UNIVERSIDADE TECNOLÓGICA FEDERAL DO PARANÁ

AUGUSTO CESAR FANTINELLI DE CARVALHO

APLICAÇÃO DE DECOMPOSIÇÃO EM ONDAS PLANAS NA MEDIÇÃO DA ABSORÇÃO *IN SITU* E ISOTROPIA

CURITIBA

2023

AUGUSTO CESAR FANTINELLI DE CARVALHO

APLICAÇÃO DE DECOMPOSIÇÃO EM ONDAS PLANAS NA MEDIÇÃO DA ABSORÇÃO *IN SITU* E ISOTROPIA

Application of plane-wave decomposition on the *in situ* absorption and isotropy measurement

Dissertation presented as requirement to the achievement of the title of Master of Engineering by the Postgraduate Program in Mechanics and Materials Engineering from the Federal University of Technology – Paraná.

Advisor: Prof. Dr. Hilbeth Parente Azikri de Deus

Co-advisor: Prof. Dr. Márcio Henrique de Avelar Gomes

CURITIBA

2023

Ministério da Educação
Universidade Tecnológica Federal do Paraná
Campus Curitiba

AUGUSTO CESAR FANTINELLI DE CARVALHO

APLICAÇÃO DE DECOMPOSIÇÃO EM ONDAS PLANAS NA MEDIÇÃO DA ABSORÇÃO IN SITU E ISOTROPIA

Trabalho de pesquisa de mestrado apresentado como requisito para obtenção do título de Mestre Em Engenharia da Universidade Tecnológica Federal do Paraná (UTFPR). Área de concentração: Mecânica Dos Sólidos.

Data de aprovação: 31 de Agosto de 2023

Dr. Hilbeth Parente Azikri De Deus, Doutorado - Universidade Tecnológica Federal do Paraná

Dr. Eric Brandao Carneiro, Doutorado - Universidade Federal de Santa Maria (Ufsm)

Dr. Marcio Henrique De Avelar Gomes, Doutorado - Universidade Tecnológica Federal do Paraná

Dr. William D Andrea Fonseca, Doutorado - Universidade Federal de Santa Maria (Ufsm)

Documento gerado pelo Sistema Acadêmico da UTFPR a partir dos dados da Ata de Defesa em 21/02/2024.

ACKNOWLEDGEMENTS

I would like, first of all, to remark that due to the format limitations, there are more people I can cite in this section who deserve their due acknowledgement for helping me and being by my side throughout this journey and my life. To all, specifically named or not, goes my eternal gratefulness.

I thank my parents, Eder and Edna, and my sister, Maria Cecília, for always being there for me, no matter what time I came home after experiments, for always listening to me ramble on about topics that they were not necessarily interested in, and for sometimes even actively helping me in equipment setup and questions related to the production of this work. Without them, I certainly would never even start the path through academia, much less finish this stage. I would also like to thank our dog, Vida. She was the best dog. May she rest peacefully.

I thank my advisors, Prof. Hilbeth Azikri, PhD, and Prof. Márcio Avelar, PhD, for guiding me through our research, presenting their opinions and counterpoints, listening to laments, complaints, and celebrations, and sometimes even sharing a beer when talking about all sorts of situations involving academia, sports, politics, and so on. I also thank them for helping me learn, write, present, discuss, and essentially set a standard for the researcher I should strive to be.

I thank Prof. Eric Brandão, PhD, for helping me navigate the theme of this research and constantly sharing his experience in the area, helping with the flow resistivity measurements, and helping me organise my thoughts regarding the object of the conducted investigations. I also thank Prof. Luiz Carlos Rodrigues, PhD, for all his support and for allowing me to use the robot from the Automation group of the Mechanical Engineering Department of UTFPR, Prof. Paulo Mareze, PhD, for helping with the flow resistivity measurements, and Prof. Rodrigo Catai, PhD, for allowing the use of the Civil Engineering Department's reverberation chamber.

To all my friends, for always having endured countless tangents about whatever I had studied, discovered, or measured that week, I thank you. I want to point out friends who directly impacted the activities described in this work: Felipe de Souza, Matheus Todt, Luis Sant'ana, and Lorenzo Garron.

I want to thank the sports clubs S. E. Palmeiras (football) and Tampa Bay Lightning (ice hockey) for providing all sorts of emotions and escapism during this time.

To you, the reader, I present my gratitude as well. I feel this work will only be finally complete when someone — you — reads this or other subsequent work and, hopefully, understands it, and it helps you know what we tried to showcase or supports you in your investigations or even enables you to find out inconsistencies that I might not have noticed when producing it.

This study was financed in part by the Coordenação de Aperfeiçoamento de Pessoal de Nível Superior – Brasil (CAPES) – Finance Code 001.

AGRADECIMENTOS

Eu gostaria, primeiramente, de salientar que, devido às limitações do formato, há mais pessoas do que eu consigo mencionar nessa seção que merecem seu devido reconhecimento por me ajudarem e por estarem ao meu lado durante essa jornada e minha vida. A todos, especificamente nomeados ou não, direciono minha eterna gratidão.

Eu agradeço aos meus pais, Eder e Edna, e a minha irmã, Maria Cecília, por sempre estarem ao meu lado, independente da hora que eu voltava pra casa após experimentos, por sempre me escutarem divagar sobre assuntos em que eles não necessariamente se interessavam, e às vezes me ajudarem ativamente na montagem de equipamento e com questões relacionadas à produção deste trabalho. Sem eles, eu certamente não teria nem ao menos começado a trajetória acadêmica, e muito menos terminaria essa etapa. Eu também gostaria de agradecer à nossa cachorra, Vida. Ela era a melhor cahorra. Que ela descanse em paz.

Eu agradeço meus orientadores, Prof. Hilbeth Azikri, PhD, and Prof. Márcio Avelar, PhD, por me guiarem durante nossa pesquisa, apresentando suas opiniões e contrapontos, ouvirem lamentações, reclamações, e comemorações, e às vezes também por dividirem uma cerveja enquanto conversávamos sobre todo tipo de situações, incluindo a academia, esportes, política, e assim por diante. Eu também agradeço por me ajudarem a aprender, escrever, apresentar, discutir, e essencialmente estabelecer um padrão para o pesquisador que devo me esforçar para ser.

Eu agradeço ao Prof. Eric Brandão, PhD, por me ajudar a navegar pelo tema dessa pesquisa e constantemente dividir sua experiência na área, me ajudar com as medições de resistividade de fluxo, e me ajudar a organizar meus pensamentos com relação ao assunto das investigaçõees conduzidas. Eu também agradeço ao Prof. Luiz Carlos Rodrigues, PhD, por todo o apoio e por autorizar a utilização do robô do Grupo de Automação do DAMEC, UTFPR, ao Prof. Paulo Mareze, PhD, por auxiliar com as medições de resistividade de fluxo, e ao Prof. Rodrigo Catai, PhD,por permitir o uso da câmara reverberante do DACOC, UTFPR.

A todos os meus amigos, por sempre terem aguentado incontáveis tangentes sobre o que quer que eu tenha estudado, descoberto, ou medido naquela semana, eu os agradeço. Eu gostaria de apontar os amigos que impactaram diretamente as atividades descritas neste trabalho: Felipe de Souza, Matheus Todt, Luis Sant'ana, e Lorenzo Garron.

Eu gostaria de agradecer aos clubes S. E. Palmeiras (futebol) e Tampa Bay Lightning (hóquei no gelo) por causarem todo tipo de emoção e escapismo durante esse tempo.

A você, leitor, eu também apresento minha gratidão. Eu sinto que esse trabalho só estará completo quando alguém — você — ler este ou outro trabalho subsequente, e assim espero, entendê-lo, e ele te ajudar a compreender o que tentamos mostrar, ou te apoiar em suas investigações, ou até mesmo te apresentar inconsistências que eu talvez não tenha notado.

O presente trabalho foi realizado com apoio da Coordenação de Aperfeiçoamento de Pessoal de Nível Superior - Brasil (CAPES) - Código de Financiamento 001.

RESUMO

A medição do coeficiente de absorção sonora é um processo importante na acústica de salas, na medida que seus resultados são utilizados por engenheiros e arquitetos em projetos, simulações, especificações etc. Nesse contexto, é vital que os valores medidos sejam coerentes com o comportamento apresentado pelo material em condições reais de aplicação. O padrão da norma ISO 354 atual que rege medições do coeficiente de absorção sonora com incidência difusa se embasa na equação de Sabine, que possui como premissa a existência de um campo acústico difuso na câmara de reverberação. A condição de difusividade de um campo sonoro é influenciada por fatores como a forma e tamanho do ambiente, e a presença de elementos difusores, e pode ser um fator difícil de se estimar exatamente. Algumas técnicas foram desenvolvidas para atingir uma medição mais confiável da absorção sonora. Este trabalho visou utilizar o processamento conhecido como decomposição em ondas planas para medir a absorção sonora de uma superfície *in situ* e quantificar a isotropia de uma câmara reverberante sob diferentes condições de absorção. Ambas as aplicações foram testadas em dois experimentos diferentes. A medição da absorção *in situ* apresentou bons resultados, comparáveis aos valores obtidos por meio da resisitividade ao fluxo medida em laboratório, com um erro que aparenta ser predominantemente sistemático. Ademais, a reconstrução do campo sonoro foi abordada para amostragens com diferentes quantidades nos arranjos. De modo geral, amostragens com mais pontos de medição apresentam reconstruções com erros menores. A difusividade da câmara reverberante foi quantificada em quatro configurações de absorção diferentes, incluindo o ambiente vazio. O indicador de difusividade apresenta valores maiores para a câmara vazia do que para os casos com absorção, mas não mostra nenhuma variação significante entre os casos com diferentes distribuições de absorvedores. Porém, o efeito da distribuição dos absorvedores é notado nas curvas de decaimento de energia e nos valores de absorção calculados pela fórmula de Sabine. Aparte disso, as reconstruções do campo sonoro foram analisadas. As reconstruções para posições dentro do volume inicial de amostragem aleatória exibiram erros menores que para os pontos fora do volume. Ademais, as diferenças entre a utilização da norma-1 ou norma-2 no cálculo da isotropia também foram observadas, com a norma-2 exibindo valores maiores devido a sua invariância rotacional.

Palavras-chave: coeficiente de absorção sonora; câmara reverberante; decomposição em ondas planas; espectro do número de onda; difusão do campo sonoro.

ABSTRACT

The measurement of the sound absorption coefficient is an important process for room acoustics, as the results they provide are used by engineers and architects for projects, simulations, specifications and such. In this context, the measured values must be coherent with the behaviour displayed by the material in real application conditions. The current ISO 354 standard that reigns over diffuse incidence absorption coefficient measurement relies on the Sabine equation, which has as a premise the existence of a diffuse sound field in the reverberation chamber. The diffuseness condition of the sound field is influenced by factors such as the enclosure's shape and size and the presence of diffusing elements and can be challenging to determine exactly. A number of techniques were developed to achieve a more trustworthy quantification of sound absorption. This work aimed to employ the process known as plane wave decomposition to measure sound absorption of an absorbing surface *in situ* and quantify the diffuseness inside a reverberation room under different absorption conditions. The *in situ* absorption measurement presented good results, comparable to values calculated from the flow resistivity measured in a laboratory, with an error that appears to be predominantly systematic. Moreover, the sound field reconstruction quality was assessed for different amounts of sampling in the array. In general, samplings with more points present reconstructions with more minor errors. The diffuseness of the reverberation chamber was quantified for four different absorption configurations, including the empty enclosure. The diffuseness indicator presents higher values for the empty chamber than for the cases with absorption but does not display any significant variation between the cases with different absorber distributions. However, the effect of the distribution of the absorber is noted in the energy decay curves and on the absorption values calculated by the Sabine formula. Aside from that, the reconstruction of the sound field was analysed. The reconstructions for positions inside the initial random sampling volume displayed smaller errors than those outside the volume. Moreover, the differences in using the 1-norm or the 2-norm in the isotropy calculation were also observed, with the 2-norm values displaying bigger values due to the rotational invariance of this norm.

Keywords: sound absorption coefficient; reverberation chamber; plane wave decomposition; wavenumber spectrum; sound field diffuseness.

LIST OF FIGURES

LIST OF SYMBOLS

Latin Letters

A, A_{T}	Equivalent absorption area	$[\mathrm{m}^2]$
A_{E}	Area of the empty chamber	$[\mathrm{m}^2]$
$A_{d,n}$	Spherical harmonics coefficient of order n and degree d	$[-]$
A_n	Spherical harmonics coefficient of order n	$[-]$
A_{WS}	Equivalent absorption area with the sample	$[\mathrm{m}^2]$
c	Speed of sound (c = 343 m/s)	$[\mathrm{m/s}]$
d	Spherical harmonics degree	$[-]$
e	Euler's number	$[-]$
f	Frequency	$[\mathrm{Hz}]$
F	Amplitude of the room transfer function	$[\mathrm{dB}]$
G	Amplitude of the exponential sweep	$[-]$
h	Impulse response	$[-]$
$\mathbf{H}$	Transfer matrix	$[-]$
$\mathbf{H}_{\mathrm{r}}$	Reconstruction matrix	$[-]$
$\mathbf{I}$	Sound intensity	$[\mathrm{W/m}^2]$
$\mathbf{I}_{\mathrm{a,r}}$	Reconstructed active sound intensity	$[\mathrm{W/m}^2]$
j	Imaginary unit (j= $\sqrt{-1}$)	$[-]$
$\mathbf{J}_{\mathrm{r}}$	Reconstructed reactive sound intensity	$[\mathrm{W/m}^2]$
$\mathbf{k}$	Wavenumber vector ($\mathbf{k} = (k_x, k_y, k_z)$)	$[1/\mathrm{m}]$
k, k_0	Wavenumber vector ($k = (2\,\pi\,f)/c = \lvert\mathbf{k}\rvert$)	$[1/\mathrm{m}]$
l	Direction index	$[-]$
L	Number of directions	$[-]$
m	Position index	$[-]$
M	Number of positions	$[-]$
n	Spherical harmonics order	$[-]$
N	Spherical harmonics maximum order	$[-]$
p	Sound pressure	$[\mathrm{Pa}]$
p_{M}	Measured sound pressure	$[\mathrm{Pa}]$
p_{r}	Reconstructed sound pressure	$[\mathrm{Pa}]$
P	Wavenumber spectrum coefficient	$[-]$
$\widetilde{P}$	Bi-dimensional wavenumber spectrum coefficient	$[-]$
$\mathbf{r}$	Position vector ($\mathbf{r} = (x, y, z)$)	$[\mathrm{m}]$
r_{c}	Critical distance	$[\mathrm{m}]$
S	Absorbing surface area	$[\mathrm{m}^2]$
t	Time	$[\mathrm{s}]$

T_{rev}	Reverberation time	$[\text{s}]$
$\mathbf{u}$	Particle velocity	$[\text{m/s}]$
$\mathbf{u}_{\text{r}}$	Reconstructed particle velocity	$[\text{m/s}]$
V	Volume	$[\text{m}^3]$
V_{p}	Reflection coefficient	$[-]$
w	Energy density	$[\text{W}\cdot\text{s/m}^3]$
W_{abs}	Absorbed energy	$[-]$
W_{inc}	Incident energy	$[-]$
W_{ref}	Reflected energy	$[-]$
$\mathbf{x}$	Wavenumber spectrum	$[-]$
$\hat{\mathbf{x}}$	Estimated wavenumber spectrum	$[-]$
Y_n^m	Spherical harmonics for order m and degree n	$[-]$

Greek Letters

α	Sound absorption coefficient	$[-]$
α_{s}	Diffuse-incidence sound absorption coefficient	$[-]$
β	Estimated decay constant	$[-]$
γ	Elevation angle of the position $\mathbf{r}$	$[\text{rad}]$
δ	Decay constant	$[-]$
$\varepsilon_{\%}$	Percentage reconstruction error	$[-]$
η	Air absorption constant	$[\text{m}^{-1}]$
θ	Elevation angle	$[\text{rad}]$
ϑ	Incidence angle	$[\text{rad}]$
$\theta_1, \ldots, \theta_5$	Robot's joint angles	$[^\circ]$
ι	Isotropy (diffuseness indicator)	$[-]$
κ	Matrix condition number	$[-]$
λ	Regularisation parameter	$[-]$
μ	Matrix coherence	$[-]$
ξ	Azimuth angle of the position $\mathbf{r}$	$[\text{rad}]$
π	Pi ($\pi = 3.14159...$)	$[-]$
ρ	Air's specific mass	$[\text{kg/m}^3]$
σ	Singular values of $\mathbf{H}$	$[-]$
τ	Time (integration constant)	$[\text{s}]$
ϕ	Azimuth angle	$[\text{rad}]$
φ	Wavenumber spectrum phase	$[-]$
$\Phi_i^{[\lambda]}$	Filter factor	$[-]$
ω	Angular velocity	$[\text{rad/s}]$
Ω	Solid angle defined by (θ, ϕ)	$[\text{rad}]$

Notations

$\overline{(\cdot)}$	Average value
$\langle\cdot\rangle_D$	Average value in the dominion D
$(\cdot)^*$	Complex conjugate
$\lvert\cdot\rvert$	Absolute value, Euclidean norm (context based)

$\|\cdot\|_1$	1-norm
$\|\cdot\|_2$	2-norm
$\hat{(\cdot)}$	Estimation
$\widetilde{(\cdot)}$	Bi-dimensional approximation
$(\cdot)^{\mathrm{T}}$	Transpose matrix
$(\cdot)^{\mathrm{H}}$	Hermitian matrix
$\nabla(\cdot)$	Gradient operator
$(\cdot)^*$	Complex conjugate
$\mathrm{Re}[\cdot]$	Real part of complex number
$\mathrm{Im}[\cdot]$	Imaginary part of complex number

Pseudo-Acronyms

ISO	International Organization for Standardization
ABNT	Brazilian Association for Technical Standards (*Associação Brasileira de Normas Técnicas*)
DIN	German Institute for Standardisation (*Deutsches Institut für Normung*)
BSI	British Standards Institution
ASTM	American Society for Testing and Materials
ANSI	American National Standards Institute
EDC	Energy Decay Curves
EDF	Energy Decay Functions
DOF	Degrees Of Freedom
RTF	Room Transfer Function

SUMMARY

1 INTRODUCTION

According to Brandão (2016), room acoustics is an area of the overall study of sound that involves the interaction of the sound inside closed environments. The behaviour of the sound inside said environment is related to the interactions between the sound and the objects' surfaces and the room's boundaries. In this context, many real-life environments, such as recording rooms, auditoriums, classrooms, video conferencing rooms, concert halls, and even audiometry cabins, may be designed, simulated, and built using techniques from room acoustics.

Determining the acoustic characteristics of materials is relevant when designing, simulating, or specifying construction materials. Concerning the reflection of the sound impinging on a surface, Brandão (2016) defines three types of phenomena: absorption, specular reflection, and diffuse reflection. Aside from these, there are other effects and related characteristics such as transmission loss (JACOBSEN; JUHL, 2013), edge diffraction effect (KUTTRUFF, 2009), and the surface impedance (VORLÄNDER, 2008). From these, an engineer can predict or simulate how the sound behaves in that enclosure and make decisions that will affect project requirements such as insulation, colouring, reverberation time, and background noise level, among others.

Thus, having well-defined processes to measure the material parameters that affect construction requirements is essential. Usually, the measurements rely on standards produced by the International Organization for Standardization (ISO). Even in local instances, standardisation organisations such as the Brazilian Association for Technical Standards (ABNT), the German Institute for Standardisation (DIN), the British Standards Institution (BSI), the American Society for Testing and Materials (ASTM), and the American National Standards Institute (ANSI) refer to ISO standards when defining their procedures and requirements. Sometimes, an ISO standard is even accepted as a local standard.

The ISO standards, namely the ISO 354 (ISO, 2003), and the ISO 3382 (ISO, 2010) eventually apply classical results and techniques from room acoustics such as Sabine's equation for random incidence absorption calculation (KUTTRUFF, 2009) and Schroeder's backwards cumulative integral to measure reverberation time (BRANDÃO, 2016). In the case of Sabine's equation, one of the hypotheses that support its derivation is the assumption that the sound field in the room is diffuse. It is worth remembering that Sabine's equation was initially derived empirically and subsequently demonstrated under the mentioned hypothesis.

A diffuse sound field can be defined in many ways and has many interesting properties (de Carvalho; GOMES; SANT'ANA, 2022). To quote Jeong (2016), a diffuse sound field is one where the sound pressure is uniform in all the points in the room (homogeneous), and the probability of energy flow is the same for all directions (isotropic). That being said, in reverberation rooms during the sound absorption measurement, because of the concentration of the absorption on a surface, it is evident that there is going to exist a difference in energy flow in the direction of the absorption. Thus the sound field will not be diffuse. Many

researchers have pointed out this inconsistency and made efforts to investigate matters such as the excessive variation of the absorption coefficient values and isotropy from laboratory to laboratory (VERCAMMEN, 2010; JEONG; NOLAN; BALINT, 2018), the assessment of isotropy in reverberation chambers (NOLAN, 2019) throughout her production, the behaviour of isotropy during sound decay (BERZBORN; VORLÄNDER, 2019), among other research.

In the context of studying a sound field in material terms, Kuttruff (2009) attests that a non-uniform distribution of absorption inside of the reverberation chamber fatally leads to a sound field that is not diffuse. That is the foreseen condition on the procedure proposed on the ISO 354 standard (ISO, 2003), which tries to circumvent this by adding diffusing elements on the boundaries of the enclosure. This implies a series of problems because not only is it currently difficult to quantify the effect these diffusers have on the sound field, but the addition of these diffusing apparatuses can also lead to more absorption to be added to the system, which can cause a contaminated or biased result, usually presenting an absorption value higher than reality. Furthermore, the absorption value can also be overestimated to values higher than one due to the edge diffraction effect (BRANDÃO, 2016).

All these uncertainties and overestimations resulting from choices made in producing the standards eventually lead to companies selecting laboratories or reverberation chamber designs that favour higher absorption values. Vercammen (VERCAMMEN, 2010; VERCAMMEN, 2009) refers to this as a "shopping" process. Moreover, the incoherence between measured values and the actual characteristics of the material may lead to poorly made design choices by architects, engineers, and designers, influenced by innermost factors they can't control or correct in any practical manner. Moreover, there can exist differences between the laboratory conditions in which the measurements are conducted and their actual employment conditions. In that sense, *in situ* techniques for measuring sound absorption can be an interesting way to circumvent diffuse field requirements.

1.1 Objectives

In the presented context, this dissertation aims to study applications of the plane-wave decomposition technique for measuring a surface's sound absorption and quantifying the sound field's isotropy.

1.1.1 Specific Objectives

A few specific objectives can be derived from the general goal of this work, in no specific order:

- Implement the plane-wave decomposition processing using inverse problem solution techniques;

- Implement the absorption calculation and the Paris formula;
- Implement the isotropy measure employing spherical harmonics decomposition;
- Validate the implemented calculations using simulation; and
- Perform tests and experiments.

Due to the diverse applications of plane-wave decomposition, the experimental aspect of this research was split into two, one focusing on absorption measurements and one focusing on isotropy measurements. This also allowed the author to use datasets previously measured by the author in previous work (de Carvalho, 2021), the matter of which was the utilisation of the robot as an array to perform sound field measurements for the ends of this work.

1.2 Methodological Approach

The sound field inside an environment may be approached in many ways. In this research, the option was to follow the techniques proposed by Nolan (2019) of calculating the plane-wave decomposition of the sound field in a particular region inside an enclosure.

For the *in situ* absorption measurement, the data measured by the author in other work (de Carvalho, 2021) was used. The setup consisted of an absorbing surface mounted on one of the walls of a laboratory room with furniture and equipment. The room was excited with an omnidirectional sound source, and a robot was used as a sequential array with random positions to measure the sound field near the absorber. From the array measurements, the wavenumber spectra for a frequency range are calculated using the plane-wave decomposition, and each of them can be used to calculate the directional sound absorption of the surface. The Paris formula (BRANDÃO, 2016) can estimate the diffuse incidence absorption from the incidence-dependent values.

For the diffuse field conditions experiment, multiple batteries of sequential array measurements in different pairs of array and sound source positions for different absorption configurations were performed inside a reverberation room. The plane-wave decomposition is calculated from these data sets and, subsequently, the isotropy of the sound field. It is also possible to extract the energy decay curves at each microphone position from the array measurements. The intention is to identify and correlate the isotropy of the sound field and the energy decay curves for the different absorption configurations.

1.3 Structure of the Text

Chapter 1 presented an introduction to the theme of this dissertation and the main objectives of this research work.

Chapter 2 presents the theoretical background and some literature review of concepts and techniques vital to understanding this work.

Chapter 3 approaches the experimental setup of the performed array measurements and justifies some of the choices made during the exploratory stage of the research.

Chapter 4 is divided into two parts, each relating to one of the experiments conducted and their respective analyses and conclusions.

Chapter 5 presents an overall recapitulation of the proposed work, some findings and some perspectives of potential further developments.

2 THEORETICAL BACKGROUND AND LITERATURE REVIEW

This chapter is dedicated to reviewing theoretical topics and literature related to the subjects of the dissertation (diffuse sound field, sound absorption, the ISO 354 standard *et cetera*) and the techniques that are employed to perform the proposed analyses (energy decay curves, plane-wave decomposition, spherical harmonics decomposition *et cetera*).

2.1 The Sound Field

Generally, a sound field is any situation where sound propagation exists. A plane wave propagating unimpeded in a medium forms a sound field, a spherical wave propagating inside an enclosure forms a sound field, and a plane wave generated by a piston, propagating inside a cylinder, creates a sound field, among an endless amount of other situations.

In any sound field, there exist two fundamental measures. The sound pressure is a scalar value usually denoted by $p(t)$, which measures the local variation of pressure depending on the time t caused by compression or rarefaction of particles of the medium (JACOBSEN; JUHL, 2013). The International System of Units (SI) unit of sound pressure is the pascal (with the symbol Pa). The particle velocity, on the other hand, measures the velocity that the particles of the medium achieve when moving back and forth, and so it is a vectorial measure that depends on the time, denoted $\mathbf{u}(t)$. Its SI unit is meters per second (m/s or $\mathrm{m\,s^{-1}}$) (JACOBSEN; JUHL, 2013). Another important measure can be derived from these two fundamental measures, which is the sound intensity, denoted by $\mathbf{I}$, that measures the flow of acoustic energy in a sound field (JACOBSEN; JUHL, 2013). It is given by the relation

$$\mathbf{I}(t) = p(t)\,\mathbf{u}(t), \tag{1}$$

and has the SI unit $\mathrm{W/m^2}$ or $\mathrm{W\,m^{-2}}$.

Real-life sound fields are usually complex, as the sound, in its propagation, can interact with surfaces, objects, or the medium itself and be reflected, absorbed, scattered, and diffracted. In these occurrences, there will be a loss of energy. Interference between sound waves, whether constructive or destructive, can also confer characteristics to the sound field. To simplify analyses, a sound field can be divided into regions surrounding the source of the sound (either an active source or a reflecting surface), following a set of criteria dependent on the distance of measurement in relation to the source. Brandão (2016) separates the sound field into three distinct regions: the near-field, the free-field, and the reverberant field. The near-field is characterised by an erratic variation of the sound pressure level in relation to the distance. What is not in the near-field is said to be in the far-field, and there is a transition region between them. The distinction between the near and far fields depends on the distance of the analysed from the source and on the frequency (BRANDÃO, 2016). The far-field can be seen as a superposition of

two distinct fields: the free-field and the reverberant-field. The proportion between free-field and reverberant-field depends not only on the distance from the source but also on the room's volume and surface area, the absorption characteristics of each surface, and the analysed frequency. The dominant behaviour on the free-field is that the sound pressure level attenuates 6 dB every time the distance from the source doubles (also called the inverse square law) (BRANDÃO, 2016), and the sound pressure level in the free field is a consequence of direct incidence from the primary source of the sound. Beyond the free field is the reverberant field, in which the sound energy is predominantly caused by the reflections of the sound on surfaces, making it so that there is little to no variation in sound pressure level when distancing from sources (BRANDÃO, 2016; KUTTRUFF, 2009; CROCKER, 2007). A valuable remark is that, aside from open spaces and anechoic chambers (in which the surfaces are highly absorbent), the far field portion of the sound field will be composed of a superposition of free field and reverberant field, and in actuality, will not follow perfectly either of the described behaviours. To discern between the free field and the reverberant field, the usual criterion is the distance beyond which the contribution of the reflections is predominant and overcomes the contribution of the direct incidence. This distance is called the critical distance (r_c) and according to Kuttruff (2009) it is calculated by

$$r_{\mathrm{c}} = \left(\frac{A}{16\,\pi}\right)^{1/2} \approx 0.1 \left(\frac{V}{\pi\, T_{\mathrm{rev}}}\right)^{1/2}, \tag{2}$$

in which A is the equivalent absorption area of the room, V is the volume of the room, and T_{rev} is the reverberation time of the room.

It is not uncommon to see the reverberant field denominated diffuse field (BRANDÃO, 2016). However, a diffuse field can also refer to the perfectly diffuse sound field (KUTTRUFF, 2009; JACOBSEN; JUHL, 2013; CROCKER, 2007), which has other requirements and is by all accounts an idealisation. Thus, in this work, the terminology for "a sound field in which the SPL's main contribution is due to the reflections" will be "reverberant field", and a "diffuse sound field" will refer to a sound field which is coherent to the idealised concept presented on Section 2.2.

2.2 The Diffuse Sound Field

The diffuse sound field is an idealised concept with many different approaches to its definition. The first consideration that must be done is that a perfectly diffuse sound field is a naturally unachievable condition because it derives from an idealised scenario. There has been an effort to rectify and concentrate the many different definitions and approaches that relate to the diffuse sound field (de Carvalho; GOMES; SANT'ANA, 2022; JEONG, 2016; JEONG; NOLAN; BALINT, 2018), with the objectives of finding whichever approach is more suitable to a particular analysis, rectifying misconceptions on the matter, and discussing the validity and application of metrics for sound field diffuseness.

Jeong (2016) states that the more accepted definition of a diffuse sound field is one where the sound pressure is uniform in relation to space — usually, this condition is referred to as homogeneity — and the probability of energy flow is uniform with regards to the direction — usually referred as isotropy.

It is essential to highlight that different authors have different ways of describing the diffuse sound field. Schultz (1971) cites uniformity in energy flow. Jacobsen (1979) proposes that, besides the isotropy condition, a diffuse sound field can be modelled by an infinite amount of plane waves that propagate with randomly related phases arriving from uniformly distributed directions. Moreover, in a more fundamental sense, Jacobsen (1979) also states that a diffuse sound field has an infinite amount of plane waves with random phase relations — in other words, the real and imaginary parts of the intensity are randomly related — arriving with the same probability with regard to the directions (JACOBSEN, 1979). This, in turn, as derived by Jacobsen, implies that the probability of energy flow is the same in all directions. The IEC 61183 standard defines the diffuse sound field as one wherein a certain position in space, and in a certain frequency or frequency band, the sound field is formed by sound arriving almost simultaneously from all directions with equal probability and level (IEC, 1994). Kuttruff (2009) defines that an isotropic sound field exists when the differential sound intensity is independent of the direction. It must be remarked that Kuttruff approaches isotropy and diffuseness as the same.

Still following Kuttruff's considerations on the matter, the author states that, in reality, a sound field can never be completely diffuse because, in that case, there would not exist net energy flow in the room (KUTTRUFF, 2009). It is not difficult to convince oneself of this since every surface — even the most perfectly reflecting surface attainable — will display losses that will cause an energy flow in their direction. This is even more true when using an enclosure to measure the sound absorption of a sample, as there will be a relatively large portion of the area with exactly the characteristic of absorbing sound energy. Moreover, specific room geometries — such as corners, domes, concavities, *et cetera* — may cause a concentration of sound energy in certain regions, infringing on the sound field's homogeneity condition.

Thus, Kuttruff states that the isotropy of the sound incidence inside a volume can not guarantee a diffuse sound field by itself and that the quantity and the distribution of the sound absorption around the enclosure are equally important.

Kuttruff (2009) analyses the sound field through the intensity as a function of the direction $I(\phi,\theta)$. The energy density is described by

$$\mathrm{d}w = \frac{I(\phi,\theta)}{c}\mathrm{d}\Omega, \tag{3}$$

where $\mathrm{d}w$ is the differential energy density, $I(\phi,\theta) = |\mathbf{I}(\phi,\theta)|$ and $\mathrm{d}\Omega$ is a infinitesimally small solid angle. Kuttruff (2009) states that since the sound field is diffuse, $I(\phi,\theta)$ does not depend

on (ϕ,θ), and thus the integration reveals

$$w = \frac{4\pi\, I}{c}. \tag{4}$$

Then, Kuttruff deduces that, since the sound waves do not lose energy with distance in the diffuse sound field, the energy density is constant through the space (KUTTRUFF, 2009).

Jacobsen and Juhl (2013) proposes that a good model for the diffuse sound field is formed by sound waves coming from all directions. This essentially means a scenario in an open medium with uncorrelated sound sources evenly distributed around a region of interest.

2.3 Energy Decay Curves

Energy Decay Curves (EDCs), also called Energy Decay Functions (EDFs), are a visual manner of observing the energy decay of a room. They stem from Schroeder's seminal research on reverberation (SCHROEDER, 1965) and are calculated using what has become known as backwards integration (KUTTRUFF, 2009)

$$\langle s^2(t)\rangle_t = \int_t^\infty [h(\tau)]^2 \mathrm{d}\tau = \int_0^\infty [h(\tau)]^2 \mathrm{d}\tau - \int_0^t [h(\tau)]^2 \mathrm{d}\tau, \tag{5}$$

where $\langle s^2(t)\rangle_t$ is the decay curve (time average of the energy of the signals), and $h(\tau)$ is an impulse response of the room relating a certain source position to a certain microphone position. The backwards integration essentially relates the ensemble average of the squared sound pressure signals at the receiver to the room's impulse response. Because the interactions between the sound and the room are ergodic, the ensemble average corresponds to the time average.

It is usual to plot the energy decay curves in logarithmic scale and for each third-octave frequency band, although other bandwidths can be used. Figure 1 displays the energy decay curves of an impulse response of a small reverberation room (115.01 m^3) damped with 10.3 m^2 of glass wool for the 500 Hz, 1000 Hz, and 2000 Hz third-octave bands.

A few things can be observed and extracted from energy decay curves. The energy decay curve can be analysed to supply an initial notion of the behaviour of the room. Randall and Ward (1960) mention that one of the characteristics of the diffuse sound field is that the decay is perfectly exponential when the field is perfectly diffuse. Furthermore, the mentioned authors state that in diffuse sound fields, the decay's characteristics are not dependent on the frequency. These are not diffuseness indicators, as they can happen in non-diffuse sound fields under certain conditions, but they can be used as starting points for practical analysis.

The reverberation time (T_{rev}) of a room can be estimated from an energy decay curve. The reverberation time is defined as the time at which the energy decays to one-millionth of the

Figure 1 – Measured energy decay curves of an impulse response for 250 Hz (red), 500 Hz (green), 1000 Hz (blue), and 2000 Hz (yellow) third-octave bands.

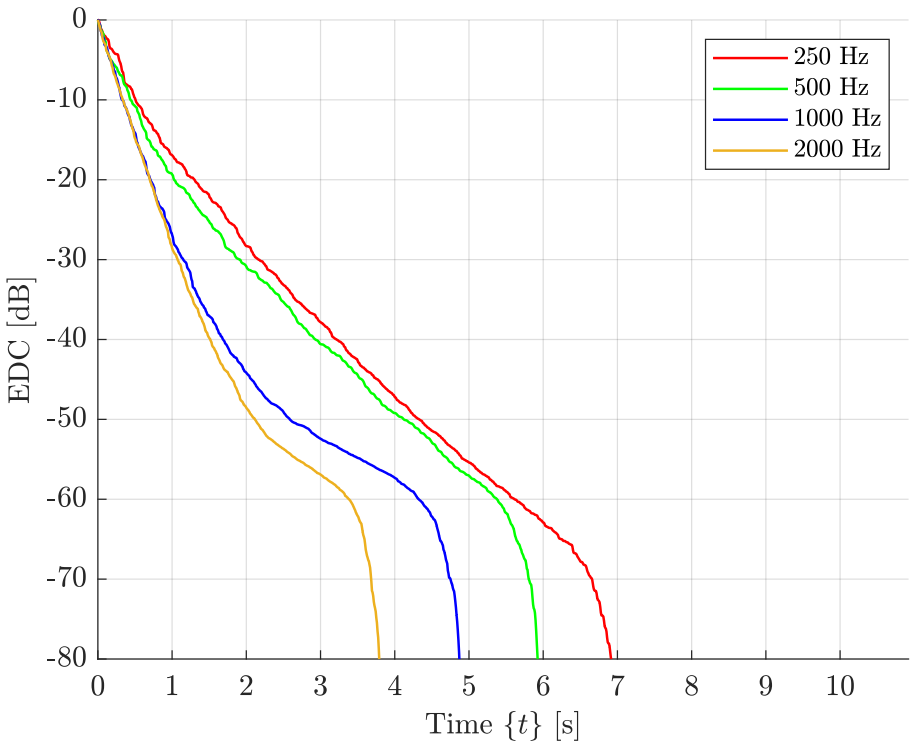

Source: own authorship (2024).

initial energy, or, regarding energy level, the energy level decays 60 dB. This can be carried out either by taking the actual time value where the curve crosses -60 dB on the graphic (T_{60}) — which usually does not present adequate results due to background noise — or by interpolating a straight line between two points of the decay and tracing it until it crosses -60 dB. Different regions of interpolation will produce different metrics:

- 0 to -10 dB: early decay time (EDT);
- -5 to -25 dB: T_{20}; and
- -5 to -35 dB: T_{30}, for example.

Balint *et al.* (2022) propose the modelling of decay functions by a multi-exponential approach. In this case, there are multiple decay times relating to different modes and their directions, with the shortest decay time pertaining to the more attenuated modes, e.g. modes more affected by an absorber. Describing a decay process with multiple (usually 2) exponential functions requires implementing a Bayesian estimation approach.

2.4 Sound Absorption

Sound absorption can be defined as a mechanism by which the sound loses energy when propagating. There exist many mechanisms that cause the sound to lose energy during propagation, such as the effects of the boundaries of the enclosure, where the sound reflects and the effect of the medium in which the sound waves propagate, which is usually air. Furthermore, when approaching the energy loss that happens on reflections, there are even more ways this can happen. In this work, the focus will be turned to the sound absorption that happens on the walls, ceiling, and floor of a room.

Brandão (2016) defines the plane-wave absorption coefficient as

$$\alpha(\vartheta) = 1 - |V_{\mathrm{p}}|^2, \tag{6}$$

in which $\alpha(\vartheta)$ is the absorption coefficient, a function of the incidence angle ϑ, and V_{p} is the reflection coefficient. It is worth clarifying that V_{p} is also dependent on the incidence angle of the sound into the surface and that the dependence in $\alpha(\vartheta)$ is a direct consequence of this fact. Thus, it is also worth stating that the absorption and the reflection coefficients depend on concrete factors such as the material's properties and how it is assembled on its utilisation site.

Furthermore, from Equation (6), one can deduce that the maximum value that $\alpha(\vartheta)$ can achieve is 1 — when $V_{\mathrm{p}} = 0$ and there is no reflection — and the minimum value is 0 — when $|V_{\mathrm{p}}| = 1$ and all the energy is reflected by the surface.

A value of absorption that depends on incidence can be interesting for specific applications. Still, in real-life scenarios, the incidence of sound on a particular surface will come from many directions.

Therefore, it is necessary to transform $\alpha(\vartheta)$ into a type of measure that is sole value, as it makes the classification of different materials and assemblies easier, but that is also still representative of the analysed phenomena. This can be carried out by applying the Paris formula (BRANDÃO, 2016)

$$\alpha_{\mathrm{s}} = \int_0^{\pi/2} \alpha(\vartheta) \sin(2\vartheta) \mathrm{d}\vartheta, \tag{7}$$

where α_{s} is called the statistical absorption coefficient (hence the sub-index "s").

Measuring the absorption of a sample α_{s} utilising its directional absorption $\alpha(\vartheta)$ can be a genuinely laborious and resource-consuming endeavour. Several works in progress propose and apply techniques and devices to perform this type of estimation (NOLAN, 2020; SOUZA, 2022; de Carvalho *et al.*, 2022), and the area of *in situ* absorption measurements has been thriving with scientific production as of late.

Other approaches to determining α_{s} can be helpful given that $\alpha(\vartheta)$ is not trivial to find. A technique based on the works of Sabine (1922) was developed to that end, and it is often used for its simplicity and the correspondence to the ISO 354 standard (ISO, 2003).

2.4.1 The Sabine Equation

Kuttruff (KUTTRUFF, 2007) presents that the decay of energy density in a room follows the relation

$$w(t) = w_0 \, \exp\left(-2 \left\langle \delta \right\rangle t\right), \text{for } t \geq 0, \tag{8}$$

in which $w(t)$ is the energy density at a time t, w_0 is the initial energy density, and $\langle \delta \rangle$ is the average decay constant of the modes. Kuttruff (2007) then states that the decay has a duration of the necessary time for the energy density to drop to one-millionth of its initial (-60 dB) — i.e. $\frac{w(t)}{w_0} = 10^{-6}$. This leads to

$$10^{-6} = \, \exp\left(-2 \left\langle \delta \right\rangle T_{\text{rev}}\right), \tag{9}$$

where T_{rev} is the reverberation time, which is the time necessary for the energy density to drop -60 dB. Applying the natural logarithm on both sides

$$-6 \, \ln 10 = \left(-2 \left\langle \delta \right\rangle T_{\text{rev}}\right), \tag{10}$$

and isolating T_{rev}

$$T_{\text{rev}} = \frac{3 \, \ln 10}{\left\langle \delta \right\rangle}, \tag{11}$$

produces a relation between the reverberation time and the average decay constant of the room.

Considering a sound source exciting the room, its energy balance is given by

$$V \frac{\mathrm{d}w}{\mathrm{d}t} = P(t) - \frac{c\,(A + 4\,\eta\,V)\,w}{4}, \tag{12}$$

in which the left-hand term is the temporal variation of energy (power) inside a constant volume V, $P(t)$ is the source power and $\frac{c\,(A+4\,\eta\,V)\,w}{4}$ is the power absorbed by the absorbing device with an equivalent absorption area A and by the air with absorption constant η (m^{-1}) (BRANDÃO, 2016). Remarkably, there is no assumption of the enclosure's geometry or the absorbing surface. The meaning of the equivalent absorption area is the weighted sum of all the surfaces of area S_{i} by their respective diffuse incidence absorption coefficients $\alpha_{\text{s, i}}$.

For a room driven by the power $P(t)$ to a steady-state scenario, when the source is "turned off" in $t = 0$, $P(t = 0) = 0$ and Equation (12) is homogeneous with solution

$$w(t) = w_0 \exp\left(-\frac{c\,(A + 4\,m\,V)\,t}{4\,V}\right) \text{ for } t > 0. \tag{13}$$

Comparing Equation (8) to Equation (13), one can conclude that

$$-2\,\langle\delta\rangle\,t = -\frac{c\,(A + 4\,m\,V)\,t}{4\,V} \text{ for } t > 0, \tag{14}$$

and thus isolate $\langle\delta\rangle$, obtaining

$$\langle\delta\rangle = \frac{c\,(A + 4\,m\,V)}{8\,V} \text{ for } t > 0. \tag{15}$$

Now, substituting Equation (15) on Equation (11) and simplifying

$$T_{\text{rev}} = \frac{24\,\ln(10)\,V}{c\,(A + 4\,m\,V)}, \tag{16}$$

or solving for A

$$A = \frac{24\,\ln(10)\,V}{c\,T_{\text{rev}}} - 4\,m\,V, \tag{17}$$

which is called the Sabine equation, as per the ISO 354 standard (ISO, 2003).

It is interesting to remark that Sabine's equation was initially derived empirically. It is a known fact that using Sabine's formula to calculate the absorption leads to systematic errors in the computed values (BRANDÃO, 2016; JACOBSEN; JUHL, 2013; KUTTRUFF, 2009; PRAWDA; SCHLECHT; VÄLIMÄKI, 2022), overestimating them sometimes presenting values over 1, which breaks the definition of the absorption coefficient. These systematic errors can be attributed to a vast set of circumstances and phenomena, such as measurement errors, insufficient diffusion of the sound field, irregularities in the shape of the sample, edge diffraction, and large values of absorption of the sample (BRANDÃO, 2016).

2.5 The ISO 354 Standard

The ISO 354 standard (ISO, 2003) is the standard that relates to measuring the sound absorption of material inside an enclosed space. Its first edition was published in 1985, with a second updated edition published in 2003. The 2003 edition was subsequently reviewed in 2008 and 2015.

The objective of this standard is to define a procedure to measure a diffuse incidence absorption coefficient, departing from the principle that the distribution of the sound waves inside an enclosure follows a uniform distribution. This, combined with the independence of the sound intensity from the spatial position, allows for a diffuse field approach to the absorption measurement, as the incidence over a sample would be random.

The standard assumes that the sound field inside a "properly designed reverberation room" (ISO, 2003) is close enough to a diffuse sound field. Therefore, the technique would be

suitable to measure an absorption coefficient for materials to be used in places such as concert halls, offices, factories, and shops, i.e. areas where the incidence of sound and (or) noise can come from many directions simultaneously. In the scope of the ISO 354 standard, not only the measurement of materials for ceiling and wall treatments is accounted for, but also of objects such as furniture, space absorbers and even people.

The standard ISO 354 (ISO, 2003) proposes that the sound absorption coefficient α_{S} is calculated through the ratio between an equivalent sound absorption area A_{T} and the actual surface area of the absorber S

$$\alpha_{\mathrm{s}} = \frac{A_{\mathrm{T}}}{S}. \tag{18}$$

The value of A_{T} is the equivalent absorption area of the chamber with the tested sample A_{WS} minus the equivalent absorption area of the empty chamber A_{E}

$$A_{\mathrm{T}} = A_{\mathrm{WS}} - A_{\mathrm{E}}\,. \tag{19}$$

In any case, the equivalent absorption area is calculated by the Sabine Equation. The reverberation time utilised should be the average of the reverberation times measured each in a different pair of a source and a transducer.

The standard has a few requirements that do not affect the measurement procedure *per se* but follow good practices for its application:

- The minimum volume V of the reverberation chamber by the ISO 354 (ISO, 2003) is 150 m^3, with a suggestion for 200 m^3;
- The maximum length of the longest straight line inside the volume of the room should be smaller than 1.9 $\mathrm{V}^{1/3}$.
- No dimensions of the room should be multiple of each other by a natural number;
- The sound field should be “sufficiently” diffuse; and
- The number of decay curves for the reverberation time averaging should be at least 12, with a minimum of microphone positions of 3 and a minimum of source positions of 2.

2.6 Plane-Wave Decomposition

Plane-wave decomposition or wavenumber approach is a technique used to represent the sound field in a region as a function of the wavenumber vector that determines a certain direction of propagation (NOLAN, 2019). The name stems from the fact that this is a transformation of the spatially sampled sound field onto a selected basis of plane-wave functions of the type

$C\,\mathrm{e}^{-\mathrm{j}\mathbf{k}\cdot\mathbf{r}}$, with $C \in \mathbb{C}$ being a complex coefficient, $\mathbf{k} \in \mathbb{R}^3$ is the wavenumber vector on the wavenumber (angular) space, and the $\mathbf{r} \in \mathbb{R}^3$ is a spatial sampling position.

This type of approach can be found throughout Nolan's work (NOLAN, 2019; NOLAN, 2020; NOLAN; FERNANDEZ-GRANDE; JEONG, 2015; NOLAN *et al.*, 2016) and articles by Brandão (BRANDÃO; FERNANDEZ-GRANDE, 2022), Fernandez-Grande (FERNANDEZ-GRANDE, 2016), Berzborn (BERZBORN *et al.*, 2019), and others (SOUZA, 2022; de Carvalho *et al.*, 2022; SOUZA; FONSECA; BRANDÃO, 2022). The technique can be used in a variety of contexts, but in this study, the focus will be on calculating the wavenumber spectrum to be used in the quantification of the isotropy of the sound field in a region (to be further explored in Section 2.7).

2.6.1 Formulation

The formulation for the plane-wave decomposition starts on the Inverse Three-dimensional Fourier Transform, which, according to Nolan (2019), is

$$p(\mathbf{r}_m) = \iiint_{-\infty}^{+\infty} P(\mathbf{k})\,\mathrm{e}^{-\mathrm{j}\,\mathbf{k}\,\cdot\,\mathbf{r}}\,\mathrm{d}\mathbf{k}, \tag{20}$$

where $p(\mathbf{r}_m) \in \mathbb{C}$ is the complex sound pressure in the mth sampling position $\mathbf{r}_m \in \mathbb{R}^3$ in space, $\mathbf{k} \in \mathbb{R}^3$ is the wavenumber vector, and $P(\mathbf{k}) \in \mathbb{C}$ is the wavenumber spectrum. The wavenumber spectrum can be, of course, written as an explicit combination of its absolute value $|P(\mathbf{k})|$ and phase $\varphi(\mathbf{k})$, that is $P(\mathbf{k}) = |P(\mathbf{k})|\,\mathrm{e}^{\mathrm{j}\,\varphi(\mathbf{k})}$.

A crucial hypothesis is needed at this point to proceed with the formulation (NOLAN, 2019). Selecting a plane-wave basis such that $|\mathbf{k}|^2 \geq k_x^2 + k_y^2$, means that no evanescent waves, i.e. waves that do not radiate to the far field are present (de Carvalho *et al.*, 2022).

Figure 2 displays a single point of a plane-wave basis, which represents a direction of propagation, in a normalised k-space — where the radiation sphere has radius 1. The absorption plane divides what are the incidence directions and what are the reflected directions when this context is applicable.

Performing the following change into spherical coordinates (de Carvalho *et al.*, 2022):

- $x_m = r\,\sin(\gamma)\,\cos(\xi)$;
- $y_m = r\,\sin(\gamma)\,\sin(\xi)$;
- $z_m = r\,\cos(\gamma)$;
- $k_x = k\,\sin(\theta)\,\cos(\phi)$;
- $k_y = k\,\sin(\theta)\,\sin(\phi)$; and

Figure 2 – Illustration of a plane-wave propagation direction in a normalised k-space.

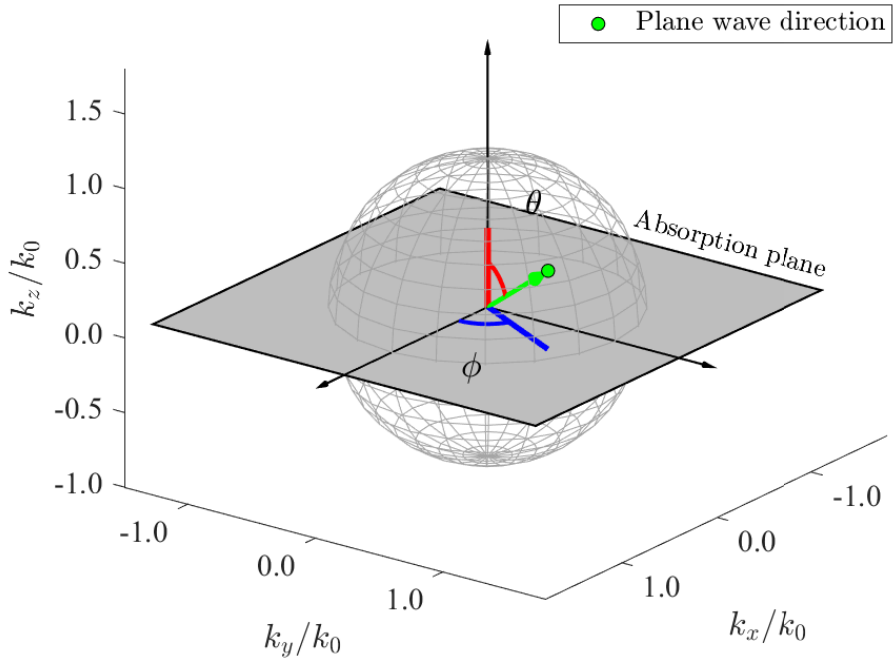

Source: own authorship (2024).

- $k_z = k\cos(\theta)$;

leads Equation (20) to Equation (21)

$$p(\mathbf{r}_m) = \int_0^{+\infty}\int_0^{2\pi}\int_0^{\pi} P(\mathbf{k})\mathrm{e}^{-\mathrm{j}\,k\,r\,(\sin(\gamma)\sin(\theta)\cos(\phi-\xi)+\cos(\theta)\cos(\gamma))}\,k^2\sin(\theta)\,\mathrm{d}k\,\mathrm{d}\theta\,\mathrm{d}\phi, \tag{21}$$

where $p(\mathbf{r}_m) = p(r,\gamma,\xi)$ in the spherical coordinates of the space and $P(\mathbf{k}) = P(k,\theta,\phi)$ in the spherical coordinates of the wavenumber space.

Another vital consideration is pertinent at this moment, which is that the sound field is being generated by a pure tone of frequency f_0. According to Nolan (2019), if that is the case, all plane waves exist in the surface of the radiation sphere of radius $k_0 = (2\pi f_0)/c$ in the k-space. This implies that the wavenumber spectrum, i.e. the representation of the sound field in the wavenumber domain, can be written by means of (NOLAN, 2019)

$$P(k,\theta,\phi) = \frac{\delta(k-k_0)}{4\pi k^2}\widetilde{P}(\theta,\phi), \tag{22}$$

where $\delta(k-k_0)/4\,\pi\,k^2$ is the Spherical Dirac Delta function for spherically symmetric curved spaces and $\widetilde{P}(\theta,\phi)$ is the two-dimensional (hence θ and ϕ) wavenumber spectrum coefficient. Substituting Equation (22) into Equation (21) and bearing in mind that $\delta(k-k_0) = 1$ only when $k = k_0$ (de Carvalho *et al.*, 2022), the sound pressure field can be written as a double integral in

θ and ϕ

$$p(\mathbf{r}_m) = \frac{1}{4\,\pi} \int_0^{2\pi} \int_0^{\pi} \widetilde{P}(\theta,\phi) \mathrm{e}^{-\mathrm{j}\,k_0\,r\,(\sin(\gamma)\,\sin(\theta)\,\cos(\phi-\xi)+\cos(\theta)\,\cos(\gamma))}\,\sin(\theta)\,\mathrm{d}\theta\,\mathrm{d}\phi. \tag{23}$$

which can be interpreted as a summation of infinitely close plane waves weighed by $\widetilde{P}(\theta,\phi)$.

In practical terms, this leads to the discrete approximation

$$p(\mathbf{r}_m) = \sum_{l=1}^{L} \widetilde{P}(\mathbf{k}_l) \mathrm{e}^{-\mathrm{j}\mathbf{k}_l \cdot \mathbf{r}_m}, \tag{24}$$

in which $p(\mathbf{r}_m)$ is the sound pressure sampled at a position $\mathbf{r}_m$, $\widetilde{P}(\mathbf{k}_l)$ is the component of the wavenumber spectrum that relates to the direction of $\mathbf{k}_l$. Instead of infinitely close plane waves, Equation (24) considers L well-defined directions of propagation. It is worth remarking that Equation (24) relates a single sound pressure sampled in $\mathbf{r}_m$ to the L sized plane-wave basis.

For a set of M measurements, M equations similar to Equation (24) can be combined into a matrix equation, as in

$$\mathbf{p} = \begin{pmatrix} \mathrm{e}^{-\mathrm{j}\mathbf{k}_1 \cdot \mathbf{r}_1} & \dots & \mathrm{e}^{-\mathrm{j}\mathbf{k}_L \cdot \mathbf{r}_1} \\ \vdots & \ddots & \vdots \\ \mathrm{e}^{-\mathrm{j}\mathbf{k}_1 \cdot \mathbf{r}_M} & \dots & \mathrm{e}^{-\mathrm{j}\mathbf{k}_L \cdot \mathbf{r}_M} \end{pmatrix} \begin{pmatrix} \tilde{P}(\mathbf{k}_1) \\ \vdots \\ \tilde{P}(\mathbf{k}_L) \end{pmatrix}, \tag{25}$$

which can be rewritten in a simpler manner

$$\mathbf{p} = \mathbf{H}\,\mathbf{x}, \tag{26}$$

in which $\mathbf{p} \in \mathbb{C}^M$ is the vector with the sound field samples in the M positions, $\mathbf{x} \in \mathbb{C}^L$ is the wavenumber spectrum, and $\mathbf{H}$ is called the transfer matrix (NOLAN, 2019). The transfer matrix contains the exponential terms that relate the $\mathbf{r}_m$ ($m = 1, ..., M$) positions and the $\mathbf{k}_l$ ($l = 1, ..., L$) plane waves.

The problem described in Equation (26) amounts to finding $\mathbf{x}$ from a known $\mathbf{H}$ and a measured $\mathbf{p}$.

2.6.2 Ill-Posed Problems and Regularisation

A critical remark about the problem at hand — Equation (25) or Equation (26) — is that $L \gg M$, with L usually being "thousands" of plane waves and M being "hundreds" of

positions, which means that this corresponds to an ill-posed problem. In other words, because $\mathbf{H}$ does not have an inverse (because it is rectangular), a unique $\mathbf{x}$ that solves Equation (26) cannot be found. Therefore, a regularisation is required to find an estimate of $\mathbf{x}$, which will be denoted $\hat{\mathbf{x}}$.

The first instinct to solve Equation (26) for $\mathbf{x}$ would be to use a least squares solution formulated as

$$\hat{\mathbf{x}} = \min_{\mathbf{x}} \|\mathbf{H}\,\mathbf{x} - \mathbf{p}\|_2^2, \tag{27}$$

where $\|\cdot\|_2^2$ denotes the square of the Euclidean norm. This formulation will present a solution for which the residual is minimal. However, this can also present a solution that is not stable, non-regular, or both. This is problematic due to the physical interpretation of the solution $\hat{\mathbf{x}}$. Reverberant sound fields imply that the sound impinges from several directions in a region, which can be translated to a smoothness or regularity requirement of the wavenumber spectrum.

To incorporate the regularity requisite in the least squares problem, the Tikhonov regularisation technique can be used (HANSEN, 2010; CESARO; LEITÃO, 2010). This is a well-known solution for inverse problems and has been associated with the plane-wave decomposition technique throughout its implementations (NOLAN, 2019; de Carvalho *et al.*, 2022; BRANDÃO; FERNANDEZ-GRANDE, 2022; FERNANDEZ-GRANDE, 2016; de Carvalho *et al.*, 2022). The Tikhonov solution for a least squares problem is defined as

$$\hat{\mathbf{x}} = \min_{\mathbf{x}} \|\mathbf{H}\,\mathbf{x} - \mathbf{p}\|_2^2 + \lambda^2 \|\mathbf{x}\|_2^2\,, \tag{28}$$

in which λ is called the regularisation parameter. The core of the Tikhonov regularisation is that λ is chosen following a criterion in such a way that it ponders between the norm of the residual $\|\mathbf{H}\,\mathbf{x} - \mathbf{p}\|_2$ (i.e., how well the solution fits the problem) and the norm of the solution $\|x\|_2$ (i.e., how regular the solution itself is), leading to a solution that fits satisfactorily Equation (26) and is regular enough to be representative of the measured sound field. It is interesting to remark that different criteria also exist, such as the compressive sensing technique, which uses the $\|\cdot\|_1$ norm, associated with the sparsity of the solution.

Equation (28) has a closed form solution for $\hat{\mathbf{x}}$ (de Carvalho *et al.*, 2022; HANSEN, 2010)

$$\hat{\mathbf{x}} = \left(\mathbf{H}^{\mathrm{H}}\,\mathbf{H} + \lambda^2\,\mathbb{I}\right)^{-1}\mathbf{H}^{\mathrm{H}}\,\mathbf{p}\,, \tag{29}$$

which can be further simplified by applying the singular value decomposition (SVD) of $\mathbf{H}$ (de Carvalho *et al.*, 2022; HANSEN, 2010)

$$\hat{\mathbf{x}} = \mathbf{V}\left(\mathbf{\Sigma}^{\mathrm{H}}\,\mathbf{\Sigma} + \lambda^2\,\mathbb{I}\right)^{-1}\mathbf{\Sigma}^{*}\,\mathbf{U}^{\mathrm{H}}\,\mathbf{p}\,, \tag{30}$$

in which $\mathbf{H} = \mathbf{U}\,\mathbf{\Sigma}\,\mathbf{V}^{\mathrm{H}}$ is the SVD of $\mathbf{H}$, $\mathbf{U}$ and $\mathbf{V}$ being unitary (i.e. $\mathbf{U}^{-1} = \mathbf{U}^{\mathrm{T}}$) and $\mathbf{\Sigma}$ being a diagonal matrix containing the singular values $\{\sigma_1,...,\sigma_M\}$ of $\mathbf{H}$ in its principal diagonal.

Having in mind the nature of the matrices $\mathbf{U}$, $\mathbf{V}$ and $\mathbf{\Sigma}$, and through some algebraic manipulation, Equation (30) can be written as a summation of vectors (de Carvalho *et al.*, 2022; HANSEN, 2010) such as

$$\hat{\mathbf{x}} = \sum_{i=1}^{n} \Phi_i^{[\lambda]} \frac{\mathbf{u}_i^{\mathrm{H}} \mathbf{p}}{\sigma_i} \mathbf{v}_i \,, \tag{31}$$

where $\Phi_i^{[\lambda]}$ is the filter factor or filter function (HANSEN, 2010; CESARO; LEITÃO, 2010)

$$\Phi_i^{[\lambda]} = \frac{|\sigma_i|^2}{|\sigma_i|^2 + \lambda^2} \,. \tag{32}$$

The filter factor is important because it behaves in such a manner that reduces the influence of the errors caused by the smaller singular values (when $\lambda \gg \sigma_i$) (de Carvalho *et al.*, 2022; HANSEN, 2010).

The regularisation parameter λ can be selected following many different criteria. A classical procedure to determine λ is the L-curve method (de Carvalho *et al.*, 2022; HANSEN, 2010), which amounts to find the λ that produces the maximum curvature on the curve that relates $\|\hat{\mathbf{x}}\|_2$ and $\|\mathbf{H}\,\hat{\mathbf{x}} - \mathbf{p}\|_2$. The technique is called L-curve because the relation between $\|\hat{\mathbf{x}}\|_2$ and $\|\mathbf{H}\,\hat{\mathbf{x}} - \mathbf{p}\|_2$ in the logarithmic scale resembles an "L" shape, with the maximum curvature being the transition between the vertical portion of the "L" and the horizontal part of the "L".

2.6.3 Sound Field Reconstruction

The sound field can be reconstructed in arbitrary positions using the wavenumber spectrum measured from an array (NOLAN, 2019; de Carvalho *et al.*, 2022; FERNANDEZ-GRANDE, 2016; NOLAN *et al.*, 2019). This can be employed to assess the acoustic impedance of a surface, for instance, by reconstructing the sound pressure and the particle velocity (NOLAN, 2019; FERNANDEZ-GRANDE, 2016; NOLAN *et al.*, 2019). The sound intensity can also be calculated from the reconstruction of the sound field (NOLAN, 2019; FERNANDEZ-GRANDE, 2016; NOLAN *et al.*, 2019).

The reconstruction process is the solution to the direct problem for an estimated $\hat{\mathbf{x}}$. For sound pressure, the reconstruction is given by Equation (33)

$$\mathbf{p}_{\mathrm{r}} = \mathbf{H}_{\mathrm{r}} \hat{\mathbf{x}}, \tag{33}$$

in which $\mathbf{p}_{\mathrm{r}}$ is the size K vector containing the reconstructed sound pressures in K arbitrary positions in the vicinity of the array, and $\mathbf{H}_{\mathrm{r}}$ is the $K \times L$ reconstruction matrix, calculated from the plane wave functions evaluated on the points where the sound field will be reconstructed.

Figure 3 – Wavenumber spectrum for a sound field created following Jacobsen's model at 500 Hz.

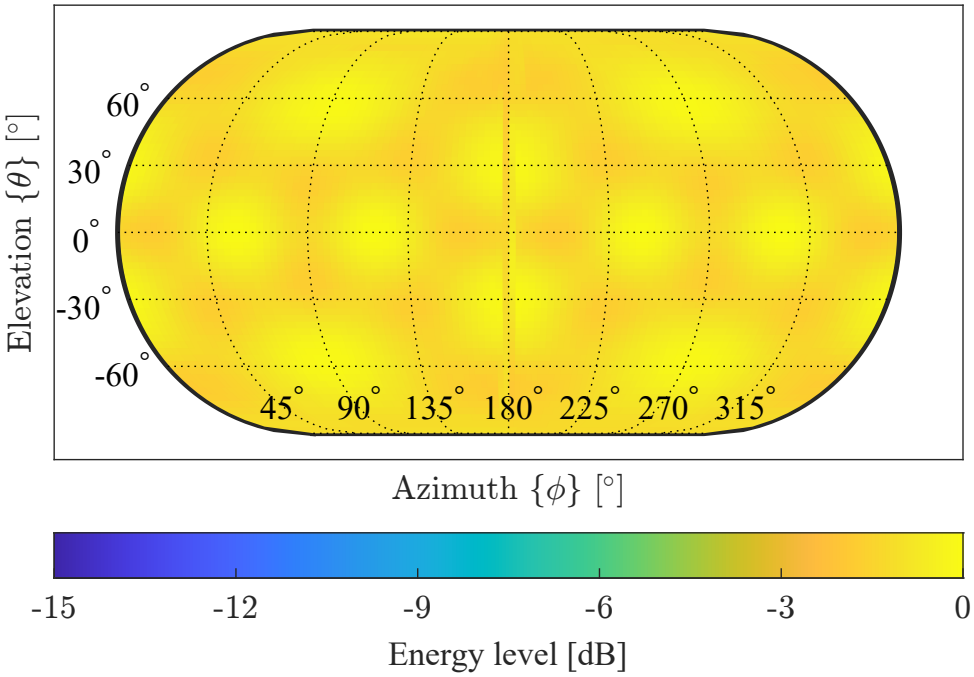

Source: own authorship (2024).

Once $\mathbf{p}_r$ is calculated, one can calculate the particle velocity $\mathbf{u}_r$ through Equation 34, and the active and reactive intensities $\mathbf{I}_{a,r}$ and $\mathbf{J}_r$ using Equations 35 and 36

$$\mathbf{u}_r = -\frac{1}{j\,\omega\,\rho}\nabla\mathbf{H}_r\hat{\mathbf{x}}, \tag{34}$$

$$\mathbf{I}_{a,r} = \frac{1}{2}\,\mathrm{Re}\left[\mathbf{p}_r\mathbf{u}_r^*\right], \tag{35}$$

$$\mathbf{J}_r = \frac{1}{2}\,\mathrm{Im}\left[\mathbf{p}_r\mathbf{u}_r^*\right], \tag{36}$$

in which $\nabla\mathbf{H}_r$ is the gradient of the reconstruction matrix, ω is the angular velocity, and ρ is the air's specific mass.

2.6.4 Wavenumber Spectrum of a Diffuse Sound Field

For Jacobsen's diffuse sound field model described in Section 2.2, the wavenumber spectrum is shown in Figure 3. A total of 10242 sound sources, placed over a sphere with 50 m of radius following an icosahedron-based distribution, were used to simulate the sound field, which was sampled in random positions, using the same array from Figure 20. The frequency generated by these sources was set at 500 Hz.

It can be observed that the diffuse sound field presents almost the same sound power level in every direction.

2.6.5 Calculation of the Sound Absorption from the Wavenumber Spectrum

When calculated in relation to an absorbing surface, the angular spectrum contains information about the incident and reflected sound energies on the absorber. Thus, the incidence-dependent absorption coefficient $\alpha(\vartheta)$ can be computed by means of

$$\alpha(\vartheta) = \frac{W_{\text{abs}}(\vartheta)}{W_{\text{inc}}(\vartheta)} = 1 - \frac{W_{\text{ref}}(\vartheta)}{W_{\text{inc}}(\vartheta)}\,, \tag{37}$$

in which $W_{\text{abs}}(\vartheta)$ is the absorbed energy, $W_{\text{ref}}(\vartheta)$ is the reflected energy, and $W_{\text{inc}}(\vartheta)$ is the energy that impinges on the absorber. In any case, the third-octave angular spectra must be averaged in the azimuth ϕ. This mitigates potential biases caused by directions with no incidence (NOLAN, 2020). This averaging process essentially corresponds to the numerical integration of the energy — or $|\hat{\mathbf{x}}|^2$ — on the azimuth interval $[0, 2\pi]$. The quantities $W_{\text{ref}}(\vartheta)$ and $W_{\text{inc}}(\vartheta)$ can be calculated using

$$\begin{aligned} W_{\text{ref}}(\vartheta) &= \frac{1}{2\pi}\int_0^{2\pi} |\widetilde{P}(\theta,\phi)|^2 \,\mathrm{d}\phi, \\ W_{\text{inc}}(\vartheta) &= \frac{1}{2\pi}\int_0^{2\pi} |\widetilde{P}(\pi-\theta,\phi)|^2 \,\mathrm{d}\phi. \end{aligned} \tag{38}$$

To determine a diffuse field absorption coefficient, one can use the Paris' formula (BRANDÃO, 2016)

$$\alpha_{\text{s}} = \int_0^{\pi/2} \alpha(\vartheta)\,\text{sen}(2\vartheta)\,\mathrm{d}\vartheta. \tag{39}$$

It should be noted that the Paris' formula considers that the incidence on the absorber is the same in every direction, which is unlikely to happen for *in situ* conditions. However, using a near-omnidirectional sound source — as omnidirectionality is another idealised concept, the room can be excited in such a way that the many reflections in the *in situ* environment impinge on the absorber, and, through averaging, the lack of isotropic incidence is mitigated.

2.7 Isotropy Indicator

Nolan (2019) proposes a metric to quantify the diffuseness of a sound field based on its isotropy. An isotropic sound field is, by definition, spherically symmetric. In practical terms, the magnitude of the waves is constant with the directions.

For Nolan's indicator, the first step is a spherical harmonics decomposition of the wavenumber spectrum. The absolute value of the wavenumber spectrum representation of the

Figure 4 – Spherical harmonics for orders 0 (first row), 1 (second row) and 2 (third row).

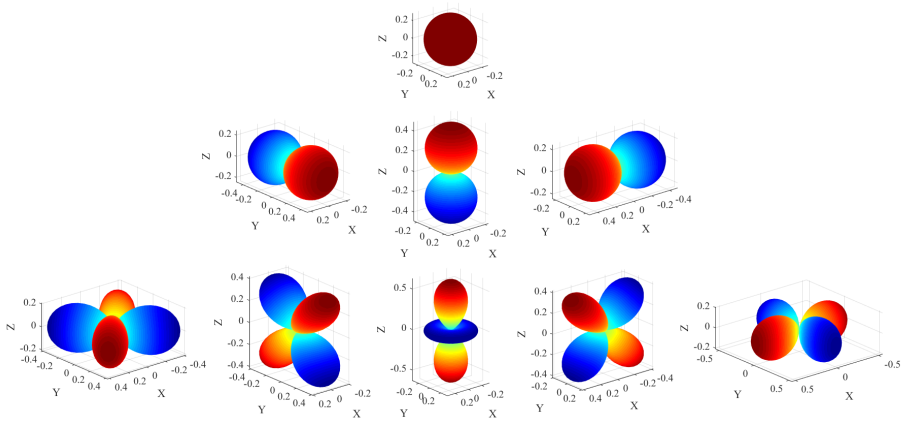

Source: own authorship (2024).

sound field relates to the spherical harmonics by means of

$$|\widetilde{P}(\theta,\phi)| = \sum_{n=0}^{\infty} \sum_{d=-n}^{n} A_{d,n}(k_0)\, Y_n^d(\theta,\phi), \tag{40}$$

in which $A_{d,n}(k_0)$ are the spherical Fourier coefficients and $Y_n^d(\theta,\phi)$ are the spherical harmonics. The spherical harmonics up to an order $N = 2$ are depicted in Figure 4. Further orders are omitted for the sake of briefness. The process for calculating the $A_{d,n}(k_0)$ coefficients is based on work by Fahim (2019).

The dependence of k_0 reinforces that a distinct set of coefficients will exist for each frequency. The inverse transform that supplies $A_{d,n}(k_0)$ is

$$A_{d,n}(k_0) = \int_0^{2\pi} \int_0^{\pi} |\widetilde{P}(\theta,\phi)|\, [Y_n^d(\theta,\phi)]^*\, \sin(\theta)\, \mathrm{d}\theta\, \mathrm{d}\phi, \tag{41}$$

which can be computationally expensive and prone to errors due to discretization. To find the spherical harmonics coefficients, a better alternative is to reinterpret Equation (40) as a matrix equation and solve it for the coefficients $A_{m,n}(k_0)$.

There are two different ways to define the diffuseness indicator relating to the type of norm utilised. The diffuseness indicator using the 1-norm is defined as (NOLAN, 2019)

$$\iota_1(k_0) = \frac{|A_{0,0}(k_0)|}{\sum_{n=0}^{\infty} \sum_{d=-n}^{n} |A_{d,n}(k_0)|}, \tag{42}$$

where ι is the isotropy or diffuseness (highlighting that isotropy is the governing condition for diffuseness), and $|A_{0,0}(k_0)|$ is the magnitude of the monopole spherical harmonic. Notice that

the summation in the degrees of the spherical harmonics is done using a simple summation, which is what is referred to as 1-norm (TANAKA; OTANI, 2023). The other way of calculating the isotropy of the sound field is to use the 2-norm of the spherical harmonics. This is carried out by means of

$$\iota_2(k_0) = \frac{\sqrt{|A_{0,0}(k_0)|^2}}{\sum_{n=0}^{\infty} \sqrt{\sum_{d=-n}^{n} |A_{d,n}(k_0)|^2}}, \tag{43}$$

in which the summation in the spherical harmonics degrees is done by means of the square root of the sum of the squares (TANAKA; OTANI, 2023). The main difference between the two techniques, according to Tanaka and Otani (2023), is the utilisation of the 2-norm circumvents a bias present in the 1-norm technique, which overestimates the contribution of plane waves near the polar directions. This is observed by verifying the isotropy values for single plane-wave wavenumber spectra with different directions of arrival. It was noticed that when using the 1-norm isotropy, the isotropy values vary depending on the direction of propagation because the components near the poles are overestimated i.e. they present a smaller isotropy than directions close to the equator. The range of this variation depends on the truncation order. For the 2-norm, the isotropy values do not vary with the direction of arrival. This happens due to the rotational variance of the 1-norm and the rotational invariance of the 2-norm (TANAKA; OTANI, 2023). This also makes it so that errors related to the truncation of N are also rotationally invariant for the 2-norm.

The 1-norm of the spherical harmonics of order n can be explicitly written as

$$\|A_n\|_1 = \sum_{d=-n}^{n} |A_{d,n}|, \tag{44}$$

omitting the dependence in k_0, and the 2-norm of the spherical harmonics of order n can be explicitly written as

$$\|A_n\|_2 = \sqrt{\sum_{d=-n}^{n} |A_{d,n}|^2}, \tag{45}$$

again omitting the dependence in k_0. Because this type of analysis is very recent, both manners of calculating sound field isotropy will be analysed.

In any case, what happens is a comparison between the contribution of the monopole moment in relation to all the contributions of the other components. If only the monopole ($n = 0$, $d = 0$) has a significant value, the function has a shape close to a sphere, which means the wavenumber spectrum is symmetric in the directions, thus $\iota = 1$. Conversely, if there are contributions from other moments, the sum in the denominator presents a larger value, and ι approaches 0.

For the model described in Section 2.2 with the wavenumber spectrum displayed in Figure 3, the spherical harmonics order distribution is shown in Figure 5.

Figure 5 – Spherical harmonics order distribution and isotropy values for a diffuse sound field at 500 Hz, with maximum order 7. Left: Using the 1-norm. Right: Using the 2-norm.

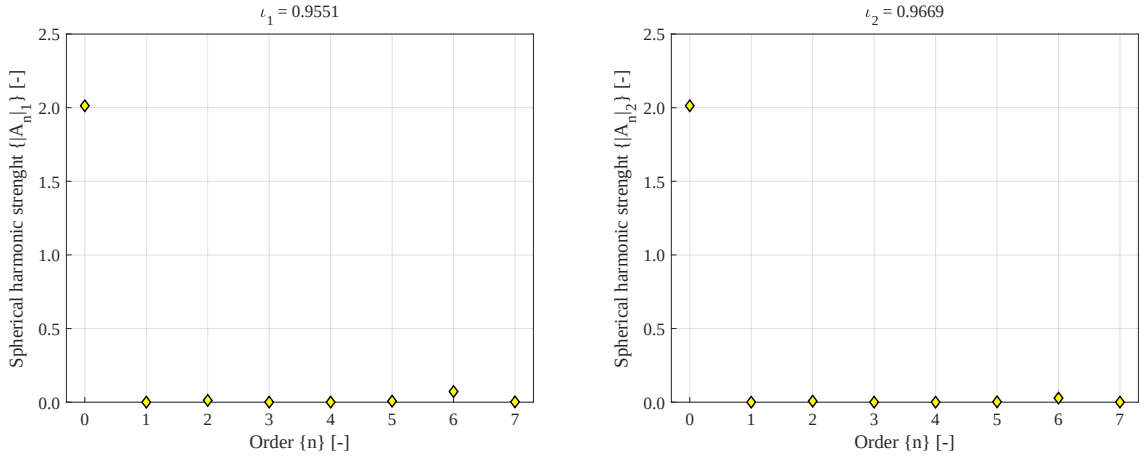

(a) 1-norm. **(b) 2-norm.**

Source: own authorship (2024).

It is evident that the main contribution is the monopole. The spherical harmonics decomposition was done up to order $N = 7$. The isotropy values calculated for this scenario correspond to $\iota_1 = 0.9551$ and $\iota_2 = 0.9669$ and are close to the expected unity. The difference between the values is attributed to the overestimation of the denominator in Equation (42). Evidence of this is that the value of the 1-norm of the spherical harmonics of order 6 is bigger than its 2-norm. The values end up being smaller than one because the simulated diffuse sound field, using the model proposed by Jacobsen (1979), still depends on hardware limitations, as a computer can only calculate a finite amount of plane waves.

For increasing maximum order values, some strength is attributed to the higher orders, which can decrease the isotropy value. This can be seen as a truncation error in isotropy. Figure 6 shows the spherical harmonics order distribution for a maximum order of 10 using the 1-norm and 2-norm.

The difference between the 1-norm and 2-norm isotropy is larger when using the maximum order $N = 10$ instead of $N = 7$, which is also evidence of cumulative overestimation in the denominator. Moreover, the difference when comparing the ι_2 values and the ι_1 values can be attributed to energy being attributed to the higher order coefficients, which also elevates the denominator of the ratios. Therefore, it is important to point out that although the utilisation of random sound field sampling allows for higher orders of truncation than when using a spherical array, the choice of the maximum order must consider the truncation error and the processing time, as larger truncation orders will take longer to process while producing inaccurate results.

Figure 6 – Spherical harmonics order distribution and isotropy values for a diffuse sound field at 500 Hz, with maximum order 10. Left: Using the 1-norm. Right: Using the 2-norm.

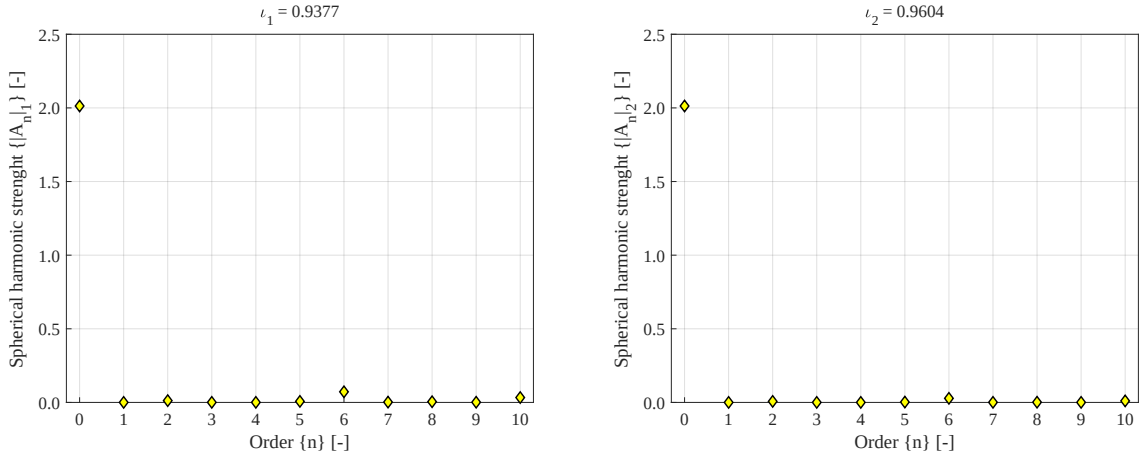

(a) 1-norm. **(b) 2-norm.**

Source: own authorship (2024).

3 EXPERIMENTAL SETUP AND PROCEDURE

This chapter is dedicated to describing the operational aspects common to the experiments conducted for this research. Specific characteristics of each experiment will be discussed in their respective sections.

3.1 Array

The arrays used in the experiments consisted of sequential arrays formed using a robotic arm coupled with a microphone to achieve sets of previously chosen positions. The used robot was a Mitsubishi RV-M1 robot arm with five degrees of freedom (DOF). This robot was selected due to its availability for utilisation and was loaned from the Flexible Manufacturing Systems Laboratory from UTFPR - Curitiba Campus. A schematic of the robot indicating each joint and its joint limits can be seen in Figure 7.

Figure 7 – Mitsubishi RV-M1 joints.

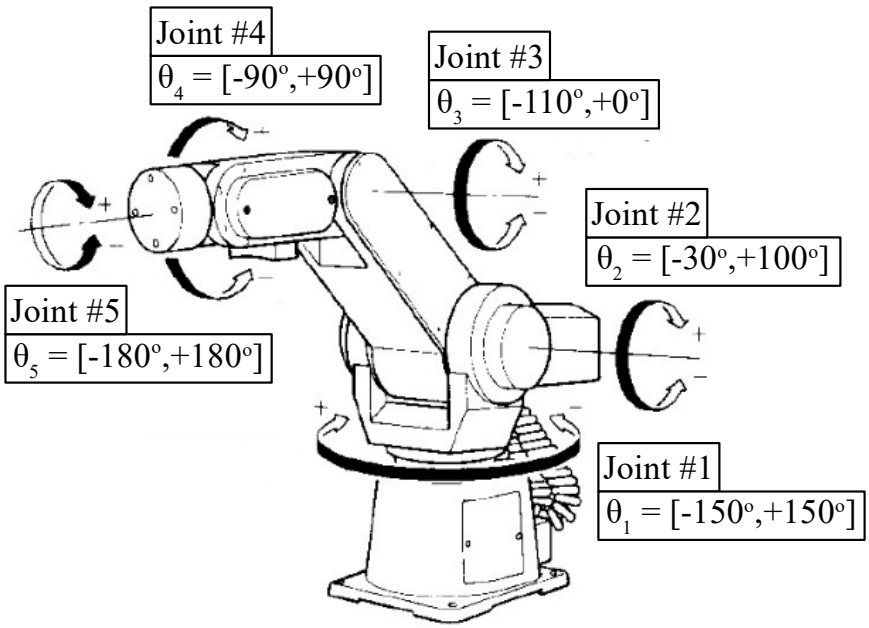

Source: Adapted from Mitsubishi Electric Corporation (1989).

The microphone was attached to the robot by means of a microphone holder, depicted in Figure 8, designed to keep the microphone tilted at a 45^o angle in relation to the centre of joint #5. This was done to prevent a circular symmetry of the transducer in relation to joint #5, which would annul the respective DOF.

The control of the robot was carried out via MATLAB, integrating the robot arm with the ITA Toolbox (BERZBORN *et al.*, 2017), which controlled the impulse response measurement.

Figure 8 – Close-up view of the microphone holder.

Source: Adapted from de Carvalho (2021).

The communication between the robot and the computer was done using the RS232 serial communication standard, which is native to this robot.

In any case, robots have limitations on the positions they can access, so the possibility of accessing each position needs to be verified. This was done by calculating the inverse kinematics of each position when generating the array, where if a position was considered inaccessible, it would be discarded, and a new one would be promptly generated and verified. In both experiments done in this research, the arrays consisted of random positions inside predefined rectangular volumes, with the microphone pointed parallel to the robot's y axis (forward). It is important to point out that the inverse kinematics of any robot consists of a set of equations that will relate the position and arrival direction of the robot to the angles each joint must achieve — sometimes referred to as the robot's "pose" — and these equations depend on design characteristics of each robot model. Although the inverse kinematics are hard-coded in industrial robots, they usually need to be manually derived for external applications, especially if the robot is a discontinued model such as the Mitsubishi RV-M1. Fortunately, because this robot is currently used for didactic purposes at UTFPR, its inverse kinematics had already been derived by Prof. Luís Paulo Laus, and they only needed to be transcribed to MATLAB.

3.2 Impulse Response Measurement

The impulse responses were measured by means of the exponential sweep technique (de Carvalho, 2021; MÜLLER; MASSARANI, 2001), as it is implemented in the ITA-Toolbox (BERZBORN *et al.*, 2017). The sound source used to excite the room was a GROM DDC-110

omnidirectional sound source shaped like a dodecahedron. The microphone used to record the sweep was a GRAS 46AQ of random incidence (suited for diffuse sound fields), together with a GRAS 26CA pre-amplifier. Other equipment used was a Roland Quad-Capture audio interface, an Alesis RA-100 reference amplifier, and a GRAS 12AL power module and signal conditioner for the microphone. A diagram representing the connection between these components (black lines) and the flow of signal in the measurement system (represented by the arrowheads in the lines) is present in Figure 9.

Figure 9 – Diagram displaying the connection between components (black lines) and the flow of signal (black arrowheads) in the measurement chain.

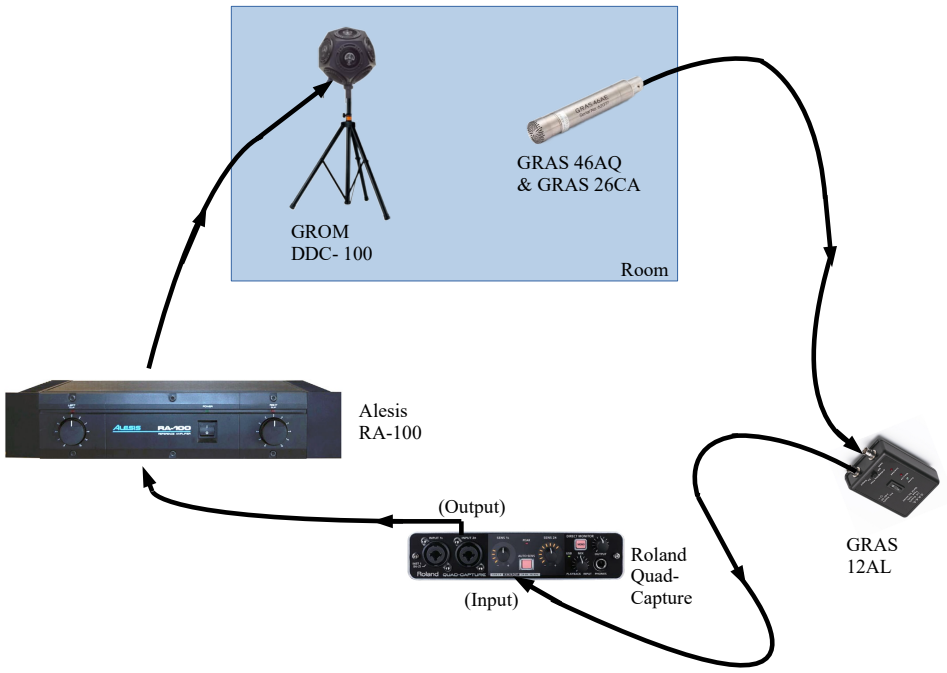

Source: own authorship (2024).

It is important to remark that the Roland Quad-Capture connects directly to the computer. The interface between the ITA Toolbox on MATLAB and the Roland Quad Capture card is done by means of the ASIO4ALL driver (Steinberg Media Technologies GmbH, 2023).

As for the measurement techniques, an exponential sweep was chosen, as it presents the same energy in all frequency bands (MÜLLER; MASSARANI, 2001), with a linear deconvolution to separate the actual impulse responses from speaker distortions and other distortion-associated phenomena. Figure 10 displays an exponential sweep generated using the ITA Toolbox, with a zoom in between 0 and 0.1 s to highlight the sinusoidal behaviour of the sweep. Coincidentally, this is the sweep used in Experiment # 2 (Section 4.2).

Figure 10 – Exponential sweep with 10.92 s of length, and stop margin of 2 s, between 20 Hz and 5000 Hz.

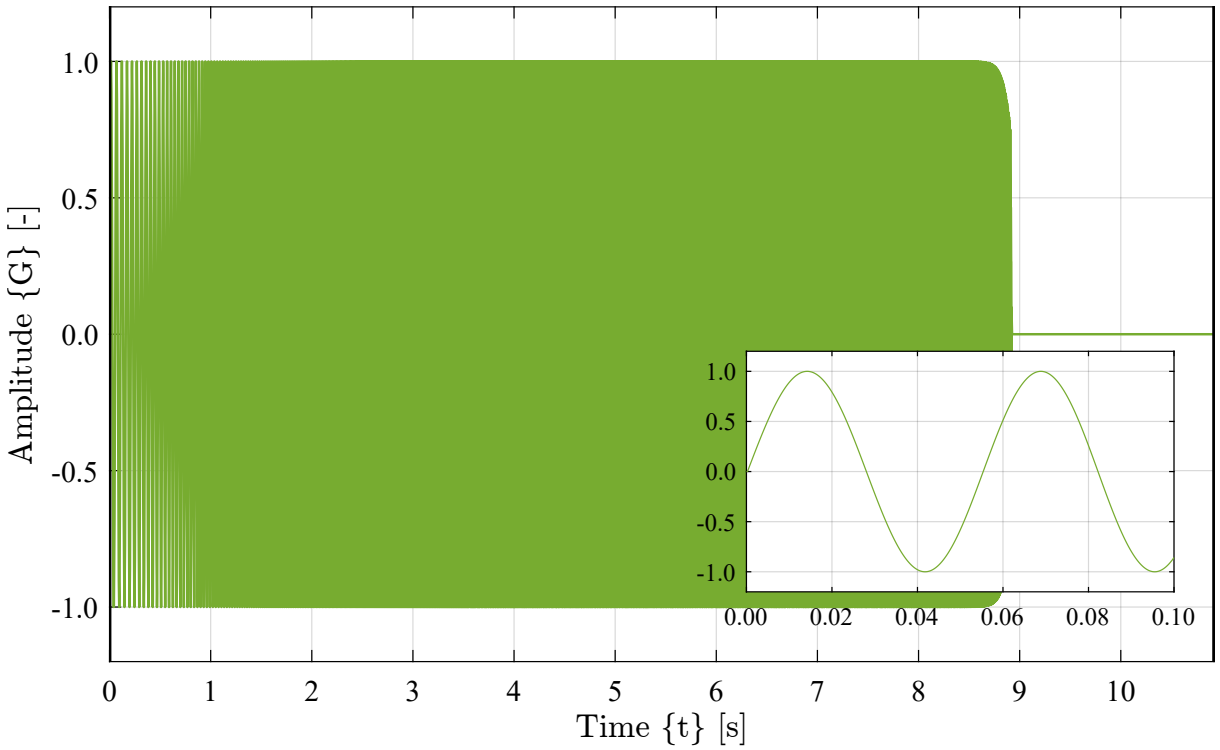

Source: own authorship (2024).

3.3 Plane Wave Decomposition

The plane wave decomposition, as explained in the Subsection 2.6.2, involves solving the ill-posed problem given by Equation (26) for $\mathbf{x}$, by means of regularisation. Because they were measured using linear deconvolution, the impulse responses needed to have their second half cropped out. The latency of the sound interface was also compensated using the calibration process present in the ITA Toolbox (BERZBORN *et al.*, 2017). The ITA Toolbox automatically presents the correspondent transfer functions from the cropped impulse responses. An easy way to automatise the process is to arrange the transfer functions in a matrix, in which the lines are the microphone positions and the columns are the values for each frequency step. In this arrangement, each column corresponds to a $\mathbf{p}$ related to a particular discrete frequency value in Equation (26), and each regularisation will result in a correspondent $\mathbf{x}$.

With relation to the array, because the microphone positions were generated in relation to the robot's reference position $(0,0,0)$, they all needed to be transformed to a reference position that has some relation to the type of phenomenon that is being analysed: the surface in the case of the absorption measurement; or the array centre in the isotropy measurement. This was done by means of a homogeneous transformation, which is a type of computation that writes the

points in the new coordinate system by means of simultaneous linear translation and rotation. Homogeneous transformations are commonly used in robotics, and more information about them can be found in related literature (CROCKER, 2005).

The plane wave basis is generated following the solution of the Thomson problem, as it provides a homogeneous distribution of points over a sphere. This is carried out through an optimised algorithm by Semechko (2021), available for MATLAB. Because the experiments approached in this dissertation do not involve evanescent waves, only points in the sphere's surface are considered. Moreover, the plane wave basis is comprised of 1000 directions, as recommended by Nolan and Xiang (2023).

The wavenumber spectrum for a broad range of frequencies is calculated through a loop that goes through the discrete frequencies and estimates a regularised solution at each step. From the array, the plane wave basis, and the frequency information, the matrix H can be calculated, in this case, for each frequency. This regularisation process for a range of frequencies is quite time-consuming due to the calculation of the SVD decomposition of H at each iteration of the loop. The SVD decomposition can be calculated using the compact form (faster) or the full form (slower). For applications such as the isotropy calculation or absorption measurement, no problems were noticed when using the compact SVD. However, the utilisation of the compact SVD can lead to an "upside-down" — or mirrored — wavenumber spectrum in some cases, which is problematic when calculating the reconstructions. This is not problematic when calculating the absorption and isotropy because the "upside-down" spectrum preserves the energy in the hemispheres (in the absorption case) and preserves the spherical harmonics decomposition (in the isotropy case).

The regularisation technique used was the Tikhonov regularisation because it provides solutions that are smooth, which is desirable when using plane wave decomposition in reverberant environments (NOLAN, 2019). Furthermore, it is a well-known technique, and it is available for MATLAB. The functions used for the regularisation are available in Hansen's "Regularization Tools" toolbox (HANSEN, 2007). The regularisation parameter was calculated using the l-curve technique, also for its availability and for being the method classically used for the approach proposed by Nolan (2019).

It is usual to calculate the average wavenumber spectrum for each third-octave frequency band. This is done to eliminate any bias caused by non-isotropic sound fields, which can exist when considering sound fields created by pure tones (NOLAN, 2020).

3.4 Reconstruction

The reconstruction of the transfer function in a position corresponds to the solution of the direct problem of Equation (26) using the estimated wavenumber spectrum. In a similar manner to the regularisation, a loop that goes through the frequencies is used and a reconstruction matrix H_r is computed from the informed plane wave basis, frequency, and reconstruction positions.

The reconstruction error $\varepsilon_{\%}$ is calculated by means of

$$\varepsilon_{\%} = 100 \times \left| \frac{p_{\mathrm{r}}(f) - p_{\mathrm{M}}(f)}{p_{\mathrm{M}}(f)} \right|; \tag{46}$$

where $p_{\mathrm{r}}(f)$ is the reconstructed pressure in a certain frequency f, $p_{\mathrm{M}}(f)$ is the pressure measured in the reconstruction point for that same frequency f. This error is a percentage error proposed by Fernandez-Grande (2016), which can then be averaged in third-octave bands.

3.5 Absorption

From the third-octave average wavenumber spectra, one of the things that can be calculated is the absorption of a surface by the ratio of incident and reflected energy. For this, the wavenumber spectra averaged need to be calculated with the reference in the measured surface i.e. the centre of the radiation sphere needs to be positioned on the surface that is being measured. This will confer a context for what is the incidence region and what is reflection, which is the absorption plane, depicted in Figure 2. Another point that should be remarked is that the direction of the propagation directions, given by the points in the radiation sphere, can appear as an "outward" vector or an "inward" vector, depending on how the plane wave basis is informed. In other words, a point (k_x,k_y,k_z) can represent a direction that points from the centre to the point — $(k_x,k_y,k_z) - (0,0,0) = (k_x,k_y,k_z)$ — or a direction that points from the point to the centre — $(0,0,0) - (k_x,k_y,k_z) = (-k_x,-k_y,-k_z)$. Evidently, this corresponds to a change in the referential, and, in conjunction with the information of the absorbing plane, will present in which hemispheres are the incidences and the reflections. For this work, the convention adopted will be $(k_x,k_y,k_z) - (0,0,0) = (k_x,k_y,k_z)$ — "outward" vectors.

In the specified configuration — θ measured as in Figure 2 and plane waves propagating away from the radiation sphere — the incident and reflected powers averaged on the azimuth, $W_{\text{ref}}(\theta)$ and $W_{\text{inc}}(\theta)$ respectively, are given by Equation (38), which are calculated numerically. Another point that should be noted is that the wavenumber spectra are calculated on a homogeneously distributed basis. This can represent a problem for the numerical integration, as the azimuth intervals — $\mathrm{d}\phi$ — are not constant. A solution is to interpolate the spectra into an evenly-spaced mesh. In this research, the selected interpolation spacing was $\pi/60$ rad $= 3^o$. Thus, the numerical calculation of $\alpha(\theta)$ was done using the trapezoidal rule, with $\mathrm{d}\phi = \pi/60$. Moreover, since $1/2\pi$ is present in both the numerator and the denominator of the ratio in Equation (37), the multiplications cancel out and do not need to be computed.

3.6 Isotropy

From a third-octave or octave averaged wavenumber spectrum, the process of calculating the isotropy consists of finding its spherical harmonics decomposition and calculating Equation (42) or Equation (43). The spherical harmonics decomposition was done using the "SHTools" toolbox for MATLAB, developed by Fahim (2019). Fahim's algorithm calculates the spherical harmonics through a least-squares solution using the pseudo-inverse matrix.

4 EXPERIMENTS AND RESULTS

Because the plane-wave decomposition can be used to calculate both the absorption and the diffuseness, two different experiments were conducted to examine each aspect individually. This chapter is dedicated to analysing both applications in what concerns their setups, techniques, results, and what conclusions can be drawn.

4.1 Experiment #1 - Experimental Assessment of the Absorption and the RTF Reconstruction of a Room Using the Wavenumber Spectrum

This experiment had the objective of exploring the capabilities of plane wave decomposition in measuring the absorption of a surface and reconstructing the RTF in a common laboratory room. For that, an array of 120 randomly generated positions was generated inside a rectangular volume of 0.40 m $\times$ 0.10 m $\times$ 0.17 m. Aside from these, 30 points were also measured for comparison with their reconstructions. Figure 11 displays the sequential array, the reconstruction points, and the robot's reference.

Figure 11 – Microphone positions. Dots (green): points measured for the inverse problem (random array). Triangles (magenta): points measured for reconstruction error evaluation. Square (yellow): robot reference.

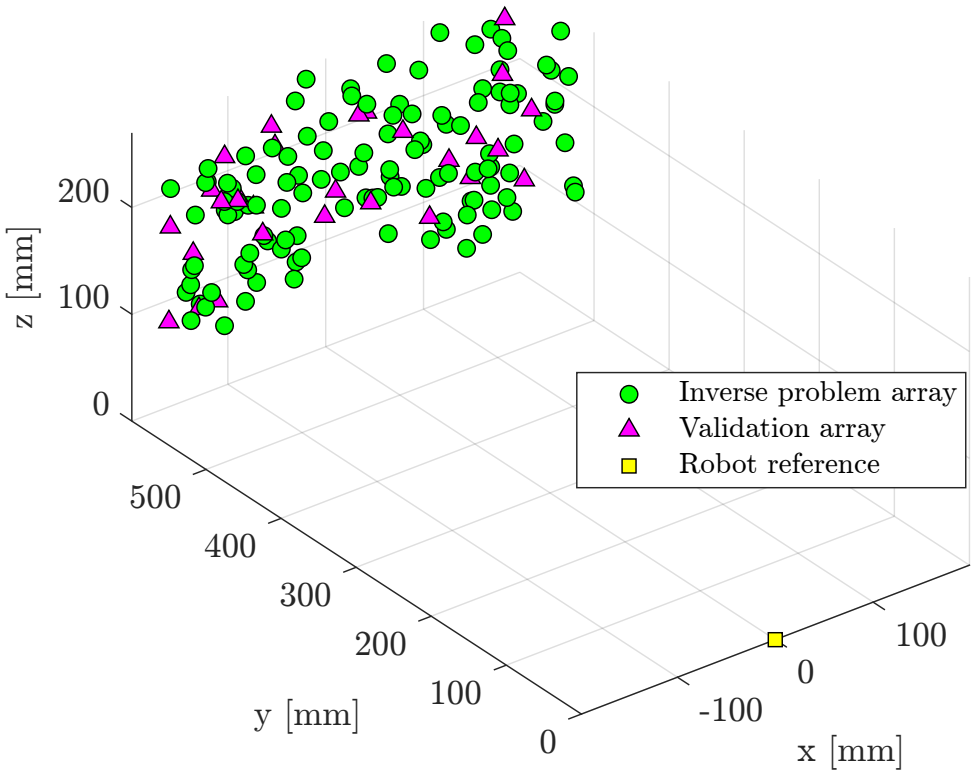

Source: own authorship (2024).

The robot was placed in such a way that the array's centre's distance to the surface was 0.30 m. The closest point to the surface was approximately 0.15 m of it. The room was a common laboratory room (room EK-019 at UTFPR - Ecoville Campus), with approximately 11.8 m $\times$ 5.3 m $\times$ 3.3 m, and inside, there were pieces of furniture and equipment, resembling a potential *in situ* condition. A glass wool surface of 10.8 m^2 (3.6 m$\times$3.0 m), with 40 kg/m^3 of density and 50 mm thickness was put in one of the walls to serve as the main absorbing surface, and thus the surface of interest for the measurements. Figure 12 displays roughly the position of the glass wool panel, the array and the dodecahedron source inside the room.

Figure 12 – Upper view of the room displaying the position of the absorber (yellow), the array (red) and the sound source (black).

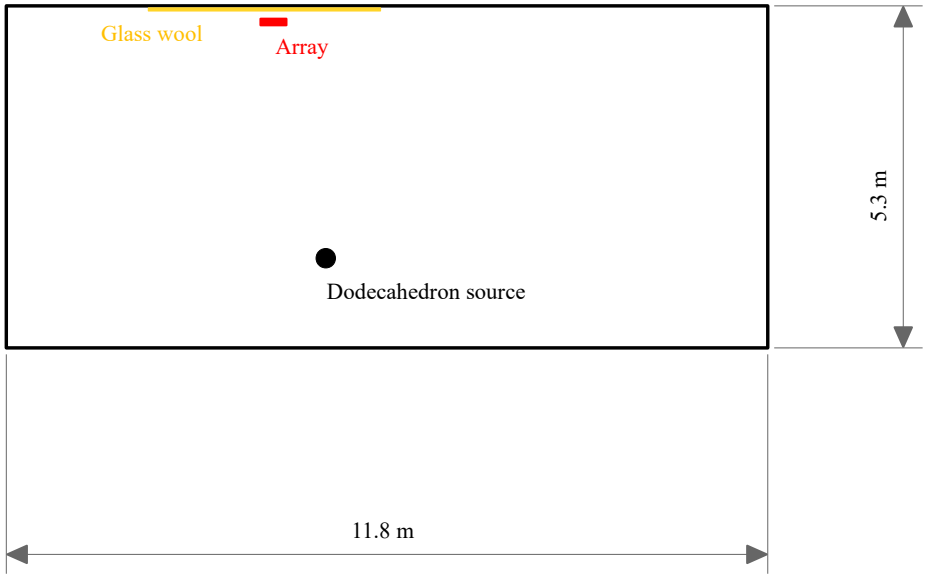

Source: own authorship (2024).

The sampling frequency employed was 96000 Hz, with $2^{19} = 524288$ samples, amounting to a sweep that lasted 5.46 s. The choice of a 96000 Hz was to use as much of the sound interface's capabilities. However, using such a high sampling frequency generates a very large volume of data, which becomes unhandy. Furthermore, such a refinement in discretized frequency also makes it so that processing the data takes a very long time. This motivated the change for a smaller sampling frequency in further experiments.

In this experiment, three different aspects of plane wave decomposition were approached. First, the reconstruction of the RTF of the sound field in a randomised set of microphone positions was compared to measurements of the RTF in these positions. The reconstruction errors using increasingly more populated and dense arrays — 80, 100, and 120 microphone positions randomly generated inside the same rectangular volume — to measure the angular spectrum were calculated for third-octave bands. The reconstruction processes display similar errors in the lower and middle frequencies for all array cases. However, the general behaviour of the reconstruction error in high frequencies had a less steep increase for the case with more microphones.

Secondly, the analysis of the energy mappings for the third-octave average spectra was done. The source incidence, the reflection of the absorber, and the other reflections of the room were identified. The reduction in the energy level when comparing the incidence and reflection of the absorber indicates that the difference in energy is being absorbed by the glass wool. The absorption of the energy is especially intense at higher frequencies, as is expected for a porous material such as glass wool.

Finally, the sound absorption coefficient of the glass wool was calculated from the third-octave wavenumber spectrum using Nolan's proposed approach (NOLAN, 2020) to find the incidence-dependent absorption and then using the Paris' formula. The measured absorption displays coherence with the absorption values available in the literature for most bands.

Overall, the techniques proposed by Nolan (2020) and Fernandez-Grande (2016) were utilised successfully.

4.1.1 Sound Field Reconstruction

The reconstruction of the RTF was done in 30 evaluation points. The relative error between the reconstructed transfer function and the measured transfer function was calculated following the metric defined in Equation (46). The value $\varepsilon_{\%}$ is then averaged across the 30 reconstruction points and then inside the third-octave bands. The reconstruction relative errors were calculated for three wavenumber spectra cases, calculated from 80, 100, and 120 microphone positions. The average relative errors from the 100 Hz to the 2500 Hz third-octave bands are shown in Figure 13 (circles, with the dashed line added to avoid parallax).

It can be promptly noticed that, indeed, the reconstruction at lower frequencies is more accurate than at higher frequencies. The reconstructions for all cases perform well between the 100 Hz and the 630 Hz band, with a relative percentage error limited to under 6.0%. The differences in the errors start to be visible from the 800 Hz band onward. Generally, the 120 positions microphone array presents the smallest average reconstruction errors. Another thing worth noticing is that at the 1600 Hz band, the error for the 80 microphone case is marginally smaller than the error for the 100 microphone case. This can be because of the different microphone dispositions that influence the numerical aspects of the regularisation, such as condition number and column redundancy (RICHARD; FERNANDEZ-GRANDE, 2019), which in turn influence the calculated angular spectrum. The smallest percentage error value for the 120 microphones case is in the 500 Hz band, at 2.1%. Between the 400 Hz band and the 630 Hz, the error for the 120 microphones case is limited to under 3.0%.

Another point of notice is the increase in errors with the increase in frequency. From 2000 Hz onward, the error is always above 10.0%, and it rises following the increase in frequency, being comparable to the measured values. This can happen due to a series of factors, such as the number of plane wave directions in the wavenumber sphere or a badly discretized region of the space in the array i.e. regions in which the microphone spacing is too

Figure 13 – Average relative reconstruction error from 100 Hz band to 2500 Hz band. 80 positions: red circles. 100 positions: green circles. 120 positions: blue circles.

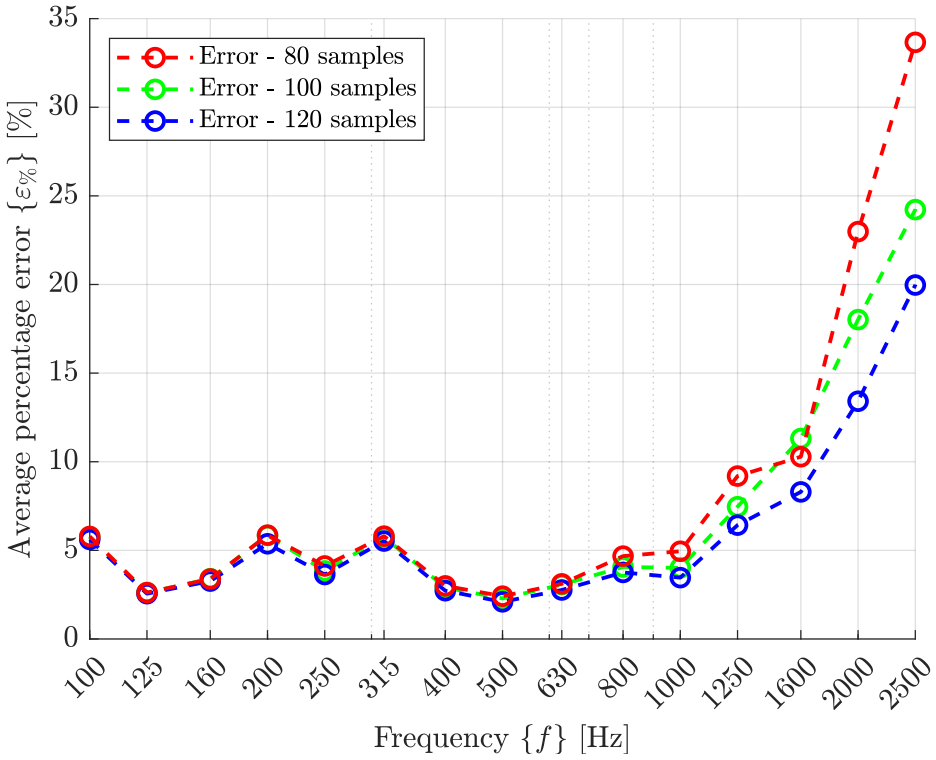

Source: own authorship (2024).

large because the robot cannot reach the in-between positions. Evidently, for the number of directions in the wavenumber domain, a set of factors must be taken into account between the desired reconstruction error, the processing capabilities of available hardware, and the numerical errors that can increase due to the $\mathbf{H}$ matrix being ill-conditioned. As the frequency increases, the radius of the wavenumber sphere grows, and the spacing between the directions of reconstruction also grows. Nolan and Xiang (2023) presents that there is a limit to how much the number of directions can make a model better. For 1 kHz, 1000 plane waves are able to represent the sound field without a significant loss of information. However, it should be pointed out that the analysis in (NOLAN; XIANG, 2023) was carried out for a single frequency and that the inverse deviance information criterion (IDIC) analysis for a larger range of frequencies is still a future consideration.

Figure 14 shows the reconstruction (blue solid line) and the measured transfer function (green dashed line) at the evaluation position number 30, between 89.1 Hz and 2818 Hz (the lower limit of the 100 Hz third-octave band and the upper limit of the 2500 Hz third-octave band), divided into 4 parts for better visualisation of the curves. This reconstruction was done using the 120 positions array. It can be noticed that up to 630 Hz, indeed, the reconstruction is very accurate. Beyond this frequency, a few discrepancies, especially overshooting of the amplitude at anti-resonance frequencies become recurrent with frequency increase, which is related to the increase in the average error of Figure 13. The errors in the reconstructed modes

also rise in a less intense manner. Moreover, for higher frequencies (notably on Figure 14d) some discontinuities can be noticed (after 1600 Hz and after 2500 Hz). Errors of this nature likely occur due to the lack of restrictions on the existence of derivatives and second derivatives in the regularisation process using L-curve and Tikhonov regularisation, which in turn carry over when solving the direct problem. Figure 15 displays detailed views centred at 1700 Hz (Figure 15a) and 2500 Hz (Figure 15b). In Figure 15a a discontinuity error can be detected at near 1692 Hz and an undershoot error can be noticed near 1698 Hz. In Figure 15b a discontinuity error can be noticed at 2540 Hz, and sequential overshoot and undershoot can be noticed between 2570 Hz and 2590 Hz. Because these errors take place more often in higher frequencies, a higher modal density will mean that the average reconstruction error will also increase because of the accumulation of errors.

4.1.2 Sound Energy Mappings

Since the wave number vectors are comprised solely of propagating plane waves distributed on the surface of a sphere, one can plot the magnitude of the plane waves as a function of the directions of travel. The graphics were made using Eckert III projections to avoid excessive distortion on the poles, and the elevation (θ angle) is measured with relation to the xy plane. For this, the averaged spectra needed to be interpolated into an evenly-spaced grid. The interpolation was done with a resolution of $\pi/60$ rad. The maps for the 400 Hz, 1000 Hz, 1500 Hz, and 2500 Hz are on the left side of Figure 18, respectively. The map on Figure 18b also indicates some general directions, such as the ceiling, the ground, the source and the room's sides. The energy dynamic range was limited to 15 dB to better visualise the incidence and the reflections. In that context, although it may seem that there is no energy reflected on the maps on Figures 18c and 18d, the attenuation caused by the absorber makes it so that the energy is small enough to be under the defined threshold.

Some artefacts can be seen near the $(\phi, \theta) = (180^{\text{o}}, 0^{\text{o}})$ positions. These are caused because the interpolation originally is calculated for angles nearing -180^{o} to angles nearing 180^{o}, leaving the azimuth limits unfilled. Notwithstanding, it can be noticed that, indeed, with an increase in frequency, the specular energy that is reflected by the absorber ("northern" hemisphere) decreases in level, which indicates that the surface is absorbing the sound irradiated by the omnidirectional source. Moreover, it can be seen that with the increase in frequency, the lobes that denote the incidence and specular reflection get smaller, such as is expected for this technique (BRANDÃO; FERNANDEZ-GRANDE, 2022).

Furthermore, even with the averaging on the third-octave bands, reflections that are not related to the surface of the absorber can be noticed in all displayed maps. These reflections from other directions of the room contribute to the calculation of an absorption coefficient that depends on the direction of incidence and, subsequently, the diffuse incidence absorption coefficient calculated by the Paris formula, even in a small room with a sound field that is

Figure 14 – Comparison between the reconstructed and measured RTFs at evaluation point number 30. Blue solid line: reconstruction. Green dashed line: measurement.

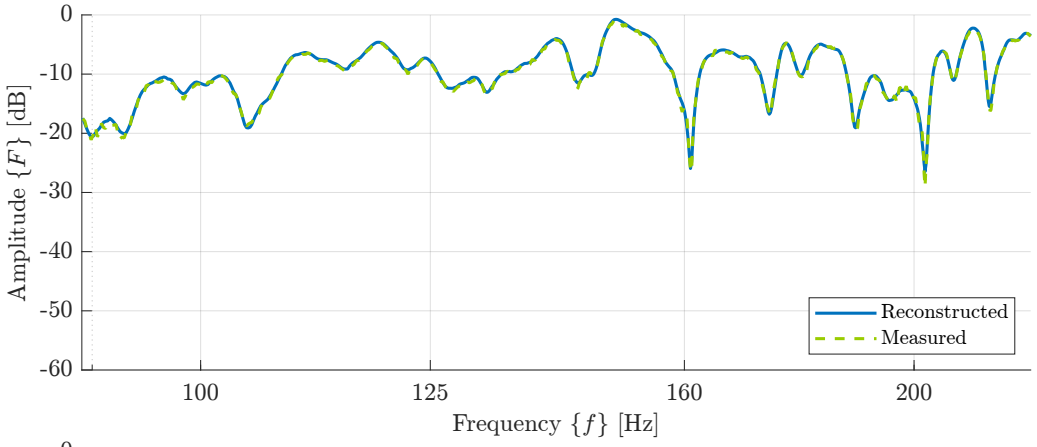

(a) 89.1 Hz to 224 Hz.

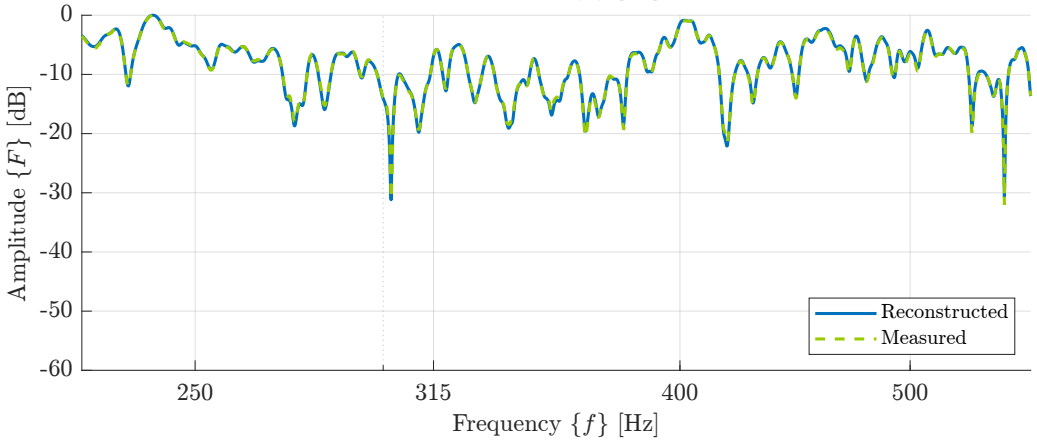

(b) 224 Hz to 562 Hz.

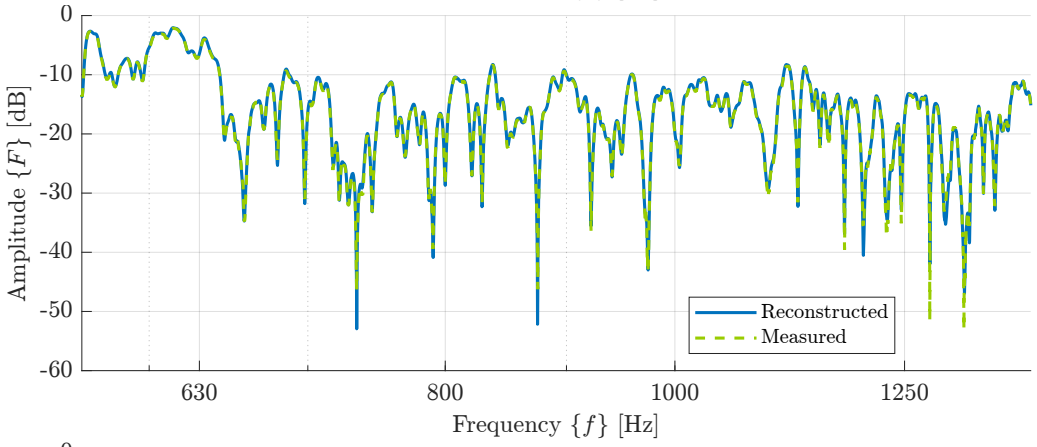

(c) 562 Hz to 1413 Hz.

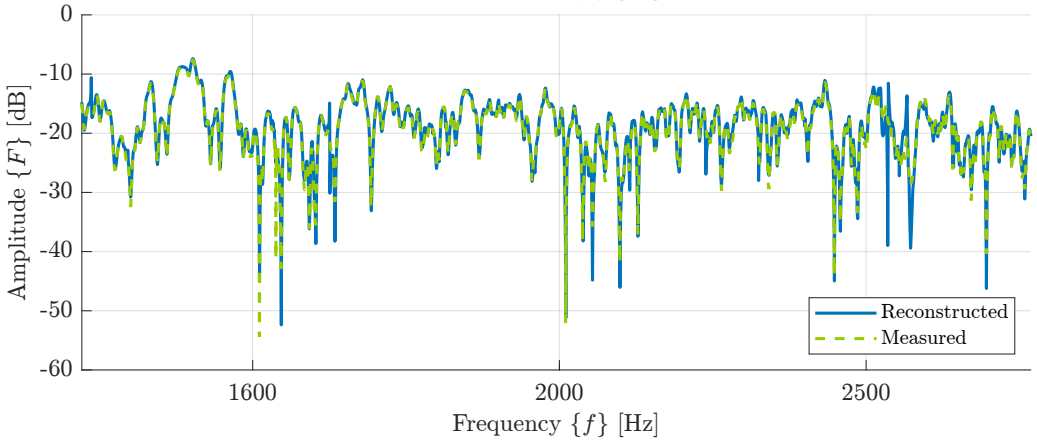

(d) 1413 Hz to 2818 Hz.

Source: own authorship (2024).

Figure 15 – Details of the discontinuities. Blue solid line: reconstruction. Green dashed line: measurement.

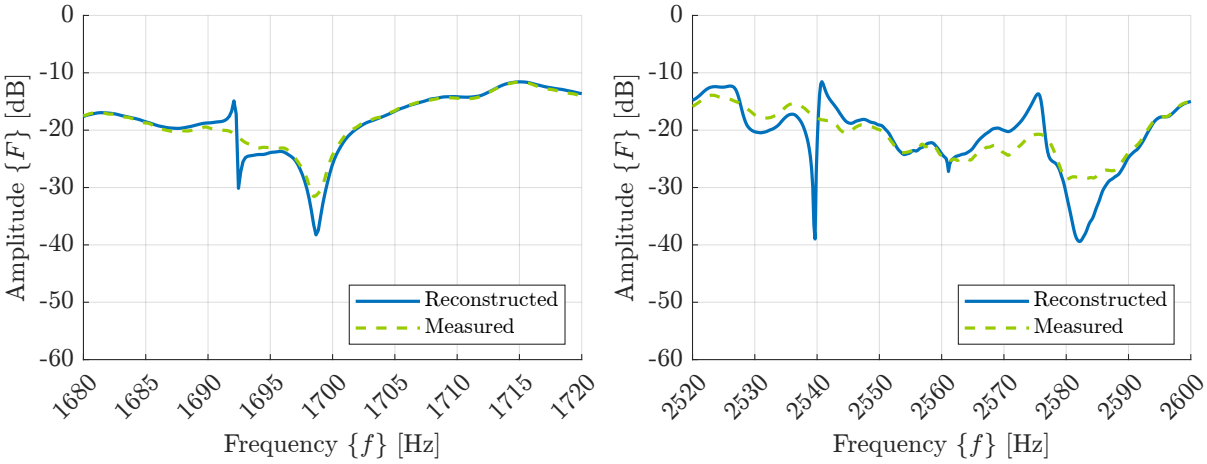

(a) 1680 Hz to 1720 Hz. **(b) 2520 Hz to 2600 Hz.**

Source: own authorship (2024).

not very diffuse. This corresponds to an advantage of this technique, as with a relatively simple excitation setup composed of an omnidirectional source conveniently positioned beyond the critical distance, it is possible to obtain incidence from several directions from only one measurement process.

4.1.3 Absorption Determination

The absorption of the glass wool surface was calculated following the theory proposed in Section 2.6.5. For that, the absolute value of the wavenumber spectrum needed to be averaged in third-octave bands to remove biases that could occur in specific discrete frequencies (NOLAN, 2020). Then, the incidence-dependent absorption was calculated for each third-octave band. The incidence-dependent absorption for the 400 Hz, 1000 Hz, 1500 Hz, and 2500 Hz are shown on the right side of Figure 18.

An interesting occurrence happens in the 250 Hz band. Figure 16 shows the map, and Figure 17 displays the directional absorption of that band. It should be noted that θ is the elevation measured from the z axis varying from 0^o to 180^o, while the incidence angle ϑ goes from 0^o (direct incidence) to 90^o (parallel incidence).

It is noticeable that the map shows energy coming from the reflected region (left side of the upper hemisphere) with the same intensity as the incident energy from the source direction. This makes it so that in the 250 Hz band (Figure 17), the absorption values are negative after approximately 51^o ($\frac{17\,\pi}{60}$ rad). This corresponds to one of the downsides of this technique. Nolan (2020) states that at lower frequencies, the absorption values at angles of incidence almost parallel or parallel to the surface are underestimated due to what the referred author calls “leakage” of the incident energy into the reflected energy region (“northern” hemisphere).

Figure 16 – Energy map for the 250 Hz band.

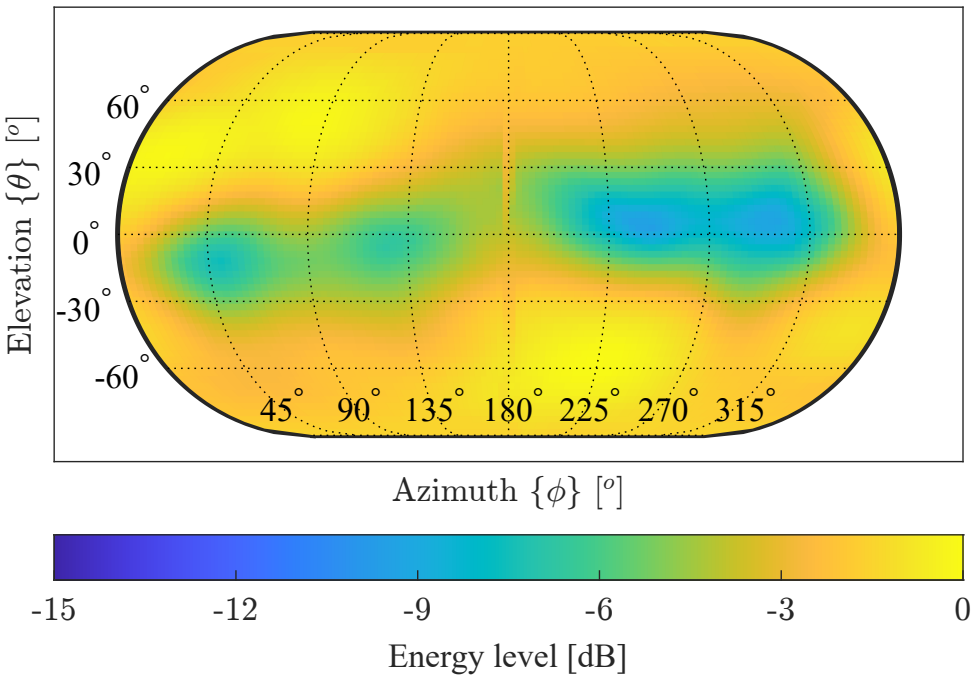

Source: own authorship (2024).

In extreme cases, such as the one in Figure 17, the absorption values calculated can reach impossible negative values. This can happen due to limitations on the wavenumber resolution provided by the array (NOLAN, 2020), due to the smoothing of the solution caused by the Tikhonov regularisation process, which, when happening near the equator, makes it so that some of the incident energy is considered as reflected energy. Another factor can be the model not considering evanescent waves.

Figure 19 shows the diffuse incidence absorption calculated with Equation (39) for both the *in situ* measurement (circles) and the absorption calculated by Miki's model (asterisks), from the 315 Hz to the 2500 Hz third-octave bands.

Figure 17 – Directional absorption for the 250 Hz band.

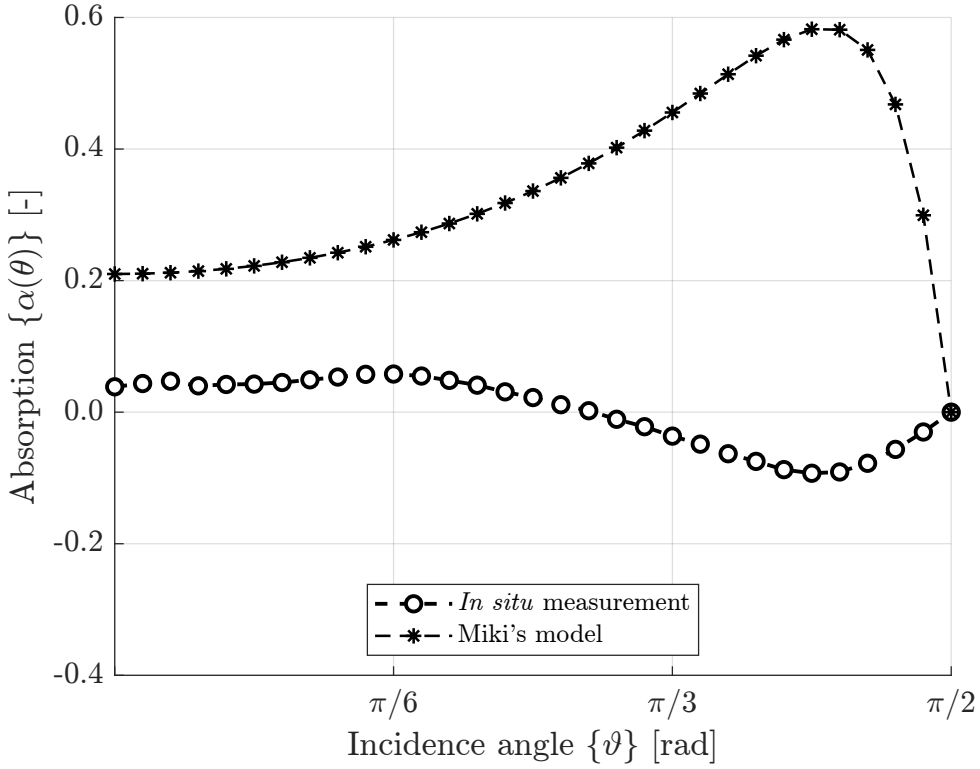

Source: own authorship (2024).

Figure 19 – Diffuse field absorption coefficient per third-octave band, calculated from third-octave averages of interpolated wavenumber spectra (circles), reference absorption values calculated using Miki's model (asterisks), commercial catalogue values of the absorption (triangles, in octave bands).

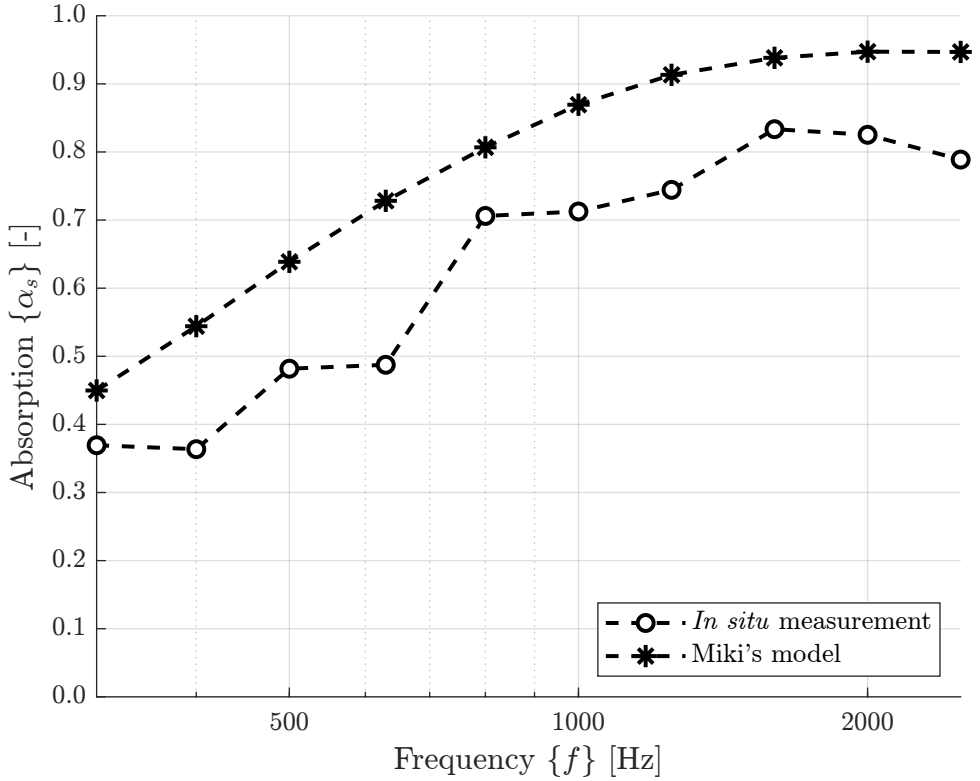

Source: own authorship (2024).

Figure 18 – Sound energy mappings (left side) and directional absorption (right side) for the 400 Hz (Figure 18a) band, the 1000 Hz (Figure 18b) band, the 1600 Hz (Figure 18c) band, the 2500 Hz (Figure 18d) band.

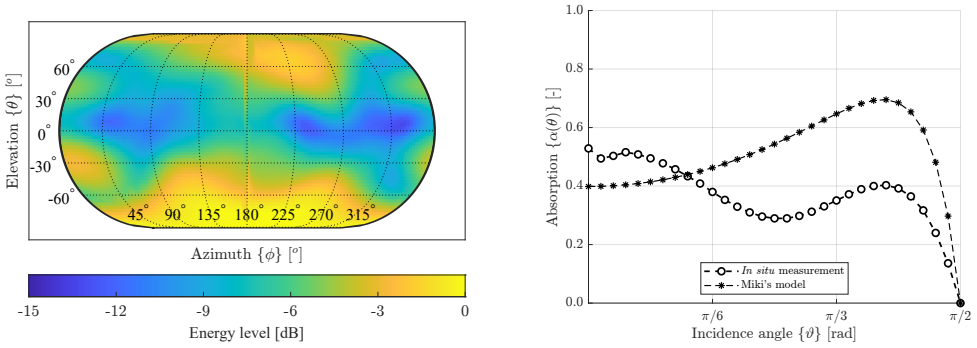

(a) 400 Hz.

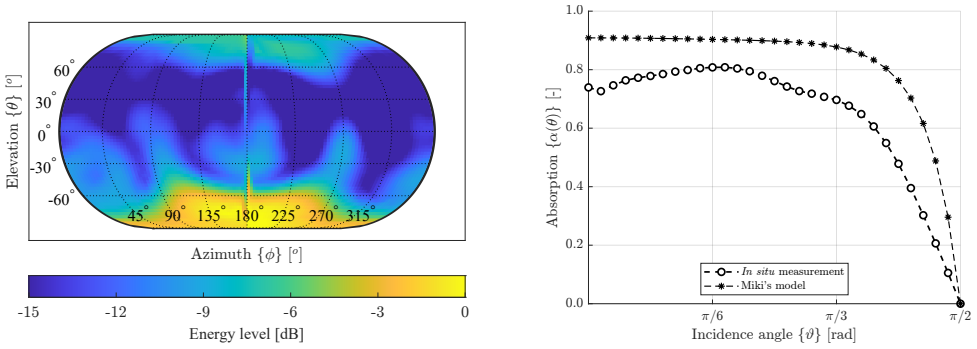

(b) 1000 Hz.

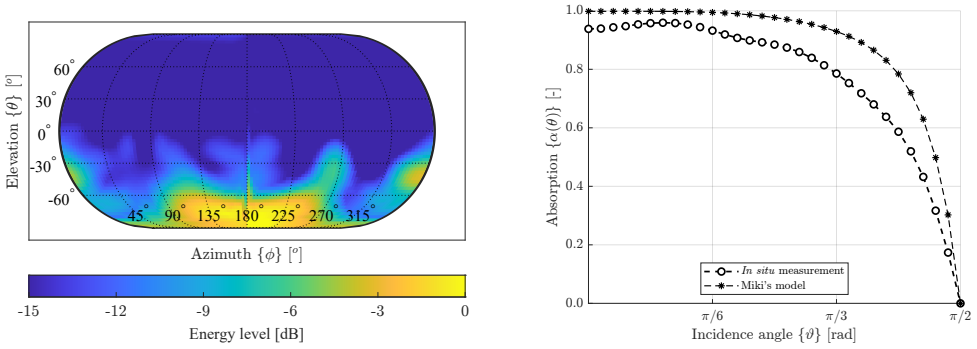

(c) 1600 Hz.

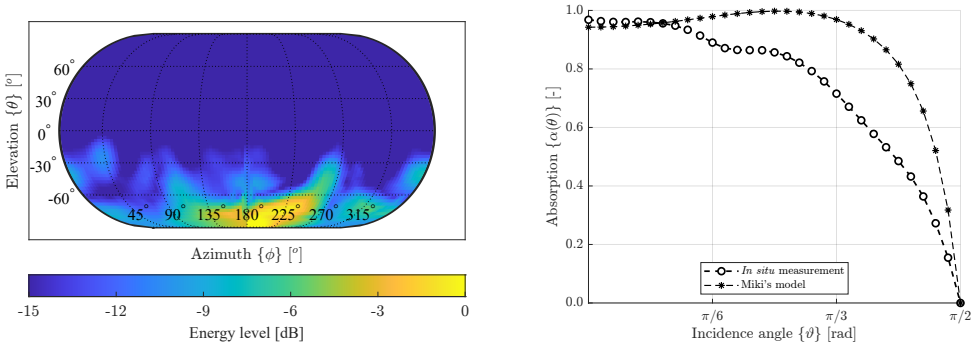

(d) 2500 Hz.

Source: own authorship (2024).

The graphic displays a general trend of rise in absorption following the increase in the frequency, which is coherent with what is expected for this type of material (BRANDÃO, 2016). Due to the severe underestimation in the 250 Hz band in the proposed *in situ* method, the displayed frequencies were chosen to be above that. The *in situ* values also display coherence with the values diffuse incidence absorption coefficients calculated by applying the Paris formula. Both curves display a similar evolution between 315 Hz and 2500 Hz, with the *in situ* experimental values being, on average, 0.16 smaller than the model values. The differences between the *in situ* and the values calculated by Miki's model can be attributed to the fact that the Paris formula is an approximation, as it considers the existence of a perfectly diffuse sound field (KUTTRUFF, 2009) and an infinite absorbing sample. Another factor that can be responsible for these errors is the measurement distance between the array and the sample. Richard and Fernandez-Grande (2019) show that, even though the spherical array has a better condition number than the planar array, the planar array display better results because the constraints related to the hardware allow for a measurement closer to the absorbing surface resulting in more accurate surface impedance measurements. Moreover, the relative underestimations of the proposed technique, when combined, result in an underestimation of the result of the Paris formula. Combining these factors with other errors from the calculation of the average absorption concerning the incidence angle can lead to errors when calculating the diffuse field absorption coefficient. When taking into consideration the commercial values informed for this sample (Saint-Gobain Vidros S.A. Divisão Isover, 2009), both the *in situ* and the model values are, in general, smaller and closer to each other than the values obtained using the reverberation chamber method. The catalogue values, aside from being much larger than the model and *in situ* values, also display one value outside the possible range — 1.1 for the 1000 Hz octave band — represented by the dotted line where $\alpha_{\mathrm{s}} = 1.0$. The only band where there is reasonable coherence is the 2000 Hz octave band.

4.1.4 Considerations

The experiment described in this paper was the calculation and polar mapping of the wave-number spectrum, the reconstruction of the sound field using the wavenumber spectrum, and the evaluation of the absorption of a surface of interest in installation conditions. In this experiment, the room had one surface covered with 10.8 m^2 of 40 $\mathrm{kg/m}^3$ glass wool, a porous absorbing material, and 150 RTF measurements in random positions were performed — 120 for the sequential array and 30 for comparison with the reconstructions. The calculation of the inverse problem's solution and the reconstruction of 30 RTFs were evaluated for a range between the 100 Hz and 5000 Hz third-octave bands for arrays of 80, 100, and 120 positions. The case using 120 positions displayed the smaller errors, limited to under 10% until the 1600 Hz band. For higher frequencies, the errors become even more pronounced — over 10%

— for all cases, most likely due to the excessive spacing between plane-wave directions. The processing was deemed successful.

The mapping of the sound field for each band in the proposed frequency range showed that, indeed, there's an increase in absorption when the frequency rises. The mapping was also important from an operational standpoint when implementing Equation (37). Moreover, some phenomena related to excessive smoothing of the solution or array characteristics in the wavenumber domain could be noticed on the 250 Hz band. This type of problem cannot be noticed only by analysing reconstruction errors, as the solution can solve the direct problem with relatively small errors but is a misrepresentation of the sound field in the angular domain.

The plane-wave decomposition allowed the identification of the direct incidence from the sound source over the absorbing sample, the reflection of the surface of interest, and also spurious reflections caused by the other regions of the room and influenced by the position of the sound source. This is important because the lack of hemispherical-isotropic incidence over the sample can be one of the causes of the underestimation of the absorption coefficient values obtained, along with factors influenced by the array characteristics. When compared to values calculated with Miki's model (MIKI, 1990), the *in situ* absorption coefficients display a similar behaviour in relation to the frequency, with an apparent systematic underestimation, between the 315 Hz and the 2500 Hz bands. For bands of frequencies lower than the mentioned, phenomena related to the underestimation at 250 Hz made it so that the results before and including this band were considered untrustworthy. When comparing the *in situ* and model values with the informed commercial values, the latter values are much higher and even beyond the possible range. Nevertheless, the absorption values show an overall behaviour consistent with models present in the literature (BRANDÃO, 2016) for that type of material and verified by comparing the energy distributions for increasing frequencies.

4.2 Experiment #2 - Experimental Assessment of Sound Field Conditions and Decay Using Plane Wave Decomposition

This experiment aimed to compare decay characteristics for different absorption configurations inside a reverberating environment with the isotropy indicator proposed by Nolan (NOLAN, 2019), which uses the 1-norm, and the isotropy indicator using the 2-norm. The utilised array was composed of 180 positions randomly generated on a 0.60 m $\times$ 0.10 m $\times$ 0.40 m, that were used as input for the plane wave decomposition inverse problem. Aside from those, 30 random positions for reconstruction were also specified and measured for comparison. Fifteen positions were determined to be inside the array generation volume, and the remaining 15 were generated on the plane where $y = 0.49$ m, outside the generation volume. This was done to detect not only the reconstruction error in the broad sense but also if there is any sensible difference between interpolation errors for points inside the

same volume as the input positions and extrapolation errors for points outside of the generating volume. Figure 20 displays the sequential array, the reconstruction points, and the robot's reference.

Figure 20 – Microphone positions. Dots (green): points measured for the inverse problem (random array). Triangles (magenta): points measured for reconstruction error evaluation. Square (yellow): robot reference.

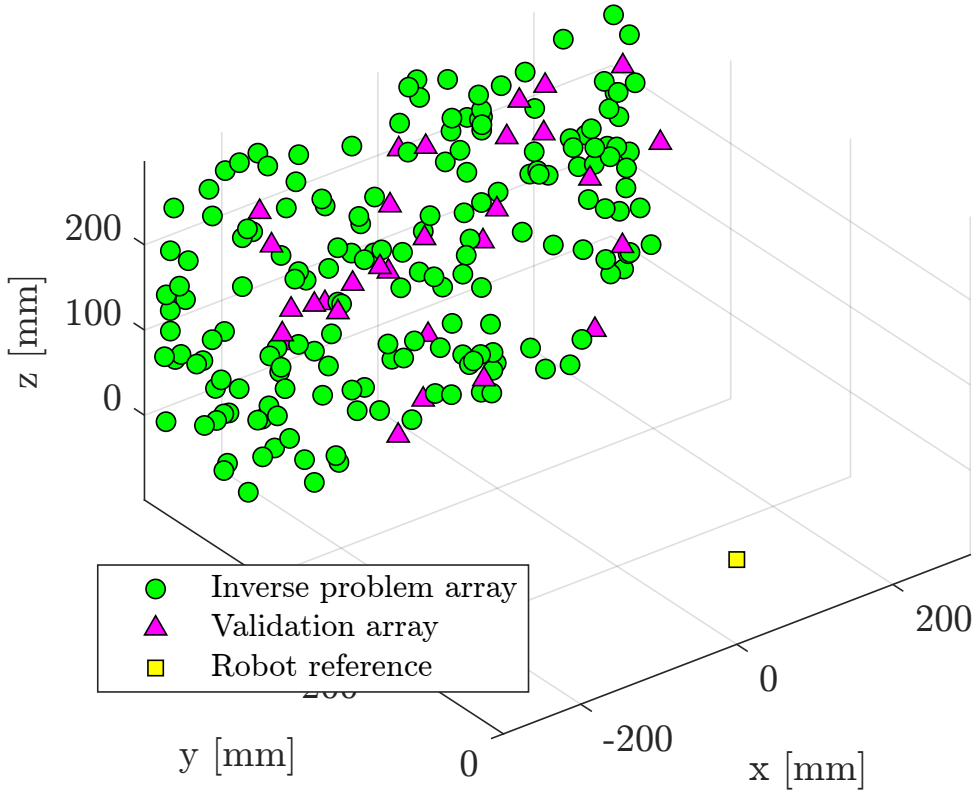

Source: own authorship (2024).

The reverberation chamber measured is the reverberation chamber from the Civil Engineering Department of UTFPR. Some data on it was described on (SPROROWSKI; ALBERTS, 2018). It is worth remembering that this reverberation room was originally designed to measure sound insulation. It is much smaller than the ISO 354 recommended volume and not precisely rectangular, resembling two coupled smaller rooms with a frame for the insulating materials' samples. Figure 21 displays the positioning of the absorbers inside the reverberation room and also displays the measurements of the floor plan of the reverberation chamber. The sections of the chamber will be hereafter referred to as "volume 1" (51.84 m^3) and "volume 2" (57.02 m^3) as marked in Figure 21. The total volume of the enclosure is 115.01 m^3. As for the absorption configurations, three different dispositions were used: concentrated sample (Figure 21b), divided into three areas (Figure 21c) and divided into five areas (Figure 21d).

The array was positioned in 3 different positions inside volume 1 of the room, as shown in Figure 22 (red rectangles). Although the positions were chosen at random, the reach of the robot's drive and control cables were taken into consideration, as they needed to reach one of

Figure 21 – Absorption configurations inside the reverberation chamber.

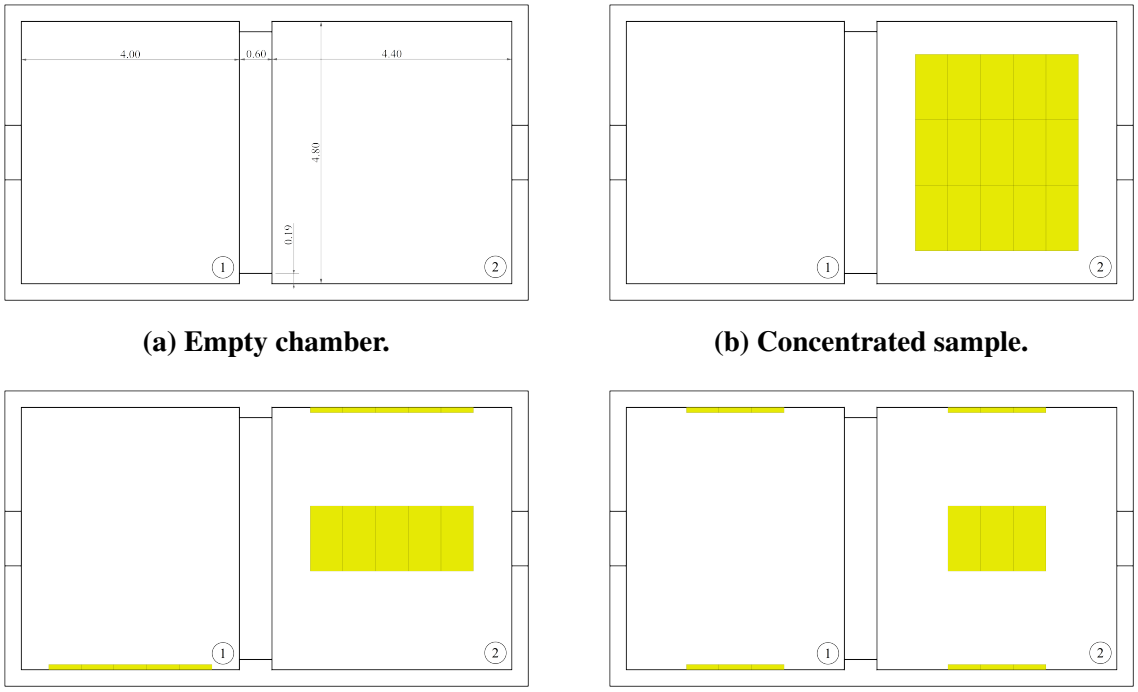

(a) Empty chamber. **(b) Concentrated sample.**

(c) Three areas configuration. **(d) Five areas configuration.**

Source: own authorship (2024).

the openings in the room so that they could be connected to the control unit. Hence all the array positions are in volume 1. Because the robot was placed on a pedestal with a large base, it would not be possible to place the robot and the sample both in volume 1 in the concentrated sample case, and thus, the sample had to be placed in volume 2. The enclosure was excited with the source in two different positions (yellow diamonds in Figure 22), one in volume 2 and one near one of the corners in volume 1.

The sound source positions were selected so that position S1 would be close to the initially concentrated sample. As for position S2, the source would be near a corner of the room to excite as many modes as possible.

4.2.1 Sound Field Reconstruction

The sound field reconstruction was evaluated for all combinations of source array positions by solving the direct problem Equation (33) for each discretized frequency. Regarding the reconstruction errors, the general tendency was that the interpolation errors are smaller than the extrapolation errors, as expected. Out of all the absorption cases and excitation/measurement positions — a total of 24 reconstructions — two of them displayed outlying error results, displayed in Figure 23: excitation #1, array #2 for the empty chamber case (Figure 23a), and excitation #1, array #2 for the five areas divided absorber case (Figure 23b). It is interesting to remark that even in these cases, the general behaviour of the interpolation errors being smaller

Figure 22 – Array positions (red) and sound source positions (yellow) inside the reverberation chamber.

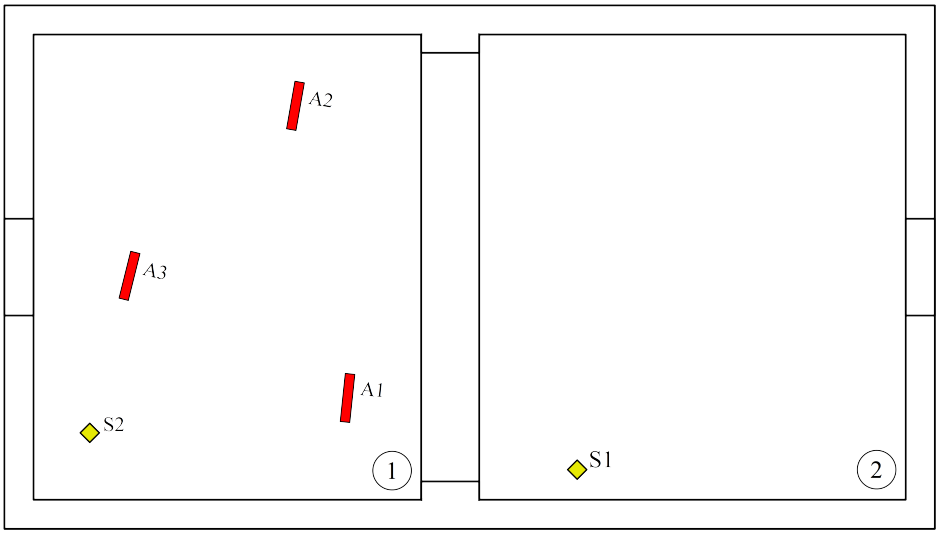

Source: own authorship (2024).

than the extrapolation errors remains. The only exception is the 200 Hz band on the excitation #1, array #2 for the five areas divided absorber case, in which the difference between them is so small it could be accredited to the calculation's own uncertainty.

Figure 23 – Average third-octave band reconstruction errors for outlier error cases. Red: general error. Green: interpolation error. Blue: extrapolation error.

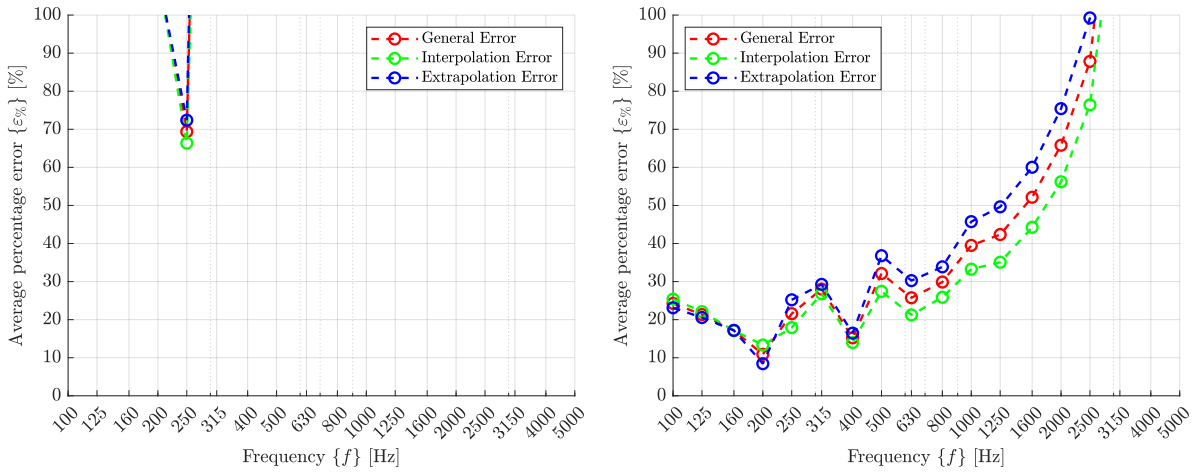

(a) Source #1, array #2, empty chamber case. **(b) Source #1, array #2, five area configuration.**

Source: own authorship (2024).

From analysing some of the room transfer functions measured for the outlier cases, there were no apparent measurement problems.

All other situations had the same behaviour on average. From that, one of the things that can be concluded is that the quality of the reconstructions does not depend on the measurement

position of the array or the source position. Figure 24 displays the average reconstruction errors for all excitation and measurement conditions excluding the mentioned outliers.

Figure 24 – Average third-octave band reconstruction errors for all excitation configurations (excluding outliers). Red: general error. Green: interpolation error. Blue: extrapolation error.

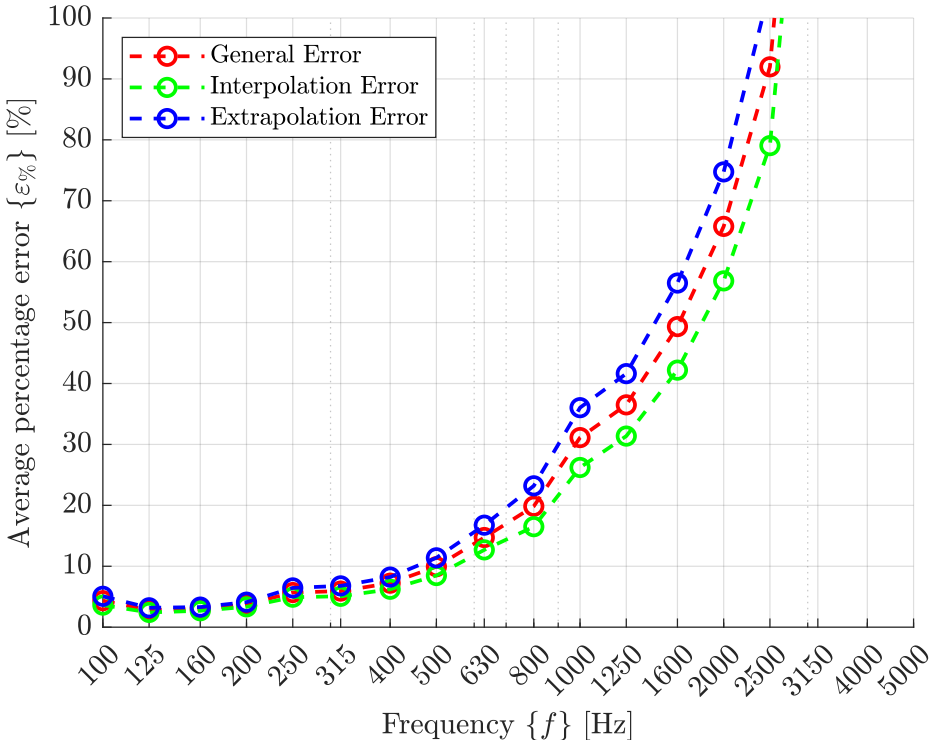

Source: own authorship (2024).

4.2.2 Numerical Considerations

Numerical problems such as the regularisation of Equation (26) can be analysed by means of the normalised Gram matrix (RICHARD; FERNANDEZ-GRANDE, 2019; FERNANDEZ-GRANDE; XENAKI; GERSTOFT, 2017)

$$\mathbf{\Gamma}_{i,j} = \frac{|\mathbf{h}_i^* \, \mathbf{h}_j|}{\|\mathbf{h}_i\| \, \|\mathbf{h}_j\|}, \tag{47}$$

which indicates the correlations between the columns of $\mathbf{H}$. Plane waves with similar directions of arrival result in values $\mathbf{\Gamma}_{i,j}$ closer to one. Naturally, the diagonal values, i.e. $i = j$, will equal 1. Operators that result in $\mathbf{\Gamma}$ closer to a diagonally dominant matrix, i.e. closer to an identity matrix, are easier to regularise. That is because the largest off-diagonal value gives the matrix coherence value μ, which bounds the condition number of the matrix, κ (RICHARD; FERNANDEZ-GRANDE, 2019). Literature (RICHARD; FERNANDEZ-GRANDE, 2019; FERNANDEZ-GRANDE; XENAKI; GERSTOFT, 2017) indicates that arrays that cause the

Figure 25 – Matrix coherence and conditions number of H.

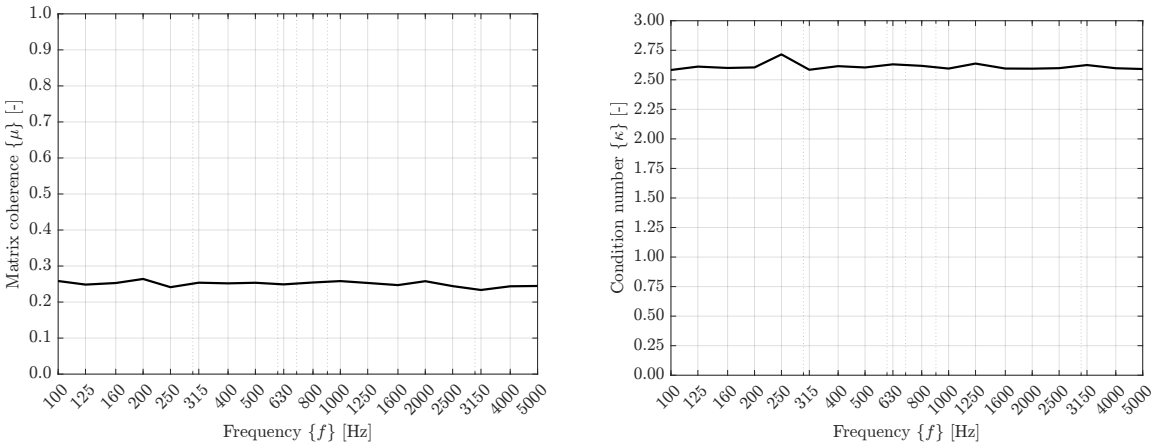

(a) Matrix coherence μ. **(b) Matrix condition number κ.**

Source: own authorship (2024).

matrix $\mathbf{H}$ to have redundancies, such as planar and spherical arrays, are more sensitive to noise and harder to regularise. These redundancies usually will appear as off-diagonal coefficients near the main diagonal. Figure 25 displays the coherence and condition number of the $\mathbf{H}$ operator for the array and the 1000 direction plane wave basis employed in this experiment. Figure 25a displays the matrix coherence μ for each third-octave band central frequency for the array from Figure 20, from 100 Hz to 5000 Hz. It can be seen that μ is almost constant for this frequency range, having a mean value of 0.25. It is remarkably smaller than the values shown for spherical and planar arrays on (RICHARD; FERNANDEZ-GRANDE, 2019), which means that $\mathbf{\Gamma}$ is closer to a diagonally dominant matrix for this array than for these other arrays' geometries. Figure 25b displays the condition number of $\mathbf{H}$ for each third-octave band central frequency for the array from Figure 20, from 100 Hz to 5000 Hz. The condition number is also almost constant at this frequency range, oscillating around 2.61, which is much smaller than the values for the types of array studied in (RICHARD; FERNANDEZ-GRANDE, 2019), which for some frequencies resulted in condition numbers of the order of magnitude of 10^{10}.

4.2.3 Energy Decay Analysis

In Subsection 2.3, the relation between the potential existence of a diffuse sound field and the shape of the energy decay curves was presented. Evaluating the combinations of measurement position and excitation, it is possible to observe the decay behaviour inside the array's generation volume — a relatively small region — and in several array positions inside the room for the different absorption configurations. Furthermore, the derivation of Sabine's reverberation time by Kuttruff (2009) depends on the approximation of the decay constants to an average, both spatially and in frequency. Given that the energy decay curves are usually displayed in logarithmic forms, a way of verifying this is to compare the decay curves with an

average adjusted curve of a first-degree function. This curve will have a first-order coefficient that is proportional to the exponential decay of the curves. The linear regression was calculated for values between -5 dB and -25 dB. The goodness of the fit is given by the R^2 values, which is the residual of the regressions, also averaged for each fit at each microphone position. Figure 26 displays the energy decay curves of 15 measured microphone positions for all excitation configurations in the empty chamber for the 125 Hz, 250 Hz, 500 Hz, 1000 Hz, 2000 Hz, and 4000 Hz. The decay constant is denoted by β. Thus, $\langle\beta\rangle_{\mathbf{r}}$ is the average value of the calculated decay constant in the measurement positions $\mathbf{r}$, and $\text{var}_{\mathbf{r}}(\beta)$ is its associated variance.

It can be seen that the decays are, on average, different for each frequency. All the linear regressions present good fits. It is also seen that the variance of the decay in all measured positions is relatively small in comparison to the values for the decay, which can be interpreted as a relatively small variation in the decay for each position in the measured region. When looking at all excitation conditions for the empty chamber, it is apparent that the average decay varies little with the measurement position. This indicates spatial independence in energy decay, in this "absorption case". It is also noticeable that these decays seem to be exponential or close to exponential from 500 Hz onward.

Figure 27 displays the decay curves and average adjusted decays for the case where the absorption is concentrated in one area. It can be seen that the decays, in this case, are not exponential throughout or can not be described by only one exponential. The variance of the decay constants also is larger than for the case without absorption in the room, which indicates a larger variation in the decay depending on the space. Another thing worth mentioning is that there is a correlation between the measurement position of the array and the decay for the lower frequencies.

For the three areas' configuration, some interesting changes occur, as it can be seen that all decays become faster — indicated by the more acute inclination of the EDCs — and the earlier portion of the decays for the 500 Hz and beyond third-octave bands become similar in inclination i.e. they present similar decay constants. Figure 28 displays the decays for the three areas' configuration. It can be noticed that the decay coefficients for the highest frequencies (500 Hz, 1000 Hz, 2000 Hz, and 4000 Hz) are very similar.

Figure 29 displays the decays for the five areas' configuration. The behaviour observed in the case with three areas is still present for the five areas configuration. The difference between the decay coefficients at lower frequencies (125 Hz and 250 Hz) and at higher frequencies (500 Hz, 1000 Hz, 2000 Hz, and 4000 Hz) is even higher.

A few conclusions can be taken from the observed behaviour of the decay when the absorption configuration changes. Figure 30 displays a direct comparison between each absorption configuration for a fixed array and source positions.

Figure 26 – EDCs for the empty chamber.

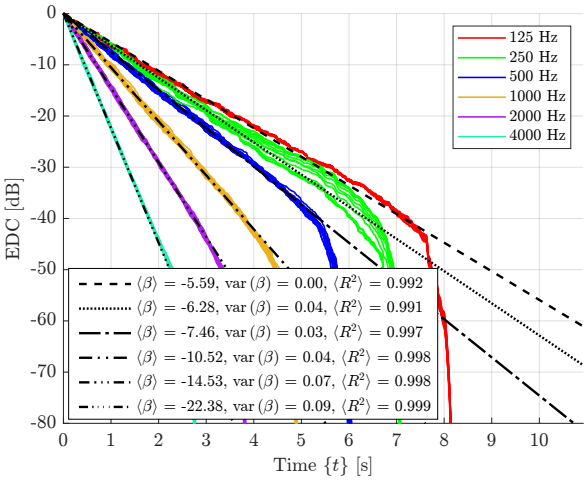

(a) Array #1, Source #1.

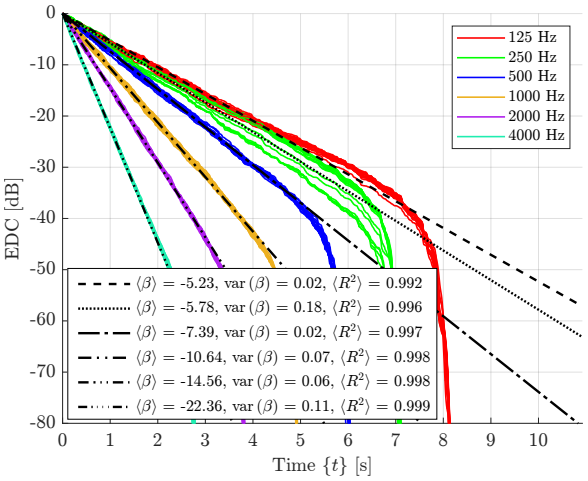

(b) Array #1, Source #2.

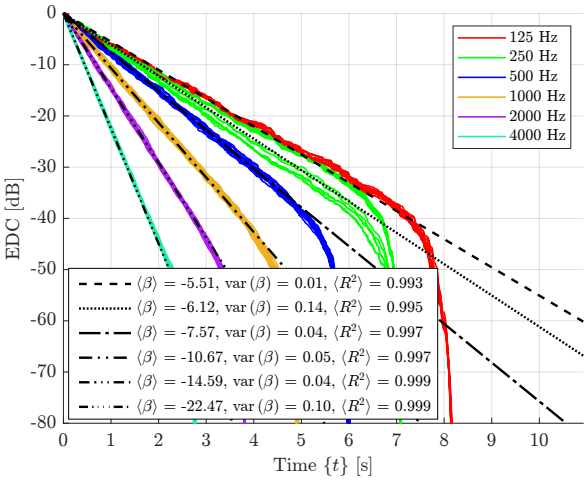

(c) Array #2, Source #1.

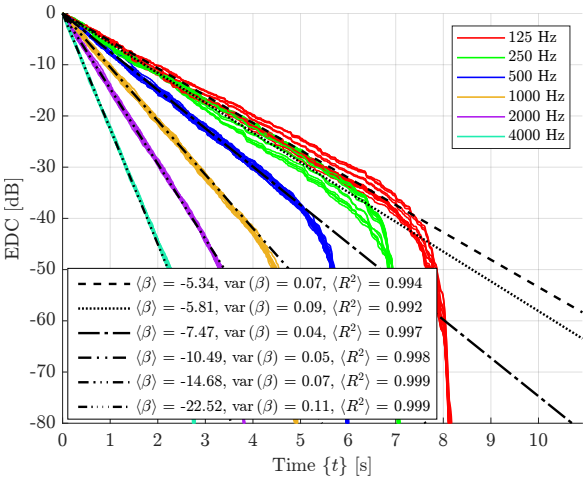

(d) Array #2, Source #2.

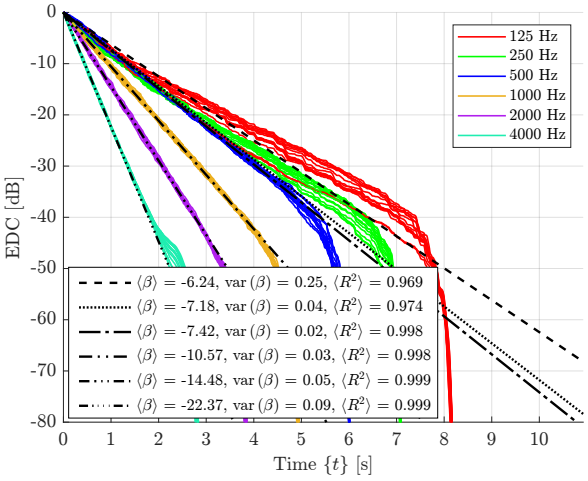

(e) Array #3, Source #1.

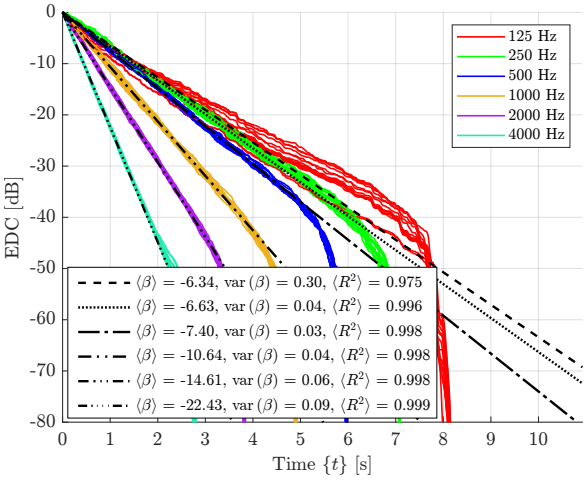

(f) Array #3, Source #2.

Source: own authorship (2024).

Figure 27 – EDCs for the concentrated absorption.

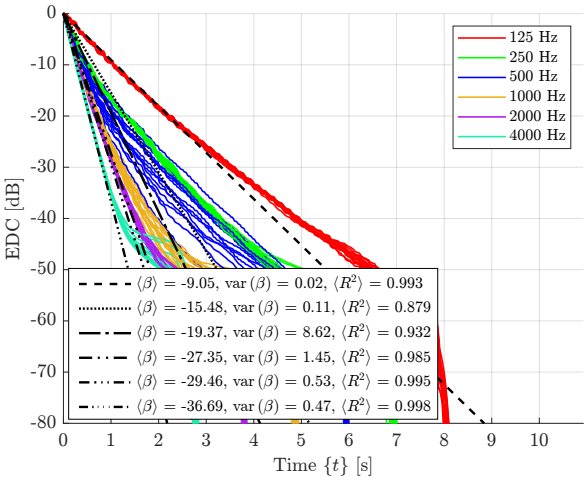

(a) Array #1, Source #1.

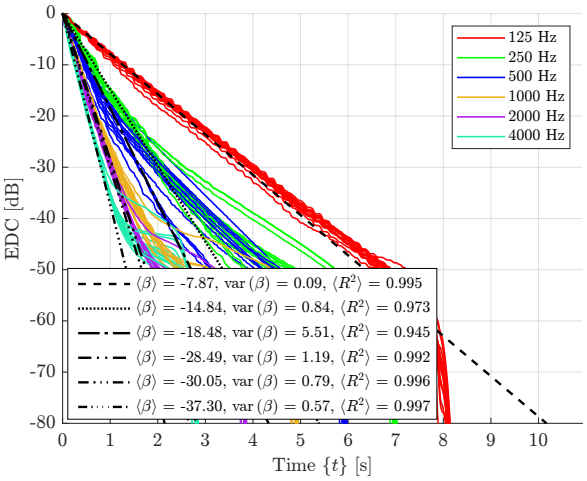

(b) Array #1, Source #2.

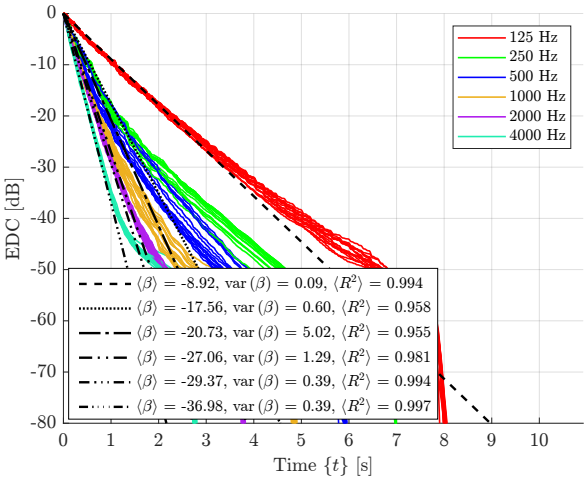

(c) Array #2, Source #1.

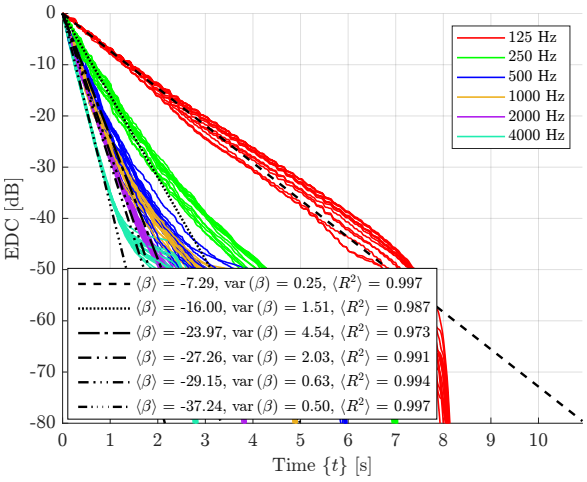

(d) Array #2, Source #2.

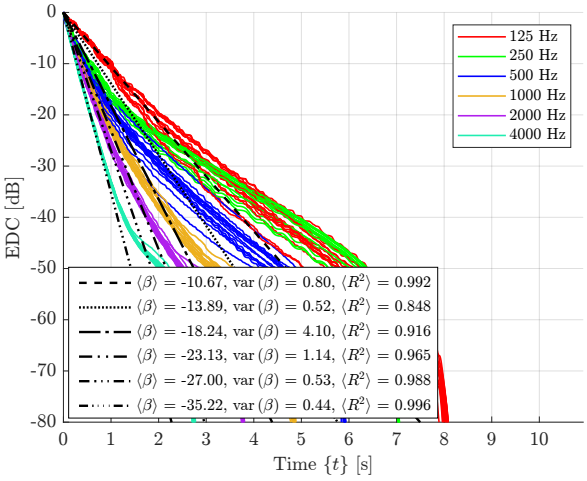

(e) Array #3, Source #1.

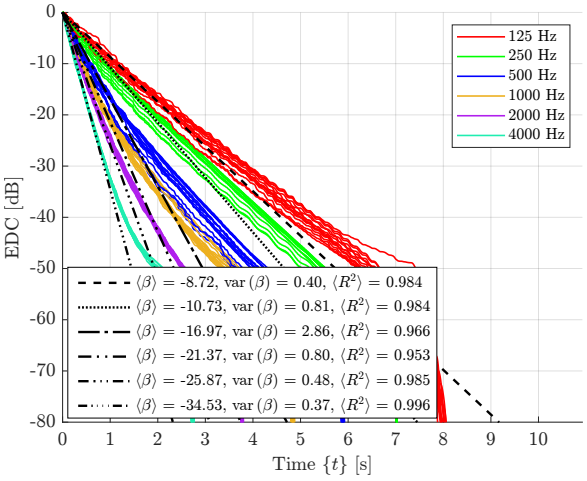

(f) Array #3, Source #2.

Source: own authorship (2024).

Figure 28 – EDCs for the three areas configuration.

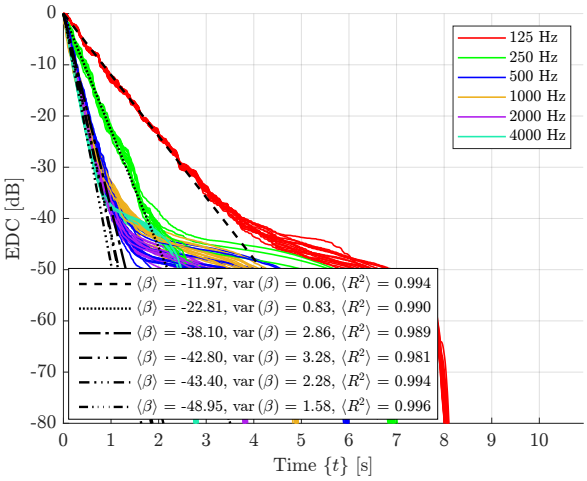

(a) Array #1, Source #1.

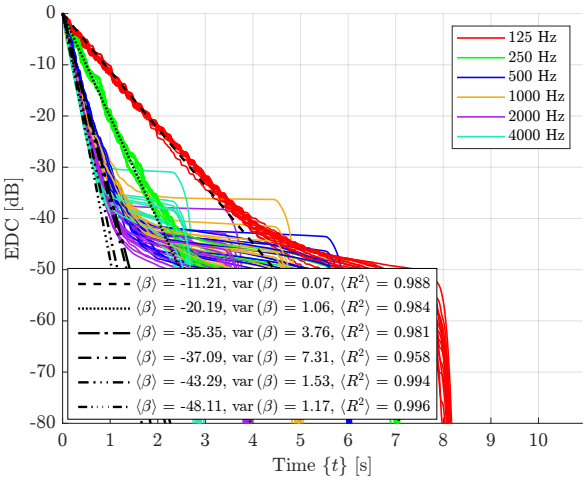

(b) Array #1, Source #2.

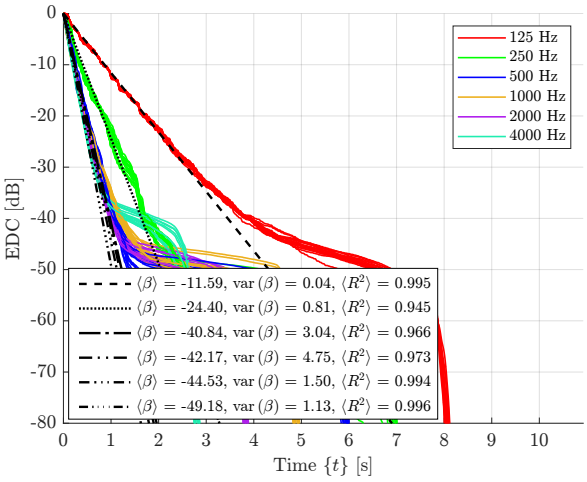

(c) Array #2, Source #1.

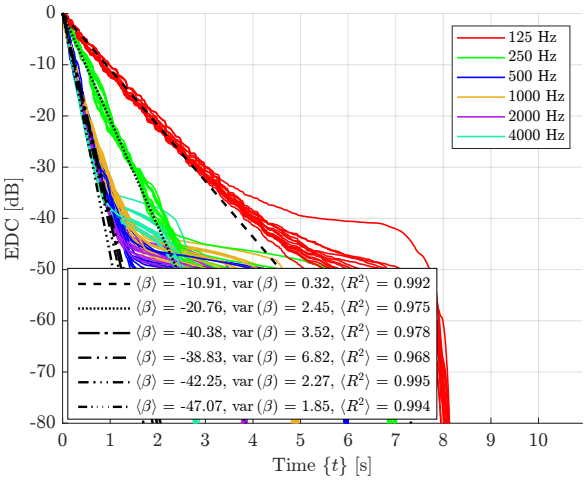

(d) Array #2, Source #2.

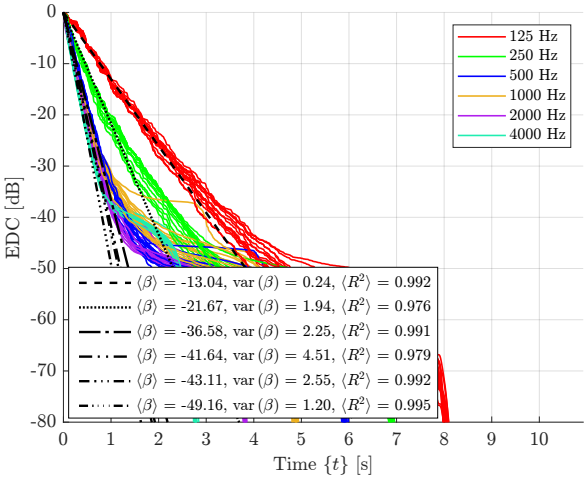

(e) Array #3, Source #1.

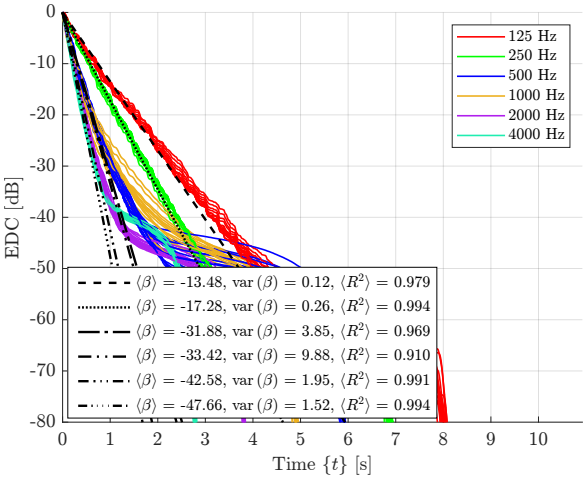

(f) Array #3, Source #2.

Source: own authorship (2024).

Figure 29 – EDCs for the five areas configuration.

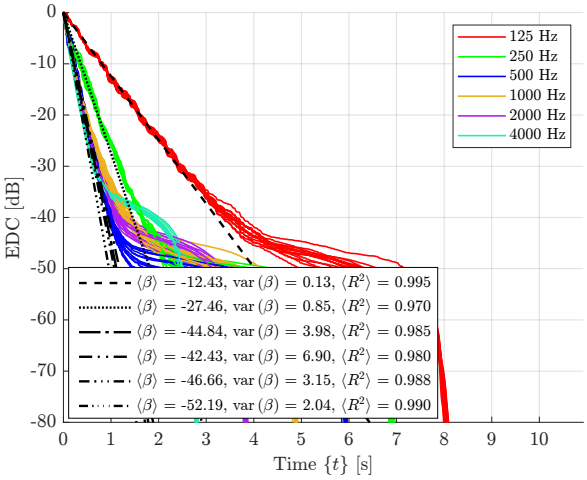

(a) Array #1, Source #1.

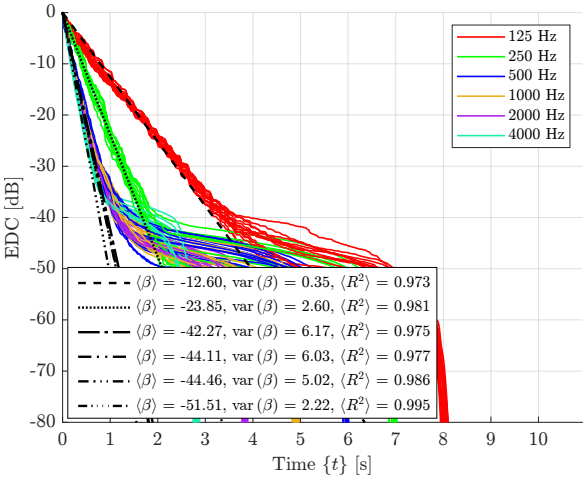

(b) Array #1, Source #2.

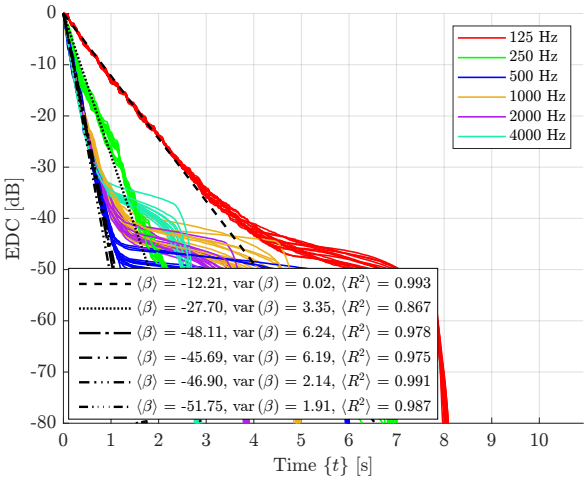

(c) Array #2, Source #1.

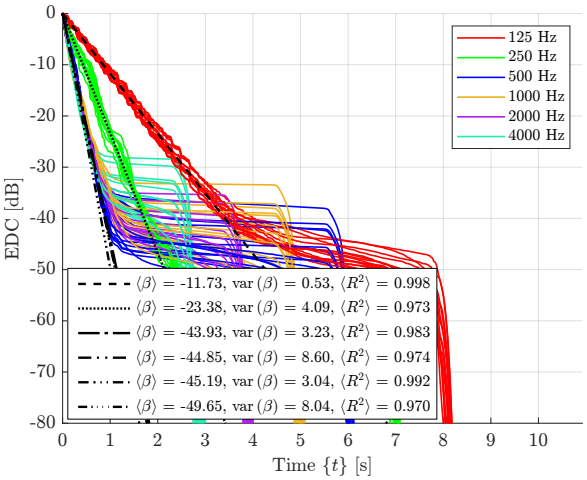

(d) Array #2, Source #2.

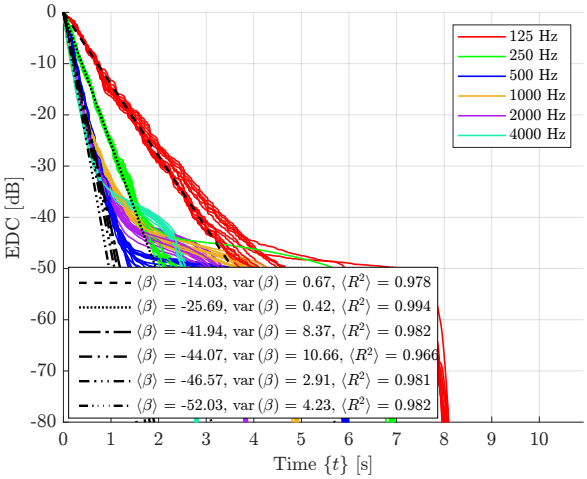

(e) Array #3, Source #1.

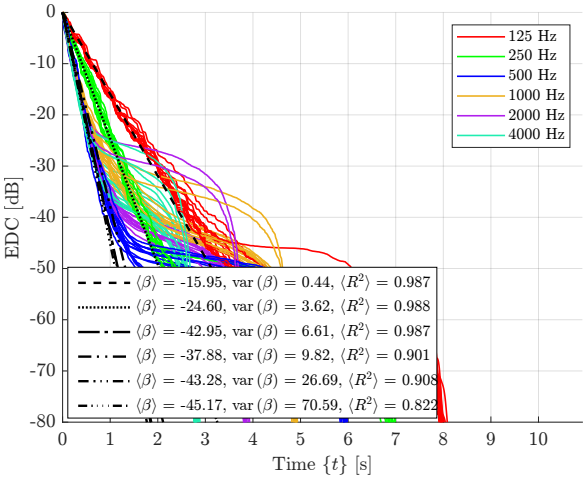

(f) Array #3, Source #2.

Source: own authorship (2024).

Figure 30 – Comparison between the decays for each absorption distribution at the position Array #1, Source #1.

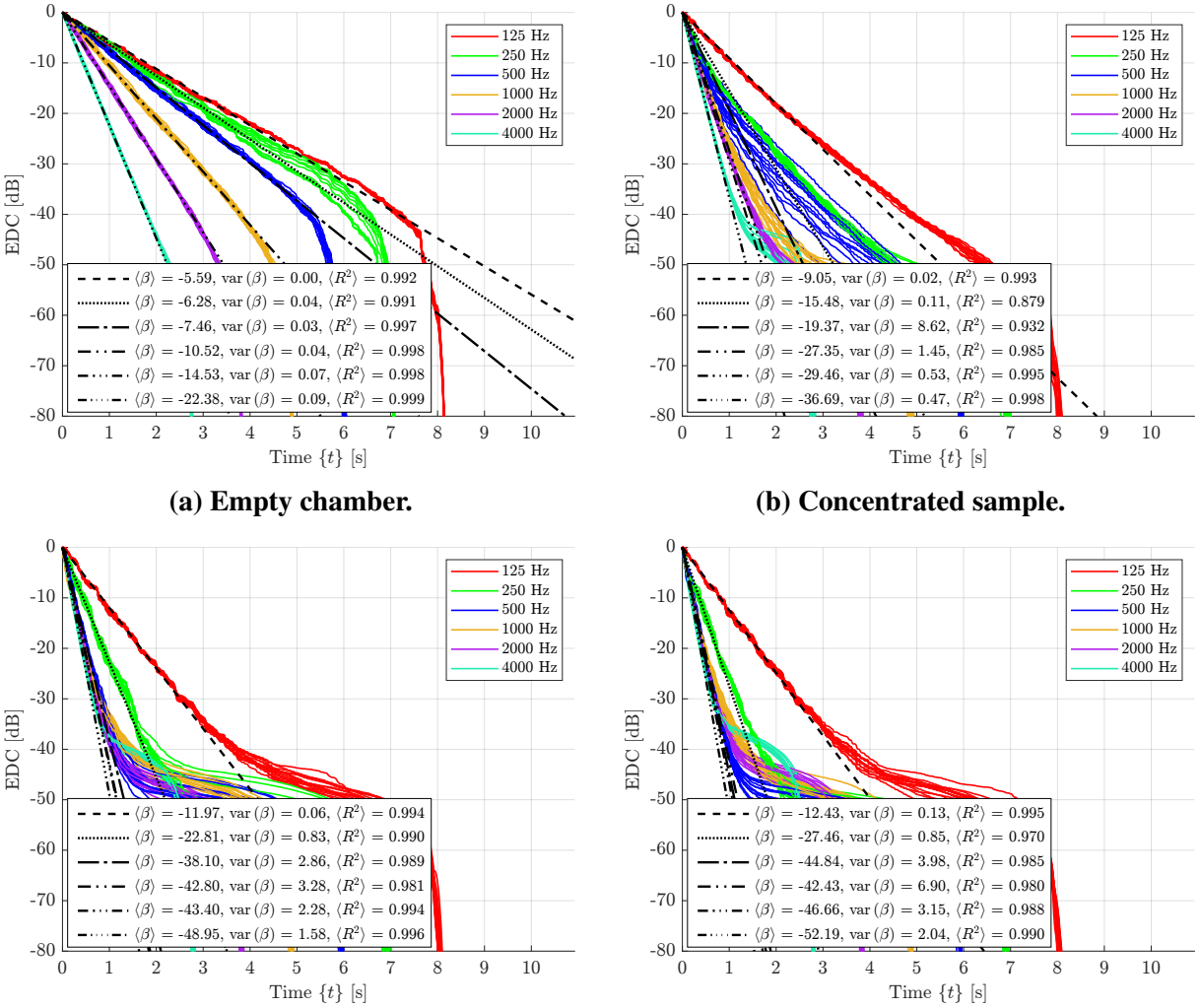

(a) Empty chamber. **(b) Concentrated sample.**

(c) Divided into three areas. **(d) Divided into five areas.**

Source: own authorship (2024).

Distributing the absorption in more than one direction makes the energy decay more uniform in space. Moreover, the decay gets more uniform and close to an exponential for the higher frequencies. This lines up with what is proposed by Randall and Ward (1960) and summarised by Everest (2001). Analysing from what is proposed by Balint *et al.* (2022), the changes in the energy decay functions, in the cases with the presence of absorption, are an effect of the transformation of grazing directions (with relation to the absorber) into non-grazing directions, by placing part of the absorption in directions perpendicular to the direction of the concentrated absorption. This makes more reflections interact with an absorbing surface. It should be remarked that this uniformity in decay is only seen at the higher frequencies.

Evidently, these changes affect the absorption value measured by the Sabine formula, as lower decays imply faster reverberation times. Figure 31 displays the absorption per third-octave frequency band for each of the absorption distribution cases and for Miki's model. The

reverberation time adopted for this calculation was the T_{20}, and all were taken from point number 50 of the array.

Figure 31 – Diffuse-incidence absorption for each absorption case and for Miki's model. Blue: concentrated absorption. Pink: three areas. Purple: five areas. Grey: Miki's model.

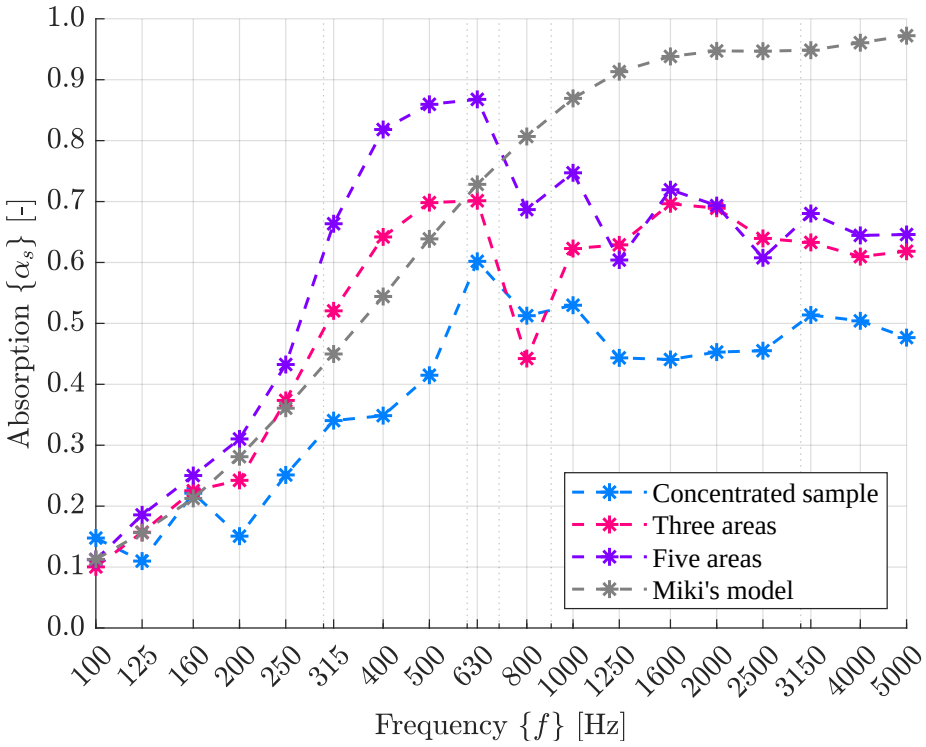

Source: own authorship (2024).

It is clear the influence of the distribution of the absorption in the absorption coefficient values. However, aside from some coherence at the lower frequencies, none of the cases measured at the reverberation chamber displays a matching behaviour to the reference absorption calculated from the flow resistivity of the sample, using Miki's model combined with the Paris' formula. This evidences that, although the absorption distribution affects the measured absorption, it does not necessarily mean that it is possible to correct the measurements only by distributing the absorption.

4.2.4 Isotropy Analysis

The isotropy can be calculated from the transfer function of the full impulse response or from the transfer functions of short time windows that sweep the impulse response in different instants (by means of the short-time Fourier Transform). The first presents a wavenumber spectrum that considers the whole history of the room excitation, which means that the wavenumber spectra contain information on the direct incidence, early reflections, and steady state of the sound field in the room. Consequently, the isotropy calculated from these can be interpreted as an "average" description of the temporal evolution of the sound field in the

measurement regions. The latter will present a time-dependent evolution of the spectra, which eventually leads to a time-dependent isotropy value. These parameters will be hereafter referred to as “full-response isotropy” and “time-dependent isotropy”, respectively.

4.2.4.1 Full-Response Isotropy

Figure 32 displays the full-response isotropy calculated using the 1-norm method for different excitation conditions (array and source combinations) in all absorption cases. Because of the odd result in Subsection 4.2.1 for the array #1 and source #2 in the empty chamber configuration, its results will be omitted.

Figure 32 – 1-norm full response isotropy for all absorption configurations.

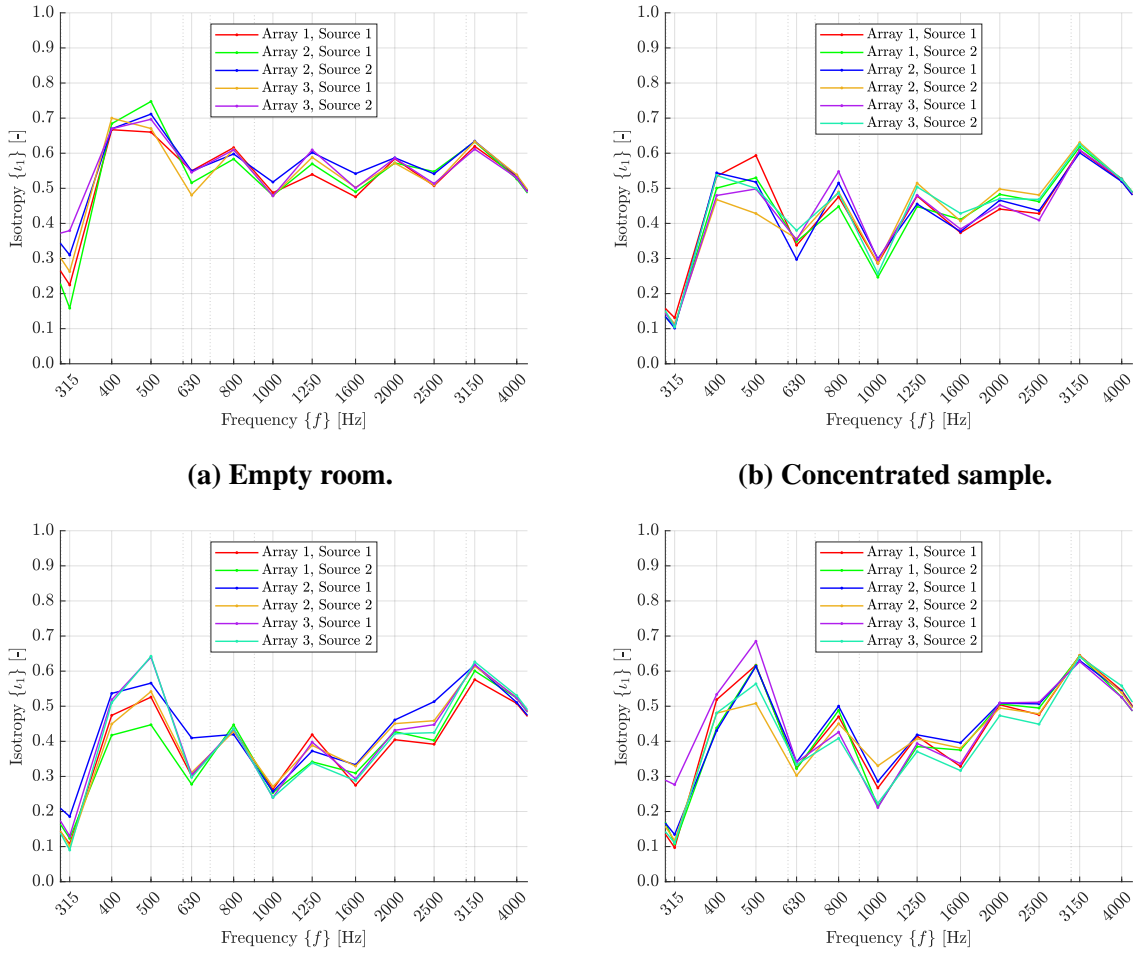

(a) Empty room.

(b) Concentrated sample.

(c) Three areas.

(d) Five areas.

Source: own authorship (2024).

Considering the maximum aperture of the array, the results from 315 Hz onward are trustworthy. It can be seen that, from 400 Hz onward, the variation in isotropy in relation to the excitation conditions is relatively small, and the largest variations happen at the transition from the 315 Hz band to the 400 Hz band. This can be related to the crossover frequency of the

room, estimated by Avelar *et al.* (2020). The highest isotropy values happen at the 400 Hz band and 500 Hz band, around 0.7. From 630 Hz onward, the isotropy varies between 0.48 and 0.63. These values are relatively far from 1, which is expected considering that the environment is a small rectangular chamber without diffusers.

Generally, the isotropy values between 315 Hz and 2500 Hz for the concentrated absorption case are smaller than for the empty room case, as expected. Moreover, it is noticeable that the variation of ι with the frequency is larger than for the empty room case. Comparing Figures 32b and 32c, it is noticeable that, from 500 Hz onward, although the average value of ι is seemingly the same, the variation from frequency to frequency is smaller. For frequencies smaller than 500 Hz, the variation appears to be at least as large. The isotropy values for the higher frequency bands (3150 Hz and 4000 Hz) are, at first sight, the same.

The isotropy values, although varying from case to case, display some coherence between the excitation conditions. This indicates that the isotropy of the sound field does not depend on the excitation conditions. The average isotropy for values of each absorption case are displayed in Figure 33. It is noticeable that the empty chamber case, even in the frequency with the lower isotropy value, presents larger values than the cases with absorption. However, no significant changes are seen between the cases of absorption and the expectation of the isotropy becoming larger following a more distributed absorption was not met, at least in the steady state sense.

Figure 33 – Average 1-norm full-response isotropy values from 315 Hz band to the 4000 Hz band.

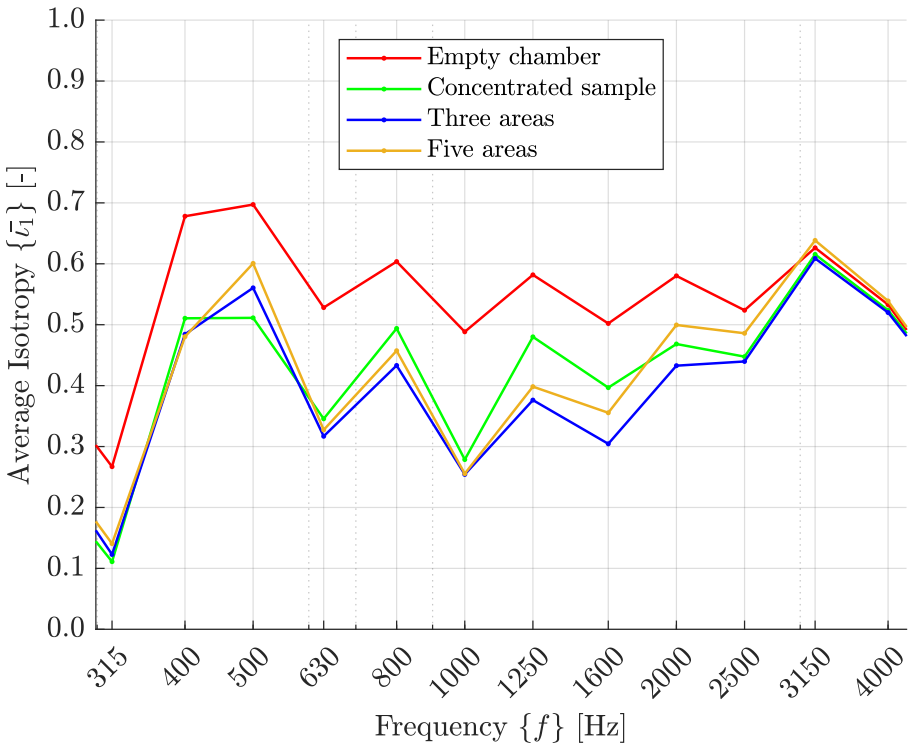

Source: own authorship (2024).

The 2-norm full-response isotropy for different excitation conditions (array and source combinations) in all absorption cases is displayed in Figure 34. All observations done for the 1-norm measurements are still valid for the 2-norm measurements. The most interesting remark that can be made for the 2-norm isotropy is that its values are consistently larger than for the 1-norm isotropy. This happens because the 2-norm is rotationally invariant, and the 1-norm is rotationally variant (TANAKA; OTANI, 2023). Naturally, when analysing Equation (42) and Equation (43), if the terms in the denominator of the 1-norm isotropy are overestimated, and the ones in the 2-norm technique are not, the value of the 2-norm will be larger than the 1-norm technique since the numerator of the ratio is the same for both formulas.

Figure 34 – 2-norm full response isotropy for all absorption configurations.

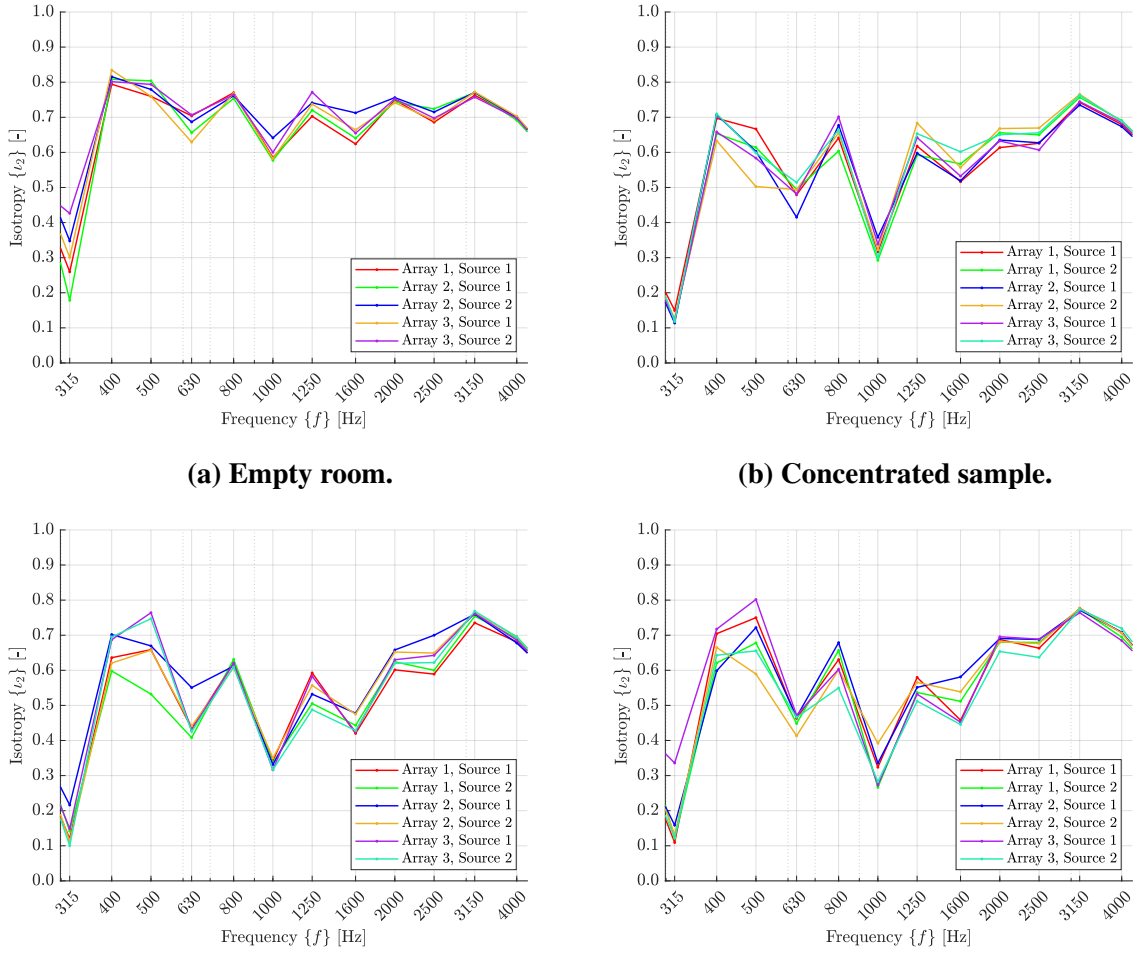

(a) Empty room. **(b) Concentrated sample.**

(c) Three areas. **(d) Five areas.**

Source: own authorship (2024).

Figure 35 shows the 2-norm average isotropy for all absorption cases.

The highest isotropy values happen at the 400 Hz band, around 0.8. From 630 Hz onward, the isotropy varies between 0.6 and 0.76. One thing that should be remarked is that although the 2-norm isotropy values are consistently larger than the 1-norm isotropy values, the

Figure 35 – Average 2-norm full-response isotropy values from 315 Hz band to the 4000 Hz band.

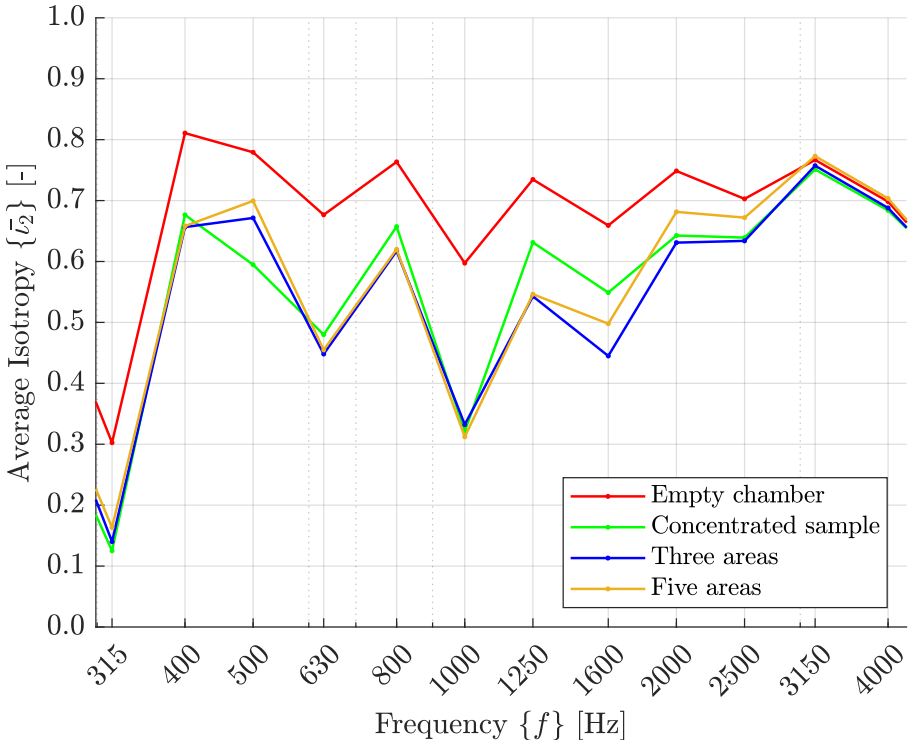

Source: own authorship (2024).

values do not rise in the same proportion. This is explained by the differences in the 1-norm and 2-norm evidenced in Chapter 2.

4.2.4.2 Time-Dependent Isotropy

The time-dependent isotropy was calculated from the impulse responses cut at 4 seconds and using the 1-norm method. This was done because the short-time windowing generates a large amount of data that takes a long time to be processed. Four seconds is enough to observe the isotropy during the first part of the decay and part of the steady state for the cases with distributed absorption. Also, because of the long processing time, only the array #1 source #1 position was analysed for all cases. The size of the time window was 0.17067, which corresponds to 2^{13} samples measured at a sampling frequency of 48000 Hz. The overlap between windows was set to 0, which amounted to 23 snippets of impulse responses. Each window has its Fourier transform calculated in the short-time Fourier transform, which then serves as inputs to the plane decomposition process, as each window will lead to a singular regularisation and, consequently, an angular spectrum. Figure 36 displays the time-dependent isotropy for the absorption cases at 500 Hz, calculated from the third-octave averaged angular spectrum (Figure 36a) and from the octave averaged angular spectrum (Figure 36b). The time-dependent isotropy averaged in third-octave bands displayed in Figure 36a have erratic behaviour, and it is hard to define a tendency of the evolution of absorption in time and its

relations. This also happens at other frequency bands. For the isotropy calculated from the octave band, the apparent behaviour is that, for the cases with absorption, the isotropy goes down during the first part of the decay and then rises back, oscillating around a constant level. In contrast, the isotropy is constant in time in the empty chamber case. However, this behaviour is not typical to all frequency bands, and it is difficult to identify a pattern.

Figure 36 – Time-dependent isotropy for all absorption cases at 500 Hz.

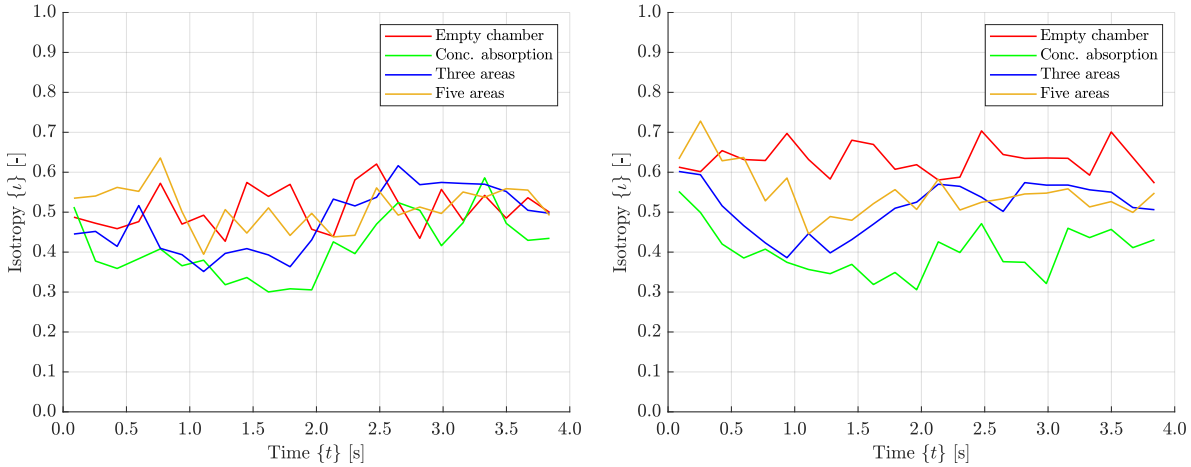

(a) For the third-octave band angular spectra. **(b) For the octave band angular spectra.**

Source: own authorship (2024).

4.2.5 Considerations

The objectives of this experiment were to compare decay characteristics and the sound field isotropy for different absorption configurations and excitation conditions (defined by the various combinations of source and array positions) and, in parallel, to verify characteristics relating to the sound field reconstruction process and numerical aspects of the plane-wave decomposition process.

It was observed that the reconstruction for positions inside the volume defined to generate the input points was consistently more accurate than for positions outside the generating volume. This tendency is still verified even in outlier cases, which might be related to the regularisation parameter selection or hardware connection problems during measurements. Moreover, the quality of the reconstruction, apart from the outliers, displays the same behaviour for all excitation conditions.

The numerical aspects of the plane-wave decomposition operator — the matrix $\mathbf{H}$ — were analysed using the Gram matrix, from which the coherence of the operator and its condition number can be evaluated. The analysis showed that the random array presents better numerical characteristics than other array formats, such as spherical and planar arrays because there is less redundant information input in the problem. This, by itself, does not guarantee

that the solution to the inverse problem accurately represents the physical characteristics of the sound field, as the choice of regularisation parameters and operational and environmental conditions also factor in estimating the angular spectrum.

The energy decay analysis consisted of analysing the overall tendencies of the EDCs measured in all 210 positions for the different excitation conditions and absorption configurations. Aside from that, the average linear regression of each EDC was calculated for some interesting third-octave bands between -5 dB and the -25 dB — as in the T_{20} calculation, aiming to extract a decay coefficient for each curve. All the regressions presented good fits for this part of the curve. For the empty chamber, the variance in the decay coefficients is relatively small, and there seems to be independence of the measurement or excitation positions in the decay. Furthermore, the decays seem to be exponential when the chamber is empty. For the concentrated absorption case, the decay functions stop being exponential, and the variance of the estimated decay constants is larger than in the previous case. The decay constants also seem less independent of the measurement and source positions, although a well-defined relation can not be defined at this moment. When the absorber is divided into three areas, the decay coefficients for the higher frequencies align with each other, and the variance of the decay coefficients rises in comparison with the earlier cases indicating a larger variation. Furthermore, the decay constant values become larger in absolute terms, indicating a faster decay than for the earlier cases. The overall takeaway of this case is that due to this absorption positioning, the energy decay is becoming less uniform in space but more uniform in frequency. For the five areas division, the tendency is for the same changes observed for the three areas configuration to happen, with an even larger approximation of the decay coefficients for the higher frequencies and faster sound decays. In general, the effect of dividing the absorbing surface and positioning in other directions is explained by Balint *et al.* (2022), which attests that this transforms directions initially parallel to the absorber into directions that now have an absorbing surface, leading to more reflections interacting with the absorbers, which results in faster sound energy decays. This distribution of the absorption also makes the energy density in the room more uniform, which in turn results in decays that are more spatially uniform. However, this does not guarantee that a diffuse field exists in the enclosure, as is evidenced by the diffuseness indicator. Notwithstanding, the evaluation of the decay can be valuable, because even if it cannot guarantee that the sound field is diffuse, cases such as the three and five areas absorption can be evaluated using techniques such as the one proposed by Balint *et al.* (2022), which will reveal that the earlier decay might be indeed the one of a diffuse sound field — exponential, or linear in a logarithmic scale — but only in specific directions.

Concerning the full-response diffuseness indicator, there is almost no variation of the isotropy indicator relating to the excitation conditions in each absorption configuration, indicating that the isotropy does not depend directly on the excitation condition. As expected, the average isotropy for the empty chamber case is larger than the isotropy for the instances with absorption. However, no sensible changes in the isotropy for the cases with absorption

can be noticed. Another remark is the difference in the isotropy values when using the 1-norm and the 2-norm. The 2-norm isotropy values are consistently larger than the 1-norm isotropy due to the rotational invariance of the former. Because of that and considerations involving the order truncation in the spherical-harmonics decomposition, the 2-norm was considered more appropriate for the analysis.

The time-dependent isotropy analysis did not produce much information, as it was hard to identify any behaviour pattern. Moreover, while the octave averaged values for the time-dependent isotropy display a behaviour somewhat expected — higher isotropy in the empty chamber — this can be due to an excessive averaging of the wavenumber spectrum, which can lead to a forced smoothing of the average spectrum, promoting a higher isotropy value. In any case, it was not possible to identify a behaviour for the time-dependent isotropy consistent for the whole frequency range.

Looking at the absorption calculated from reverberation times extracted from one of the array positions, the general effect of the distribution is that the absorption values rise. However, all of the cases display different frequency behaviour than the model-based reference.

Further investigations relating to room diffuseness and decay characteristics are necessary. It is currently unclear, for instance, how the array's shape and distribution affect the calculations of the wavenumber spectra aside from the numerical aspect of the estimate. In this context, which also applies to Experiment #1 studied in Section 4.1, an array could have excellent numerical properties but present poor acoustical problems, leading to poor sound field representation. Although the operator can be numerically appropriate, the choice of regularisation parameter can help mitigate problems such as the excessive reconstruction errors in Section 4.2.3. Some types of regularisation parameters even allow for measurement and operator error estimates to be informed, which can provide angular spectra that are more accurate in representing the sound field and result in more accuracy in interpolation and extrapolation. Other future investigations involve the analysis of sound decay using the Bayesian estimation proposed by Balint *et al.* (2022), which can provide the actual decay constant values and reverberation times, potentially leading to more precise analyses.

5 CONCLUSION AND PERSPECTIVES

This work aimed to study experimental applications of the plane wave decomposition process and, in the case of the sound field diffuseness analysis, to connect the diffuseness measure with other sound field characteristics. Plane-wave decomposition involves solving an approximate three-dimensional inverse Fourier transform employing a regularisation to estimate its result from sampling the sound field at a particular frequency. The result of this calculation is the wavenumber — or angular — spectrum. The analysis was conducted by means of two experiments. In both experiments, characteristics of the sound field reconstruction using the wavenumber spectrum estimates were also evaluated.

The first experiment involved using a random sampling of the sound field near an absorbing surface to calculate the angular spectrum and then use it to estimate the absorption coefficient. Subsequently, this wavenumber spectrum is used to calculate the incidence-dependent sound absorption and the diffuse incidence sound absorption of the surface by means of the Paris formula. The estimation of the diffuse incidence absorption coefficient was deemed appropriate. Compared with Miki's model's values, the estimation through the angular spectrum appears to have a systematic error. Moreover, the reconstruction analysis revealed that, in general, a sampling composed of more positions produces reconstructions with smaller errors. Furthermore, this technique revealed itself to be appropriate to *in situ* conditions and not need very complex setups, as the robot can be exchanged for rigid arrays, and the sound source does not have strict requirements for its position.

The second experiment consisted of calculating the isotropy in several excitation conditions inside a reverberation chamber with changing absorption distributions around the room. From that, the isotropy values were compared to the characteristics of the sound energy decay in the room for different absorption configurations. The isotropy revealed that the diffuseness is higher for the empty chamber than for the cases with an absorber. However, the cases with absorption did not present significant differences in isotropy between themselves. This may be due to the room's characteristics, such as its dimensions, or that it was composed of, essentially, two smaller rooms coupled. The distribution of the absorption around the room had effects on the sound energy decay. With the absorber more distributed, the decays for higher frequencies started to become uniform, tending to the same decay constant value. The decays also become faster for all frequencies. Regarding the type of isotropy metric used, the 2-norm isotropy presents larger values. This is due to its characteristic of rotational invariance. Thus, it was deemed more correct than the 1-norm metric. Concerning the reconstruction, reconstructions to positions inside the same volume where the randomly generated array positions were created present fewer errors, on average, than reconstructions to positions outside the generation volume. Although it was impossible to observe any relevant diffuseness change with the absorption distribution, its changes and effects on the absorption calculation were

perceived. Moreover, the difference in diffuseness between the empty chamber and the cases with absorption was verified, which is a sign that the processing is overall correct.

More investigations can develop from this work. Shortcomings identified in both experiments, such as angular spectra that misrepresent the actual sound field or that present high reconstruction errors, can be mitigated by investigations of factors such as better array shape and control of the distances between microphone positions, more appropriate experimental setups, with better array and source positioning, and the utilisation of other types of regularisation parameters when estimating the wavenumber spectrum. This last topic is especially interesting since there is evidence that different methods for finding the regularisation parameters can lead to more accurate reconstructions, specifically in non-reverberating environments (de Carvalho *et al.*, 2022).

REFERENCES

BRANDÃO, E. **Acústica de Salas**: projeto e modelagem. São Paulo, São Paulo: Blucher, 2016. ISBN 978-85-212-1006-1.

JACOBSEN, F.; JUHL, P. M. **Fundamentals of General Linear Acoustics**. Chichester, United Kingdom: John Wiley & Sons, 2013.

KUTTRUFF, H. **Room Acoustics**. 5. ed. 2 Park Square, Minton Park, Abingdon, Oxon OX14 4RN: Spon Press, 2009.

VORLÄNDER, M. **Auralization**: fundamentals of acoustics, modelling, simulation, algorithms and acoustic virtual reality. 1. ed. [S.l.]: Springer, 2008. ISBN 978-3-540-48829-3.

ISO. **ISO 354**: Acoustics – measurement of sound absorption in a reverberation room. Geneva, Switzerland, 2003.

ISO. **ISO 3382**: Acoustics - Measurement of the reverberation time of rooms with reference to other acoustical parameters. Geneva, Switzerland, 2010.

de Carvalho, A. C. F.; GOMES, M. H. de A.; SANT'ANA, L. H. The diffuse sound field according to literature: similarities and differences. In: **XII Iberoamerican Congress of Acoustics**. Florianópolis, Brazil: [s.n.], 2022.

JEONG, C.-H. Diffuse sound field: challenges and misconceptions. In: **45 Inter-Noise**. Hamburg, Germany: [s.n.], 2016. p. 1015–1021. Available from Internet: https://pdfs.semanticscholar.org/7389/.

VERCAMMEN, M. L. S. Improving the accuracy of sound absorption measurement according to iso 354. In: **International Symposium on Room Acoustics 2010**. Melbourne, Australia: [s.n.], 2010.

JEONG, C.-H.; NOLAN, M.; BALINT, J. Difficulties in comparing diffuse sound field measures and data/code sharing for future collaboration. In: **Euronoise 2018**. Crete, Greece: [s.n.], 2018.

NOLAN, M. **Experimental characterization of the sound field in a reverberation room**. 2019. Thesis (PhD) — Technical University of Denmark, 2019. Available from Internet: https://orbit.dtu.dk/en/publications/experimental-characterization-of-the-sound-field-in-a-reverberati.

BERZBORN, M.; VORLÄNDER, M. Directional sound field decay analysis in performance spaces. **Building Acoustics**, v. 28, 2019. doi:10.1177/1351010X20984622.

VERCAMMEN, M. L. S. How to improve the accuracy of the absorption measurement in the reverberantion chamber? In: **NAG/DAGA**. Rotterdan: [s.n.], 2009. Available from Internet: https://www.researchgate.net/publication/228872645_How_to_improve_the_accuracy_of_the_absorption_measurement_in_the_reverberation_chamber.

de Carvalho, A. C. F. **Desenvolvimento de um Sistema Automatizado para Medições de Funções de Transferência entre Microfone e Fonte Sonora**. aug. 2021. 98 p. Bachelor's thesis — Universidade Tecnológica Federal do Paraná, Curitiba, aug. 2021.

JACOBSEN, F.; JUHL, P. M. **Fundamentals of General Linear Acoustics**. Chichester, United Kingdom: John Wiley & Sons, 2013. ISBN 978-1-118-34641-9.

CROCKER, M. J. **Handbook of Noise and Vibration Control**. 1. ed. Hoboken, United States of America: John Wiley & Sons, 2007. ISBN 978-0-471-39599-7.

SCHULTZ, T. J. Diffusion in reverberation rooms. **Journal of Sound and Vibration**, v. 16, p. 17–28, 1971. doi:10.1016/0022-460X(71)90392-0.

JACOBSEN, F. **The diffuse sound field**: Statistical considerations concerning the reverberant field in the steady state. 1979.

IEC. **IEC 61183**: Electroacoustics — Random-incidence and diffuse-field calibration of sound level meters. Geneva, Switzerland, 1994.

SCHROEDER, M. R. New method of measuring reverberation time. **Journal of the Acoustical Society of America**, v. 37, 1965. doi:10.1121/1.1909343.

RANDALL, K.; WARD, F. Diffusion of sound in small rooms. **Proceedings of the IEE - Part B: Electronic and Communication Engineering**, v. 107, 1960. doi:10.1049/pi-b-2.1960.0147.

BALINT, J. *et al.* Bayesian decay time estimation in a reverberation chamber for absorption measurements. **Journal of the Acoustical Society of America**, v. 146, 2022. doi:10.1121/1.5125132.

NOLAN, M. Estimation of angle-dependent absorption coefficients from spatially distributed in situ measurements. **The Journal of the Acoustical Society of America**, v. 147, p. 119–124, 2020. doi:10.1121/10.0000716.

SOUZA, G. A. **Desenvolvimento de um escâner automatizado para medição sequencial e caracterização espaço-temporal de materiais acústicos**. 2022. Dissertation (Master) — Universidade Federal de Santa Maria, 2022.

de Carvalho, A. C. F. *et al.* Application of wave-number approach for room behaviour analysis and absorption coefficient measurement. In: **XII Iberoamerican Congress of Acoustics**. Florianópolis, Brazil: [s.n.], 2022.

SABINE, W. C. **Collected Papers on Acoustics**. Cambridge, USA: Harvard University Press, 1922.

KUTTRUFF, H. **Acoustics**: An introduction. 1. ed. [S.l.]: Taylor & Francis, 2007. ISBN 0-203-97089-6.

PRAWDA, K.; SCHLECHT, S. J.; VÄLIMÄKI, V. Calibrating the sabine and eyring formulas. **Journal of the Acoustical Society of America**, v. 152, 2022. doi:10.1121/10.0013575.

NOLAN, M.; FERNANDEZ-GRANDE, E.; JEONG, C.-H. Characterization of diffusivity based on spherical array processing. In: **Internoise 2015**. San Francisco, United States of America: [s.n.], 2015.

NOLAN, M. *et al.* A wavenumber approach to characterizing the diffuse field conditions in reverberation rooms. In: **22nd International Congress on Acoustics**. Buenos Aires, Argentina: [s.n.], 2016.

BRANDÃO, E.; FERNANDEZ-GRANDE, E. Analysis of the sound field above finite absorbers in the wave-number domain. **The Journal of the Acoustical Society of America**, v. 151, p. 3019–3030, 2022. doi:10.1121/10.0010355.

FERNANDEZ-GRANDE, E. Sound field reconstruction using a spherical microphone array. **Journal of the Acoustical Society of America**, v. 139, 2016. Available from Internet: doi.org/10.1121/1.4943545.

BERZBORN, M. *et al.* On the directional properties of energy decay curves. In: **23rd International Congress on Acoustics**. Aachen, Germany: [s.n.], 2019. p. 4043–4050. Available from Internet: http://pub.dega-akustik.de/ICA2019/data/articles/001139.pdf.

SOUZA, G. A.; FONSECA, W. D.; BRANDÃO, E. Desenvolvimento de um escâner automatizado para medição sequencial de respostas ao impulso. In: **XII Iberoamerican Congress of Acoustics**. Florianópolis, Brazil: [s.n.], 2022.

de Carvalho, A. C. F. *et al.* Solution of ill-posed problem in plane wave decomposition for sound field reconstruction. In: **XLIII Ibero-Latin American Congress on Computational Methods in Engineering**. Foz do Iguaçu, Brazil: [s.n.], 2022.

HANSEN, P. C. **Discrete Inverse Problems**: Insight and algorithms. 1. ed. Philadelphia, United States of America: SIAM, 2010. ISBN 978-0-898716-96-2.

CESARO, A. de; LEITÃO, A. Problemas inversos: Uma introdução. In: **1st Colloquium of Mathematics of the South Region**. Santa Maria, Brazil: [s.n.], 2010.

NOLAN, M. *et al.* Experimental characterization of the sound field in a reverberation room. **The Journal of the Acoustical Society of America**, v. 145, p. 2237–2246, 2019. doi:10.1121/1.5096847.

FAHIM, A. **Spatial dissection of a soundfield using spherical harmonic decomposition**. oct. 2019. 223 p. Thesis (PhD) — Australian National University, Canberra, oct. 2019.

TANAKA, T.; OTANI, M. An isotropic sound field model composed of a finite number of plane waves. **Acoustical Science and Technology**, v. 44, n. 4, p. 317–327, 2023. doi:10.1250/ast.44.317.

Mitsubishi Electric Corporation. **Industrial micro-robot system model RV-M1 technical manual**. Nagoya, Japan, 1989.

BERZBORN, M. *et al.* The ITA-Toolbox: An Open Source MATLAB Toolbox for Acoustic Measurements and Signal Processing. In: **43rd Annual German Congress on Acoustics**. Kiel, Germany: [s.n.], 2017. Available from Internet: http://publications.rwth-aachen.de/record/687308.

MÜLLER, S.; MASSARANI, P. Transfer-function measurement with sweeps: Director's cut including previously unreleased material. **Journal of the Audio Engineering Society**, v. 49, 2001. Available from Internet: https://www.researchgate.net/publication/258210091_Transfer-function_measurements_with_sweeps-Director\%27s_cut_including_previously_unreleased_material_and_some_corrections.

Steinberg Media Technologies GmbH. **ASIO4ALL v2**. 2023. Available from Internet: https://asio4all.org/.

CROCKER, M. J. **Introduction to Robotics**: Mechanics and control. 3. ed. New Jersey, United States of America: Pearson Education, 2005. ISBN 0-13-123629-6.

SEMECHKO, A. **Suite of functions to perform uniform sampling of a sphere v1.6.0.1**. 2021. GitHub. Available from Internet: https://github.com/AntonSemechko/S2-Sampling-Toolbox.

NOLAN, M.; XIANG, N. Bayesian selection of plane wave decomposition models. **JASA Express Letters**, v. 3, n. 3, p. 1–7, 2023. doi:10.1121/10.0017440.

HANSEN, P. C. **Regularization Tools Version 4.0 for Matlab 7.3**. 2007. MathWorks. Available from Internet: http://www2.compute.dtu.dk/~pcha/Regutools/.

RICHARD, A.; FERNANDEZ-GRANDE, E. Comparison of two microphone array geometries for surface impedance estimation. **Journal of the Acoustical Society of America**, v. 146, n. 1, p. 501–504, 2019. doi:10.1121/1.5116705.

KUTTRUFF, H. **Room Acoustics**. 5. ed. 2 Park Square, Minton Park, Abingdon, Oxon OX14 4RN: Spon Press, 2009. ISBN 978-1-4822-6043-4.

Saint-Gobain Vidros S.A. Divisão Isover. **Isosound - Painéis Acústicos Revestidos**. São Paulo, São Paulo, Brazil, 2009.

MIKI, Y. Acoustical properties of porous absorbers – Modifications of Delany-Bazley models. **Journal of the Acoustical Society of Japan (E)**, v. 11, n. 1, p. 19–24, 1990. doi:10.1250/ast.11.19.

SPROROWSKI, A. I.; ALBERTS, M. **Avaliação da Qualidade do Campo Acústico de uma Câmara Reverberante**. jun. 2018. 41 p. Bachelor's thesis — Universidade Tecnológica Federal do Paraná, Curitiba, jun. 2018.

FERNANDEZ-GRANDE, E.; XENAKI, A.; GERSTOFT, P. A sparse equivalent source method for near-field acoustic holography. **Journal of the Acoustical Society of America**, v. 141, n. 1, p. 532–542, 2017. doi:10.1121/1.4974047.

EVEREST, F. A. **The Master Handbook of Acoustics**. 4. ed. United States of America: McGraw-Hill, 2001. doi:10.1036/0071399747. ISBN 0-07-139974-7.

AVELAR, M. *et al.* Evaluation of the crossover frequency based on the analysis of room transfer functions through statistical estimators. **Applied Acoustics**, v. 164, 2020. doi:10.1016/j.apacoust.2020.107247.

GRAS Sound & Vibration. **GRAS 46AQ**. Denmark, 2021.

APPENDIX

APPENDIX A – INTRODUÇÃO (TRANSLATED TO PORTUGUESE)

De acordo com Brandão(BRANDÃO, 2016), a acústica de salas é uma área do estudo generalizado do som que envolve a interação do som dentro de ambientes fechados. O comportamento do som dentro deste ambiente está relacionado com as interações entre o som e as superfícies dos objetos e os limites da sala. Nesse contexto, muitos ambientes em condições reais, como salas de gravação, auditórios, salas de aula, salas de videoconferência, salas de concerto, e até mesmo cabines de audiometria, devem ser projetados, simulados e construídos utilizando técnicas provenientes da acústica de salas.

Determinar as características acústicas dos materiais é relevante ao projetar, simular, ou especificar materiais de construção. Com respeito a reflexão do som incidindo em uma superfície, Brandão (BRANDÃO, 2016) define três tipos de fenômeno: absorção, reflexão especular, e reflexão difusa. A parte dessas, há outros efeitos e características relacionadas como perda por transmissão (JACOBSEN; JUHL, 2013), efeito de difração de borda (KUTTRUFF, 2009),e a impedância de superfície (VORLÄNDER, 2008).

A partir dessas características, um engenheiro pode prever ou simular como o som se comporta nesse recinto e tomar decisões que afetarão requisitos de projeto como isolamento, coloração, tempo de reverberação, e nível de ruído de fundo, dentre outros.

Portanto, a existência de processos bem definidos de medição de parâmetros de materiais que afetam requisitos de construção é essencial. Normalmente, as medições são embasadas em padrões aprovados pela Organização Internacional de Normalização (em inglês: *International Organization for Standardization*, ISO). Até mesmo a nível local, orgãos de padronização como a Associação Brasileira de Normas Técnicas (ABNT), o Instituto Alemão para Normalização (em alemão: *Deutsches Institut für Normung*, DIN), a Instituição Britânica de Normas (em inglês: *British Standards Institution*, BSI), a Sociedade Americana para Testes e Materiais (em inglês: *American Society for Testing and Materials*, ASTM), e o Instituto Nacional Americano de Normas (em inglês: *American National Standards Institute*, ANSI) se baseiam em normas ISO quando definem seus procedimentos e requisitos. Às vezes, uma norma ISO pode ser inclusive aceita como uma norma local.

As normas ISO, em especial a ISO 354 (ISO, 2003), e a ISO 3382 (ISO, 2010), eventualmente aplicam resultados clássicos e técnicas de acústica de salas como a equação de Sabine para o cálculo da absorção em incidência aleatória (KUTTRUFF, 2009) e a integral cumulativa no sentido inverso de Schroeder para medir tempo de reverberação (BRANDÃO, 2016). No caso da equação de Sabine, uma das hipóteses que embasam sua derivação é o pressuposto de que o campo sonoro na sala é difuso. Vale ressaltar que a equação de Sabine foi inicialmente desenvolvida empiricamente e posteriomente demonstrada sob a hipótese mencionada.

Um campo acústico difuso pode ser definido de diversas maneiras e possui muitas propriedades interessantes (de Carvalho; GOMES; SANT'ANA, 2022). De acordo com Jeong (JEONG, 2016), um campo sonoro difuso é um campo sonoro no qual a pressão sonora é uniforme em todos os pontos da sala (homogêneo), e a probabilidade de fluxo de energia é

a mesma em todas as direções (isotrópico). Dito isso, em câmaras reverberantes, durante a medição de absorção sonora, devido à concentração de absorção em uma superfície, é evidente que existirá uma diferença em fluxo de energia na direção da absorção. Logo, o campo sonoro não será difuso. Muitos pesquisadores apontaram esta inconsistência e despenderam esforços para investigar temas como a variação excessiva dos valores do coeficiente de absorção e da isotropia em câmaras reverberantes de laboratório em laboratório (VERCAMMEN, 2010; JEONG; NOLAN; BALINT, 2018), a abordagem da isotropia em câmaras de reverberação (NOLAN, 2019), o comportamento da isotropia durante o decaimento sonoro (BERZBORN; VORLÄNDER, 2019), entre outras pesquisas.

No contexto do estudo de um campo sonoro em termos materiais, Kuttruff (KUTTRUFF, 2009) afirma que uma distribuição não uniforme da absorção dentro da câmara reverberante fatalmente produz um campo acústico que não é difuso. Essa é a condição esperada no procedimento proposto na norma ISO 354 (ISO, 2003), que tenta contorná-la adicionando elementos difusores nos limites do recinto. Isto implica em uma séria de problemas porque não somente é difícil quantificar o efeito destes difusores sobre o campo sonoro, mas a adição destes aparatos difusores também pode levar a adição de mais absorção ao sistema, o que pode causar resultados contaminados ou enviesados, normalmente apresentando valores de absorção mais altos que a realidade. Ademais, o valor da absorção também pode ser superestimado a valores acima de um devido ao efeito de difração de borda.

Todas essas incertezas e superestimações, efeitos de escolhas feitas na produção de normas eventualmente leva companhias a selecionar laboratórios ou projetos de câmaras reverberantes que favoreçam valores de absorção mais altos. Vercammen (VERCAMMEN, 2010; VERCAMMEN, 2009) se refere a isso como um processo de “compras”. Além disso, a incoerência entre valores medidos as características verdadeiras de material podem levar a más decisões de projeto feitas por arquitetos, engenheiros, e projetistas, influenciadas por fatores ocultos que não podem controlar nem corrigir de forma prática. Inclusive, podem haver diferenças entre as condições laboratoriais nas quais as medições são realizadas e as condições reais de aplicação. Neste caso, técnicas de medição *in situ* para medir a absorção sonora podem ser uma maneira interessante de contornar os requisitos de campo difuso.

A.1 Objetivos

Dentro do contexto apresentado, esta dissertação visa estudar aplicações da técnica da decomposição em ondas planas para medir a absorção sonora de uma superfície e quantificar a isotropia do campo acústico.

A.1.1 Objetivos Específicos

Alguns objetivos específicos podem ser derivados do objetivo geral deste trabalho, sem ordem específica:

- Implementar o processamento da decomposição em ondas planas utilizando técnicas de solução de problemas inversos;
- Implementar o cálculo da absorção e a fórmula de Paris;
- Implementar a medida de isotropia empregando decomposição em harmônicos esféricos;
- Validar os cálculos implementados usando simulação; e
- Realizar testes e experimentos.

Devido às diversas aplicações da decomposição em ondas planas, o aspecto experimental desta epsquisa foi dividido em dois, uma parte focando nas medições de absorção e outra focando nas medições de isotropia. Isto também permitiu que o autor utilizasse conjuntosde dados medidos previamente pelo próprio autor em trabalhos prévios (de Carvalho, 2021), cujo tema foi a utilização de um robô como um array para realizar medições de campo sonoro para os fins explorados neste trabalho.

A.2 Abordagem Metodológica

O campo sonoro dentro de um ambiente pode ser abordado de diversas maneiras. Nesta pesquisa, optou-se por seguir as técnicas propostas por Nolan (NOLAN, 2019) para calcular a decomposição em ondas planas do campo sonoro em uma região em particular dentro de um recinto.

Para a medição da absorção *in situ*, os dados medidos pelo próprio autor em outro trabalho (de Carvalho, 2021) foram utilizados. O experimento consistiu de uma superfície absorvente montada em uma das paredes de uma laboratório com mobília e equipamentos. A sala foi excitada com uma fonte omnidirecional, e um robô foi utilizado como um arranjo seuqneciado de microfones com posições aleatórias para medir o campo sonoro próximo do absorvedor. Das medições do array, os espectros angulares para uma faixa de frequência foram calculados utilizando a decomposição em ondas planas, e cada um deles pode ser utilizado para calcular a absorção sonora direcional da superfície. A fórmula de Paris (BRANDÃO, 2016) pode estimar a absorção em incidência difusa a partir de valores dependentes da direção de incidência.

Para os experimentos relacionados às condições de campo difuso, múltiplas baterias de medições com arranjo sequencial com diferentes pares de posições de arranjo e de fonte

para diferentes configurações de absorção foram realizadas dentro da câmara reveberante. A decomposição em ondas planas é calculada destes conjuntos de dados e, subsequentemente, a isotropia do campo sonoro. Também é possível extrair as curvas de decaimento de energia em cada posição de microfone das medições com arranjo. A intenção é identificar e correlacionar a isotropia do campo sonoro e as curvas de decaimento de energia para as diferentes configurações de absorção.

A.3 Estrutura do Documento

Capítulo 1 apresentou uma introdução ao tema desta dissertação e os principais objetivos desta pesquisa.

Capítulo 2 mostra o embasamento teórico e uma revisão bibliográfica de conceitos e técnicas vitais para a compreensão deste trabalho.

Capítulo 3 aborda a montagem experimental das medições com arranjo e justifica algumas das escolhas feitas durante a etapa exploratória da pesquisa.

Capítulo 4 é dividido em duas partes, cada qual relacionada a um dos experimentos conduzidos e suas respectivas análises e conclusões.

Capítulo 5 apresenta uma recapitulação geral do trabalho proposto, algumas descobertas e algumas perspectivas de potenciais desenvolvimentos futuros.

APPENDIX B – CONCLUSÃO E PERSPECTIVAS (TRANSLATED TO PORTUGUESE)

Este trabalho visou estudar aplicações experimentais do processo de decomposição em ondas planas e, no caso da análise da difusividade do campo sonoro, a relacionar a medida de difusividade com outras características do campo difuso. Decomposição em ondas planas envolve resolver uma transformada de Fourier inversa tridimensional utilizando uma regularização para estimar seu resultado a partir de medições do campo acústico em uma certa frequência. O resultado deste cálculo é o espectro do número de onda — ou espectro angular. A análise foi conduzida por meio de dois experimentos. Em ambos experimentos, características da reconstrução do campo sonoro utilizando as estimativas do espectro do número de onda também foram avaliadas.

O primeiro experimento envolveu a utilização de uma amostragem aleatória do campo acústico próximo de uma superfície absorvente para calcular o espectro angular e posteriormente utilizá-lo para estimar o coeficiente de absorção. Subsequentemente, este espectro do número de onda é utilizado para calcular a absorção sonora dependente da incidência e a absorção sonora em incidência difusa por meio da fórmula de Paris. A estimação do coeficiente de absorção sonora em incidência difusa foi considerada apropriada. Comparada com os valores obtidos por meio do modelo de Miki, a estimação por meio do espectro angular aparenta ter um erro sistemático. Além disso, a análise da reconstrução revelou que, em geral, um amostragem composta por mais posições produz reconstruções com erros menores. Ademais, esta técnica se revelou apropriada a condições *in situ* e não necessita de montagens muito complexas, visto que o robô pode ser substituído por arrays rígidos, e a fonte sonora não possui requisitos rigorosos com relação a sua posição.

O segundo experimento consistiu em calcular a isotropia em diversas condições de excitação dentro de uma câmara reveberante para várias distribuições de absorção ao redor da sala. Para isso, os valores de isotropia foram comparados com as características do decaimento de energia sonora na sala para diferentes configurações de absorção. A isotropia revelou que a difusividade é mais alta para a câmara vazia que para os casos com absorvedor. Contudo, os casos com absorção não apresentaram diferenças significativas na isotropia dentre eles. Isso poder ser devido às características da sala, como suas dimensões, ou pelo fato de que ela era composta por, essencialmente, duas salas menores acopladas. A distribuição de absorção ao redor da sala teve efeitos no decaimento energético do som. Com o absorvedor mais distribuído, os decaimentos para frequências mais altas começaram a ficar uniformes, tendendo ao mesmo valor de constante de decaimento. Os decays também ficam mais rápidos para todas as frequências. Com respeito ao tipo de métrica de isotropia utilizada, a isotropia de norma-2 apresenta valores mais altos. Isto se deve a sua característica de invariância rotacional. Portanto, ela foi considerada mais correta que a métrica de norma-1. Com relação à reconstrução, reconstruções em posições dentro do mesmo volume onde os valores aleatoriamente gerados do arranjo foram criados apresentam erros menores, em média, que reconstruções em posições fora do volume de geração. Embora tenha sido impossível observar qualquer mudanças relevantes na difusividade com a distribuição da absorção, suas mudanças e efeitos no cálculo da absorção

foram notados. Além disso, a diferença na difusividade entre a câmara vazia e os casos com absorção foi verificada, o que é um sinal de que o processamento está, no geral, correto.

Mais investigações podem ser desenvolvidas a partir deste trabalho. Insuficiências identificadas em ambos os experimentos, como espectros angulares que não representam corretamente o campo sonoro real ou que apresentam erros de reconstrução altos, podem ser mitigados por investigações de fatores como formatos melhores de array e controle das distâncias entre posições de microfone, montagens experimentais mais apropriadas, com posições melhores de arranjo e fonte, e a utilização de outros tipos de parâmetros de regularização na hora de estimar o espetro do número de onda. Este último tópico é especialmente interessante pois há evidências que métodos diferentes para definir o parâmetro de regularização podem levar a reconstruções mais precisas, especificamente em ambientes não reverberantes (de Carvalho *et al.*, 2022).

APPENDIX C – MATLAB FUNCTIONS AND SCRIPTS

The MATLAB functions and scripts utilised in this research are available at https://github.com/augustoc2112/PWD-and-Robot-Array, where they will be progressively published following the publication of this work.

ANNEX A – GRAS 46AQ SPECIFICATIONS

This annex is dedicated to displaying the frequency response (Figure 37) and the free-field corrections (Figure 38) of the GRAS 46AQ diffuse field microphone. According to the microphone datasheet, these plots were obtained from a 250 Hz excitation (GRAS Sound & Vibration, 2021).

Figure 37 – GRAS 46AQ frequency response.

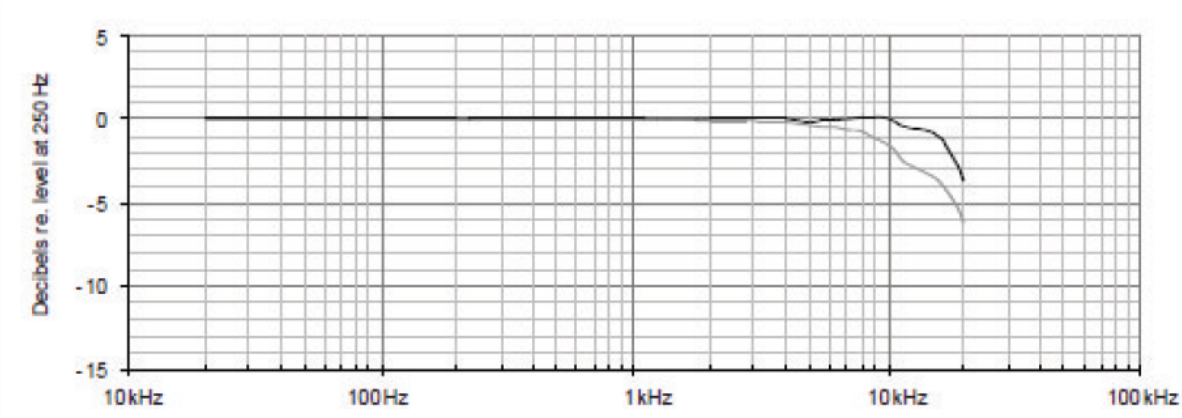

Source: GRAS Sound & Vibration (2021).

Figure 38 – GRAS 46AQ free-field corrections.

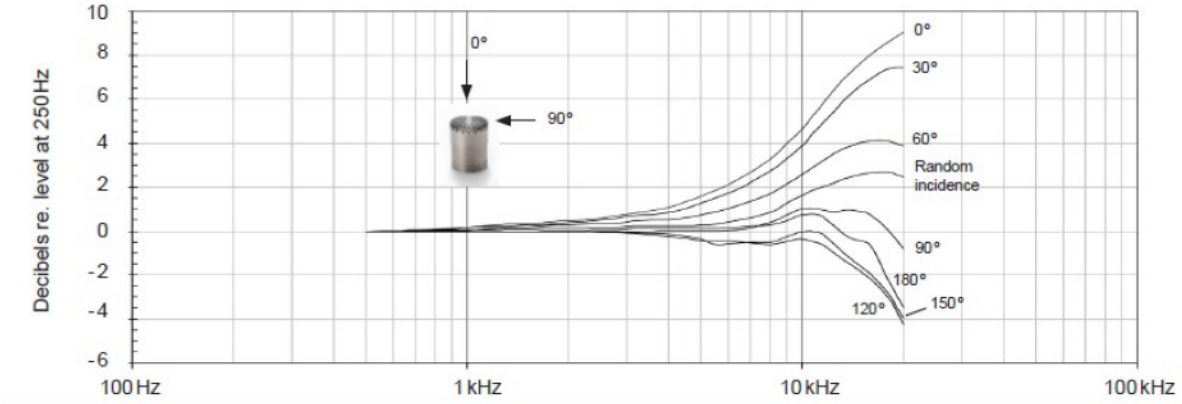

Source: GRAS Sound & Vibration (2021).